

Computational optical imaging based on helical point spread functions

Berlich, R.

DOI

[10.4233/uuid:9efdc813-e4a7-4a29-9023-1b95b498ca2a](https://doi.org/10.4233/uuid:9efdc813-e4a7-4a29-9023-1b95b498ca2a)

Publication date

2021

Document Version

Final published version

Citation (APA)

Berlich, R. (2021). *Computational optical imaging based on helical point spread functions*. [Dissertation (TU Delft), Delft University of Technology]. <https://doi.org/10.4233/uuid:9efdc813-e4a7-4a29-9023-1b95b498ca2a>

Important note

To cite this publication, please use the final published version (if applicable).
Please check the document version above.

Copyright

Other than for strictly personal use, it is not permitted to download, forward or distribute the text or part of it, without the consent of the author(s) and/or copyright holder(s), unless the work is under an open content license such as Creative Commons.

Takedown policy

Please contact us and provide details if you believe this document breaches copyrights.
We will remove access to the work immediately and investigate your claim.

COMPUTATIONAL OPTICAL IMAGING BASED ON HELICAL POINT SPREAD FUNCTIONS

COMPUTATIONAL OPTICAL IMAGING BASED ON HELICAL POINT SPREAD FUNCTIONS

Dissertation

for the purpose of obtaining the degree of doctor
at Delft University of Technology
by the authority of the Rector Magnificus prof. dr. ir. T.H.J.J. van der Hagen
chair of the Board for Doctorates
to be defended publicly on
Wednesday 3 February 2021 at 17.30 o'clock

by

René BERLICH

Master of Science in Photonics,
Friedrich-Schiller-Universität Jena, Germany
born in Gera, Germany

This dissertation has been approved by the promotor.

Composition of the doctoral committee:

Rector Magnificus, Prof. dr. S. Stallinga Dr. S.F. Pereira	chairperson Delft University of Technology, promoter Delft University of Technology, copromoter
--	---

Independent members:

Prof. dr. W.M.J.M. Coene	Delft University of Technology
Prof. dr. R. Piestun	University of Colorado, USA
Prof. dr. Y. Shechtman	Technion - Israel Institute of Technology, Israel
Dr. C.S. Smith	Delft University of Technology
Prof. dr. B. Rieger	Delft University of Technology, reserve member

Other members:

Dr. R. Brüning	Fraunhofer IOF, Germany
----------------	-------------------------



This work was carried out in collaboration between the Department of Imaging Physics at the faculty of Applied Sciences of Delft University of Technology and the Fraunhofer Institute for Applied Optics and Precision Engineering (IOF).

Keywords: Computational imaging, PSF engineering

Printed by: Ridderprint | www.ridderprint.nl

Front: Illustration of the propagation of an engineered, double-helix point spread function through the focus of an optical imaging system

Copyright © 2021 by R. Berlich

ISBN 978-94-6416-444-2

An electronic version of this dissertation is available at
<http://repository.tudelft.nl/>.

CONTENTS

Summary	vii
Samenvatting	ix
1 Introduction	1
1.1 Computational imaging	2
1.1.1 General concept	2
1.1.2 Point spread function engineering	5
1.1.3 Helical point spread functions	7
1.2 Motivation and outline	9
1.2.1 Depth retrieval for extended objects	9
1.2.2 Practical pupil phase implementation	11
1.2.3 Improved aberration robustness	11
1.2.4 Wavefront retrieval for extended objects	12
1.2.5 Outline of thesis	12
References	13
2 Single shot three-dimensional imaging	17
2.1 Introduction	18
2.2 System approach	19
2.2.1 Imaging setup	19
2.2.2 Image acquisition	20
2.2.3 Image processing	22
2.3 Proof-of-principle experiment	27
2.3.1 Setup implementation	27
2.3.2 Depth estimation	28
2.3.3 Image decoding	29
2.4 Conclusion	31
References	32
3 Fabrication of CGHs using FLDW	35
3.1 Introduction	36
3.2 Theoretical CGH modeling	36
3.3 CGH design and fabrication	38
3.4 Experimental performance validation	40
3.5 Conclusion	42
References	42

4	High-order-helix point spread functions	45
4.1	Introduction	46
4.2	Multi-order-helix designs	47
4.2.1	Design approach	47
4.2.2	Performance evaluation	50
4.3	Influence of aberrations on PSF rotation	52
4.3.1	Numerical investigation of PSF rotation	52
4.3.2	Theoretical rotation assessment	55
4.4	Experimental results	57
4.4.1	Optical setup	57
4.4.2	Demonstration of on-axis PSF rotation	58
4.4.3	PSF rotation across an extended field of view	60
4.5	Conclusion	63
4.6	Appendix: Evaluation of rotation measure M_n^m	63
	References	66
5	Image based aberration retrieval	69
5.1	Introduction	70
5.2	Pupil engineered phase diversity	71
5.3	Linear aberration retrieval model	74
5.4	Numerical performance assessment	78
5.4.1	Monte Carlo analysis	78
5.4.2	CRLB performance	79
5.4.3	Aberration retrieval performance	83
5.5	Experimental results	86
5.5.1	Point object approach verification	87
5.5.2	Extended scene	89
5.6	Conclusion	91
	References	92
6	Conclusion	97
6.1	Results	98
6.1.1	Passive, monocular 3D imaging acquisition	98
6.1.2	Image based wavefront measurement	100
6.2	Outlook	101
6.2.1	Machine vision cameras	101
6.2.2	Wavefront sensors	103
6.2.3	Further application scenarios	104
	References	104
	Acknowledgements	107
	Curriculum Vitæ	109
	List of Publications	111

SUMMARY

Helical point spread functions (PSFs) provide a powerful computational imaging tool for modern optical imaging and sensing applications. However, their utilization is, so far, limited to a single field of application, i.e. super-resolution microscopy, which is due to multiple shortcomings in their current system implementation.

A new computational imaging approach is developed in this thesis, which enables the utilization of helical PSFs and their unique advantages for applications in the area of machine vision. In particular, the approach can be used to acquire the three-dimensional distribution of a passively illuminated, extended scene in a single shot based on a compact, monocular camera setup. A novel image processing routine is established to overcome a major challenge of computational imaging using helical PSFs, i.e. the retrieval of the PSF rotation angle in the case of an extended object distribution.

The hardware implementation of computational imaging setups that rely on helical PSFs is based on a combination of a conventional optical element, such as a microscope objective or a camera lens, and an additional, dedicated pupil mask. This mask is commonly realized using either a spatial light modulator or a lithographic element that features a structured surface profile. Two new fabrication schemes with different advantages are explored in this thesis. The first scheme utilizes wafer-scale optical lithography in combination with UV-replication in order to fabricate highly cost efficient phase elements. The second method is based on femto-second laser direct writing. It enables the inscription of the phase element directly inside a transparent optical element using a single fabrication step. Therefore, it facilitates a flexible realization of highly integrated PSF engineered optical systems.

Current design concepts for pupil masks that generate helical PSFs only focus on double-helix distributions that feature two, laterally separated irradiance peaks. Furthermore, a diffraction limited performance of the computational imaging system is assumed. A new design method that enables the generation of multi-order-helix PSFs with an arbitrary number of rotating peaks is developed in this thesis. A study of the influence of first order aberrations on the rotation angle of multi-order-helix PSFs is performed in order to assess their effect on the accuracy limits with respect to three-dimensional imaging. In this context, the superior aberration robustness of high-order-helix PSFs featuring three or more rotating spots is demonstrated.

Whereas, on the one hand, the effect of aberrations on helical PSFs degrade the depth retrieval accuracy of three-dimensional imaging systems, their influence can be explored in order to obtain information on the system's wavefront aberrations on the other hand. To this end, the computational imaging approach developed for three-dimensional imaging is extended and combined with a conventional phase diversity method. The novel approach enables a numerically efficient estimation of general wavefront aberrations based on the acquisition of an extended, unknown object scene.

In summary, the research performed in this thesis provides the foundation to exploit the

unique advantages of computational imaging systems based on helical PSFs for applications in the area of three-dimensional imaging and wavefront sensing.

SAMENVATTING

Helical point spread functions (PSF's) bieden een krachtig rekenhulpmiddel voor beeldvorming voor moderne optische beeld- en sensortoepassingen. Het gebruik ervan is echter tot dusver beperkt tot een enkel toepassingsgebied, namelijk de superresolutie-microscopie, dankzij meerdere tekortkomingen in hun huidige systeemimplementatie. In dit proefschrift wordt een nieuwe benadering van computationele beeldvorming ontwikkeld, die het gebruik van spiraalvormige PSF's en hun unieke voordelen voor toepassingen op het gebied van de machine visie mogelijk maken. In het bijzonder kan deze benadering worden gebruikt om de drie-dimensionele verdeling van een passief belichte, uitgebreide scène in een enkele opname te verkrijgen op basis van een compact, monoculaire cameraopstelling. Een nieuwe beeldverwerkingsroutine is ontwikkeld om een belangrijke uitdaging van de computationele beeldvorming aan te pakken met behulp van spiraalvormige PSF's, d.w.z. het verkrijgen van de PSF-rotatiehoek in het geval van een uitgebreide objectdistributie.

De hardware-implementatie van computationele beeldvormingsopstellingen die gebaseerd zijn op spiraalvormige PSF's is gebaseerd op een combinatie van een conventioneel optisch element, zoals een microscoop-objectief of een cameralens, en een extra, toegewijd leerlingenmasker. Dit masker is meestal gerealiseerd met behulp van een ruimtelijke lichtmodulator of een lithografisch element dat beschikt over een gestructureerd oppervlakprofiel. Twee nieuwe fabricatieschema's met verschillende voordelen worden onderzocht in dit proefschrift. Het eerste schema maakt gebruik van waferschaal optische lithografie in combinatie met UV-replicatie om zeer kostenefficiënte fase-elementen te fabriceren. De tweede methode is gebaseerd op femto-seconde laser direct schrijven. Het maakt de inscriptie van het fase-element direct in een transparant optisch element mogelijk met behulp van een enkele fabricage-stap. Het vergemakkelijkt daarom een flexibele realisatie van sterk PSF geïntegreerde optische systemen.

De huidige ontwerpconcepten voor leerlingenmaskers die spiraalvormige PSF's genereren, richten zich alleen op dubbele-helix-verdelingen met twee, zijdelings gescheiden stralingspieken. Bovendien wordt uitgegaan van een diffractie beperkte prestatie van het computationele beeldvormingssysteem. In dit proefschrift wordt een nieuwe ontwerp-methode ontwikkeld die het genereren van multi-orde-helix PSF's met een willekeurig aantal roterende pieken mogelijk maakt. Er wordt een studie uitgevoerd naar de invloed van eerste-orde-afwijkingen op de rotatiehoek van multi-orde-helix PSF's om hun effect op de nauwkeurigheidsgrenzen met betrekking tot driedimensionale beeldvorming te beoordelen. In deze context wordt de superieure robuustheid van de aberratie van hoog-orde-helix-PSF's met drie of meer roterende vlekken aangetoond.

Terwijl enerzijds het effect van aberraties op spiraalvormige PSF's de nauwkeurigheid van diepterecuperatie van driedimensionale beeldvormingssystemen vermindert, kan hun invloed anderzijds worden onderzocht om informatie te verkrijgen over de golffrontafwijkingen van het systeem. Met het oog hierop is de computationele beeldvormings-

aanpak die is ontwikkeld voor driedimensionale beeldvorming uitgebreid en gecombineerd met een conventionele fase-diversiteitsmethode. De nieuwe benadering maakt een numeriek efficiënte schatting van algemene golf-frontafwijkingen mogelijk gebaseerd op de verwerving van een uitgebreide, onbekende objectscène.

Samengevat biedt het onderzoek in dit proefschrift de basis voor de exploitatie van de unieke voordelen van computationele beeldvormingssystemen op basis van spiraalvormige PSF's voor toepassingen op het gebied van driedimensionale beeldvorming en golf-front sensing.

1

INTRODUCTION

Autonomous driving, personalized and predictive medicine, computer vision and extended reality represent four of the seven biggest current technology trends according to *Forbes* [1]. Optical imaging represents a key enabling technology throughout all of these trends. It provides the data to safely navigate autonomous vehicles through traffic, to let robots seamlessly interact with humans and to embed virtual content into the physical world. State-of-the-art optical imaging systems require much more than simply capturing a picture of a scene of interest. Extracting information on an object or the light itself, in addition to providing a conventional two-dimensional image of the object scene, represents a major technological challenge. In particular, this may include the retrieval of information related to the object's three-dimensional shape as well as the wavefront, the polarization state and the spectrum of the reflected or the emitted light. Solving the challenge of retrieving this multi-dimensional data drives the developments of cutting-edge imaging concepts in modern application fields such as bio-medical imaging, machine-vision or remote sensing.

One particular concept to address this challenge is computational imaging, an imaging modality that merges the steps of optical image formation and computational image processing. It has become of major importance for a large range of applications, where these developments are made possible by the improvement of computer processing platforms, i.e. parallel computing using a cluster of processors, advances in signal processing algorithms, as well as the availability of modern sensing hardware.

1.1. COMPUTATIONAL IMAGING

1.1.1. GENERAL CONCEPT

Traditionally, optical imaging systems are designed and optimized for providing the best image quality. In order to define a suitable figure of merit that quantifies optical image quality, imaging systems are generally modeled based on the assumption that light that emanates from different parts of the object distribution is incoherent. In this case, the image formation can be described using a linear system and the irradiance distribution $i(\mathbf{x}_i)$ of the imaged object distribution $o(\mathbf{x}_o)$ of an optical system is given by [2]

$$i(\mathbf{x}_i) = \int_{-\infty}^{\infty} o(\mathbf{x}_o) \cdot |P(\mathbf{x}_i, \mathbf{x}_o)|^2 d\mathbf{x}_o . \quad (1.1)$$

Note that the vectors \mathbf{x}_o and \mathbf{x}_i refer to the lateral, scale-normalized coordinates in the object and the image plane, respectively. The squared modulus of the transmission function, i.e. $h(\mathbf{x}_i, \mathbf{x}_o) = |P(\mathbf{x}_i, \mathbf{x}_o)|^2$, is referred to as the point spread function (PSF) of the optical system. It corresponds to the irradiance distribution in the image plane that is produced by a point source located at a position \mathbf{x}_o in the object plane. The imaging process can be considered as shift invariant if the shape of the PSF is (approximately) independent of the point source's position in the systems field of view or at least a sub-region thereof, which is a suitable approximation for well-corrected optical systems. In such an *isoplanatic region*, Eq. (1.1) can be written as

$$i(\mathbf{x}_i) = \int_{-\infty}^{\infty} o(\mathbf{x}_o) \cdot |P(\mathbf{x}_i - \mathbf{x}_o)|^2 d\mathbf{x}_o . \quad (1.2)$$

Accordingly, the image distribution $i(\mathbf{x}_i)$ is determined by a convolution of the object distribution $o(\mathbf{x}_o)$ and the system's PSF $h(\mathbf{x}_i)$. Under the assumption of small angles of diffraction, the transmission function $P(\mathbf{x})$ in an isoplanatic region corresponds to the Fourier transformation of the complex pupil field

$$p(\mathbf{x}_p) = a(\mathbf{x}_p) \cdot \exp\left(\frac{2\pi i}{\lambda} \cdot w(\mathbf{x}_p)\right), \quad (1.3)$$

which is defined on each image point's reference sphere in the exit pupil of the optical system. The amplitude function $a(\mathbf{x}_p)$ defines the shape of the exit pupil aperture and the phase is determined by the aberration function $w(\mathbf{x}_p)$. Note that λ denotes the considered wavelength. The convolution integral in Eq. (1.2) can be written as a simple product in the Fourier domain according to

$$I(\xi) = O(\xi) \cdot H(\xi), \quad (1.4)$$

where $I(\xi)$ and $O(\xi)$ correspond to the Fourier transformation of $i(\mathbf{x}_i)$ and $o(\mathbf{x}_o)$, respectively. The Fourier transformation of the PSF is referred to as the optical transfer function $H(\xi)$. Its modulus $M(\xi) = |H(\xi)|$, referred to as the modulation transfer function (MTF), provides the contrast reduction of a particular spatial frequency ξ that is imaged through the optical system. In the case of a circular exit pupil aperture, the modulation transfer function vanishes for frequencies larger than the cut-off frequency $\xi_0 = 2NA/\lambda$, which depends on the optical system's numerical aperture NA. Note that this corresponds to Abbe's well known bandwidth limit for optical imaging systems [3]. An overview of the defined imaging quantities and their relationship is illustrated in Fig. 1.1.

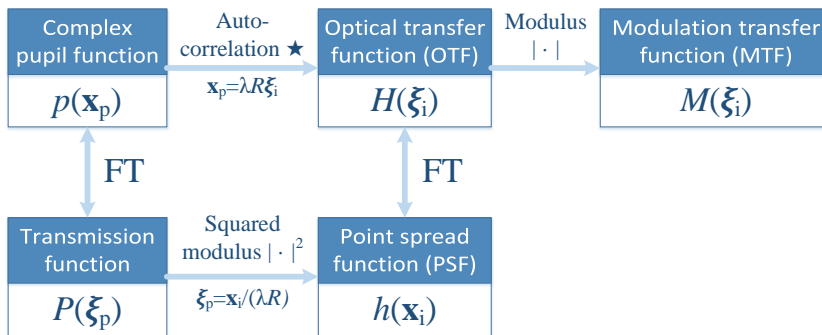


Figure 1.1: Illustration of the relationship between the complex pupil function $p(\mathbf{x}_p)$, the point spread function $h(\mathbf{x}_i)$ and the optical transfer function $H(\xi_i)$ of an imaging system. Note that FT denotes a Fourier transformation and R denotes the radius of the reference sphere in the exit pupil of the imaging system.

Conventional figures of merit to optimize an image's quality include the lateral extension of the PSF $h(\mathbf{x})$, the root-mean-square wavefront error of the complex pupil field $p(\mathbf{x}_p)$, or the value of the MTF $M(\xi)$ for a set of predefined spatial frequencies $\{\xi_j\}$. However, these classical figures of merit may not provide the best performance for extracting extended information of the imaged object scene beyond the two-dimensional object

distribution. Computational imaging describes a methodology that tailors the performance of an imaging system to advanced imaging and sensing tasks. In particular, it extends the conventional imaging process by considering a holistic system description including the optical image formation in combination with dedicated computer processing. Figure 1.2 illustrates the difference in the work flow between a conventional and a computational imaging system schematically.

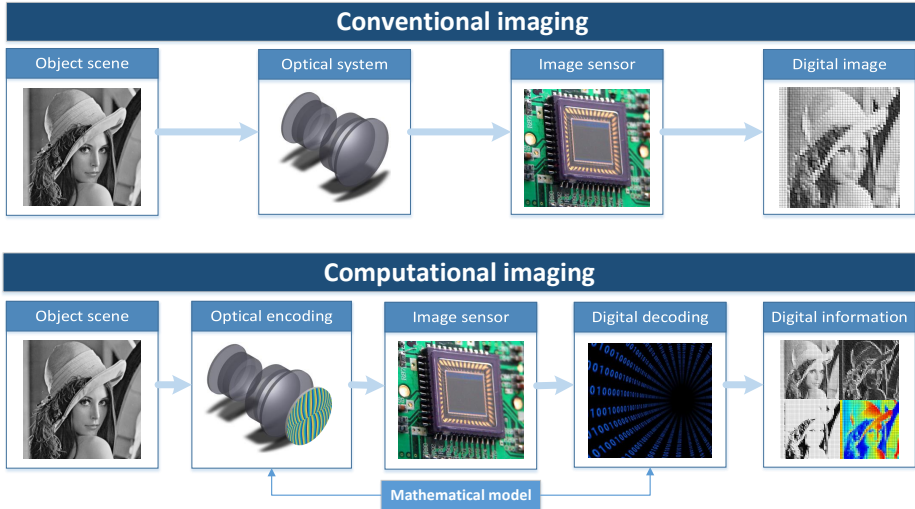


Figure 1.2: Overview of the work flow of a conventional imaging approach (top) in comparison to computational imaging approach (bottom). A conventional imaging system incorporates an optical system to generate a direct image of an object scene, which is digitally recorded using an image sensor. A computational imaging system generates an optically encoded image using specialized optical hardware components. The digitally recorded image is subsequently decoded using computational processing. Optical encoding and digital decoding are linked by a mathematical model and optimized jointly in order to extract advanced object information of interest.

A conventional system relies on a classical optical system such as a camera lens, a microscope objective or a telescope to form a direct image of the captured object scene onto an image sensor. A computational imaging system initially produces an optically encoded image. Hereby, the encoding is achieved by utilizing specialized optical hardware components within the imaging path. Alternatively, such components can be utilized in a dedicated illumination path in case an active light source is considered. In both cases, the general hardware may be based on traditional focusing optics that is modified by implementing phase and/or amplitude masks, diffusers, polarizers or gratings in the imaging and/or the illumination subsystem of the overall setup. Other specialized optical hardware utilizes novel, alternative architectures and imaging morphologies such as array optics (e.g. light-field cameras [4, 5]) as well as scanning (e.g. confocal scanning microscopy [6]), projection (e.g. computed tomography [7]) or lensless techniques [8]. After the image formation step, the optically encoded image is digitally decoded

using computational post-processing in order to extract the object information of interest. This processing relies on tailored algorithms that perform numerical computations such as deconvolutions, mapping, filtering and feature matching. A key aspect of the computational imaging chain is that the optical encoding and computational decoding processes are jointly developed and optimized in an integral design process. This necessitates that they are linked by a common mathematical model as indicated in Fig. 1.2. This model can be based on physical optics theorems, which may rely on ray tracing techniques or more sophisticated models such as scalar or vectorial diffraction theory [2]. In recent years, models have been developed based on artificial intelligence concepts including neural networks and deep learning [9]. These models provide a powerful tool, in particular for the case when the optical encoding cannot be properly described using physical theorems.

The computational imaging methodology allows for enhanced capabilities of the joint system in extracting information which cannot be accessed by purely classical imaging systems. In particular, it provides a tool for optical phase imaging and wavefront sensing [10] and it has been applied successfully in rendering imaging systems with a high dynamic range (HDR) [11], super-resolution [12, 13] or extended depth of field [14, 15]. Computational imaging systems are applied for three-dimensional [16, 17] and multi-spectral imaging [18, 19] as well as polarization sensing [20]. In addition, the computational imaging approach can be used to reduce the hardware complexity that would be required for a conventional optical system. For example, it can be applied for microscopic imaging without the need for an objective lens [8] or photography based on a single pixel detector [21]. A comprehensive review of computational imaging applications and associated key technologies is given in ref. [22].

1.1.2. POINT SPREAD FUNCTION ENGINEERING

This thesis focuses on one particular class of computational imaging systems. Here, the specialized hardware that implements the optical encoding (see Fig. 1.2) is based on a conventional optical imaging or illumination system in combination with a dedicated pupil mask. A wide range of terms is used in the literature to refer to this particular approach, including wavefront-coding [14], coded aperture imaging [9, 23], as well as point spread function or pupil engineering [24, 25]. The pupil mask alters the OTF $H(\xi)$ or, equivalently, the PSF $h(\mathbf{x})$ of the optical imaging or illumination system in a pre-defined manner as it modifies the amplitude and/or the phase of the light passing through the element. It is commonly placed in the pupil plane (or at a conjugate plane thereof) in order to ensure that an equal alteration of the PSF is achieved across the optical system's field of view. The pupil mask can be described by an additional complex function $m(\mathbf{x}_p)$, which is multiplied to the complex pupil field defined in Eq. (1.3) and results in an engineered pupil function

$$p_E(\mathbf{x}_p) = m(\mathbf{x}_p) \cdot a(\mathbf{x}_p) \cdot \exp\left(\frac{2\pi i}{\lambda} \cdot w(\mathbf{x}_p)\right). \quad (1.5)$$

The purpose of the complex mask function $m(\mathbf{x}_p)$ is to customize the optical system's PSF distribution $h(\mathbf{x})$ in order to allow for an optimized extraction of a particular type of information of an imaged object. This can either be done in terms of estimation theo-

retical bounds, i.e. the Cramér Rao lower bound [26], or in terms of practicality, e.g. by preventing complex numerical estimation problems.

The pupil mask can be practically implemented using different active and passive optical elements that can work in a reflection or a transmission configuration. Spatial light modulators (SLMs) are commonly used as they enable flexibly switching between different mask designs. Alternatively, a passive optical element that relies on a surface profile that is structured by lithography methods can be used. These elements constitute a less complex and more compact solution, albeit at the costs of a limited flexibility. The image formation step initially results in an optically encoded rather than a conventional, direct image of the object scene. Tailored computational image post-processing then needs to be applied to extract the particular object information of interest. This can be done by an appropriate mathematical model, commonly based on scalar diffraction theory and Fourier optics. More recent PSF engineered, computational imaging systems rely on machine learning concepts [27].

Using pupil engineering to extend the depth of focus of a conventional optical system is one of the earliest computational imaging application examples, which was originally proposed by Cathey and Dowski in 1995 [14]. The depth of focus can be described as the axial distance in object space over which the PSF remains highly confined. The depth of focus increases with a decreasing numerical aperture NA of the optical system. Accordingly, high resolution, light efficient systems that necessitate a high numerical aperture are, conventionally, limited by a short depth of focus. A tailored pupil mask can be used to maintain the PSF's confinement over a significantly larger axial range. Multiple pupil designs have been proposed using axicons [28], phase plates [14], diffusers [15], free-form optics [29] or tailored chromatic aberration [30]. The extended depth commonly comes at the price of an increased lateral PSF size at the axial, in-focus position. However, post-processing algorithms that are tailored to this particular PSF can be applied in order to mitigate the loss in lateral resolution [14, 29]. Extended depth of focus has been applied in a large range of imaging applications spanning microscopy [28], photography [15] and machine vision [31]. Furthermore, the approach made the transition into commercial products for consumer electronics [32] and machine vision systems [33].

A second prominent pupil engineering example is based on shaping the PSF to form a ring that features a central obscuration. Such PSFs can be generated using phase plates that introduce a vortex phase distribution to the incoming field [34]. One essential field of application is fluorescence microscopy, where pupil engineering is performed in the illumination subsystem of a microscope. The approach called stimulated emission depletion (STED) utilizes two pulsed light sources that spatially overlap in the plane, where the fluorescent sample is located [13]. The first one forms a conventional, single spot PSF for excitation whereas the second one features a ring shaped PSF for depletion of the fluorophores. The combination allows for the generation of fluorescence images with a nanometer scale resolution and, therefore, bypasses the classical Abbe diffraction limit [13]. Due to the significant impact of this super-resolution microscopy technique in the area of bio-medical imaging, the principle was awarded the Nobel Prize in Chemistry in 2014. This technique has been commercialized and represents a standard imaging mode of state-of-the-art fluorescence microscopy systems. Equivalent vortex phase elements that produce ring shape PSFs are also used in a completely different application

area. Coronagraphs enable the imaging of very faint objects even if they are located in close proximity to a very bright light source, which would normally obscure the object due to its glare [35]. These systems are particularly relevant for the field of astronomy, where it is applied for imaging the sun's corona or detecting extrasolar planets. Here, the engineered, ring-shaped PSF provides the optical tool for discriminating the light of an extrasolar planet from the host star [36, 37].

In summary, computational imaging using a PSF engineering approach benefits a large range of applications. Several particular implementations of engineered PSFs have been proposed in the context of computational imaging, e.g. featuring an extended depth of focus or a central obscuration. The field of application of the individual implementations commonly covers multiple, classical areas of optical imaging ranging from microscopy through photography and astronomy.

1.1.3. HELICAL POINT SPREAD FUNCTIONS

In recent years, a novel class of engineered point spread functions, referred to as helical PSFs, has gained increased interest [38–45]. The working principle of these PSFs in comparison to a conventional PSF is schematically illustrated in Fig. 1.3.

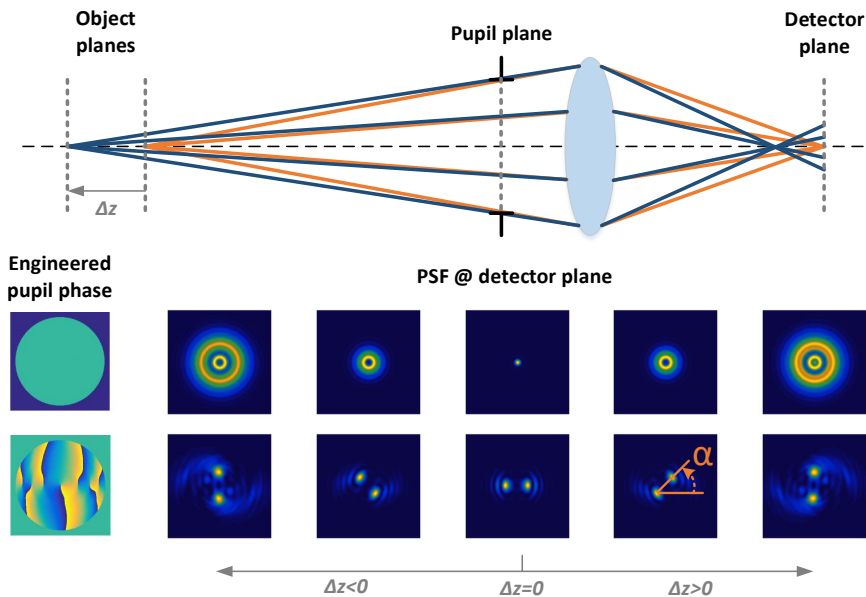


Figure 1.3: Working principle for measuring an axial shift Δz of an object point with respect to the in-focus plane using a pupil engineered, optical imaging system. In contrast to the blurring of a conventional optical system's single spot PSF (top row), the engineered, helical PSF (bottom row) provides two distinct spots that rotate around a common axis with a changing shift Δz . The rotation angle α can directly be associated with a shift Δz in an unambiguous range of $-90^\circ \leq \alpha \leq 90^\circ$.

The PSF of an idealized, conventional optical system forms a single, well-confined irradiance peak if an in-focus ($\Delta z = 0$) object point is imaged. The size of this spot is increasing, if the object point is shifted away from the in-focus position ($|\Delta z| > 0$), and a conventional PSF blurring is observed. In contrast, the engineered, helical PSF features multiple, laterally separated peaks for an in-focus, axial object point location. The most unique characteristic of this kind of PSF is its behavior if the object point is moved away from the in-focus position. In particular, the PSF peaks rotate in a helical manner, which is exemplary shown in the bottom part of Fig. 1.3. Here, an engineered pupil phase design that generates a double-helix PSF distribution is shown. This particular design exhibits two peaks that rotate around a common axis. In comparison to the fast lateral spreading of the conventional, single-spot PSF, the two peaks remain well confined even for a substantial amount of defocus Δz . Accordingly, this type of engineered PSF establishes a simple, direct relationship between the distance of an object point and the angle α between the PSF peaks and a reference in-plane axis over an extended axial range. If this relationship is known, e.g. through an initial system calibration step, this unique characteristic enables a simple and unambiguous depth estimation (of a point source object) using a single detector image without the need for an elaborate, numerical estimation model [46].

The theoretical fundamentals of wave fields featuring multiple irradiance spots that rotate during propagation was originally introduced by Piestun et. al [47]. In particular, the authors proposed the first method for generating and modeling the propagation of these distributions based on a superposition of a tailored set of Gauss-Laguerre modes. The concept of using such distributions, i.e. featuring two irradiance peaks, for measuring depth was initially proposed by Greengard et. al [46]. In the following years, new design methods for generating helical PSFs have been proposed and further optimized [24, 48] in order to improve the light efficiency of the utilized pupil masks. This is achieved by pupil mask designs that rely on a pure phase modification in the pupil plane. Double-helix PSFs with two rotating spots have been widely studied and successfully applied for three-dimensional, point emitter localization and tracking with high depth resolution and an extended depth of focus [39, 40, 42, 49, 50]. In fact, it has been shown that an optical system with a double-helix PSF provides an improved precision limit, i.e. with respect to the Cramér Rao lower bound, for estimating the axial distance of an object point over an extended depth range compared to a conventional PSF [46]. It also offers superior precision limits for high signal-to-background ratio application scenarios in comparison to competing monocular concepts, including astigmatic or bi-plane methods [51, 52]. In contrast to these methods, it provides an almost constant localization precision in all three spatial dimensions.

The continuous interest in these kind of pupil engineered imaging systems, i.e. in the area of super resolution microscopy, led to the foundation of the start-up company *Double Helix Optics*. The company commercializes the application of helical PSFs for three-dimensional particle-localization and targets applications in the area of super-resolution microscopy [53]. The high potential of the approach was further acknowledged as the company's main product was awarded with the SPIE Prism award for the best new optics and photonics product on the market in the area of diagnostics and therapeutics.

1.2. MOTIVATION AND OUTLINE

The research conducted in the frame of this thesis focuses on pupil engineered, computational imaging systems that rely on the use of helical PSFs. These types of PSFs have been studied and applied for more than a decade and it has been demonstrated that they provide unique benefits for addressing optical depth measurement and three-dimensional localization problems. The continuous research interest and the successful commercialization demonstrate the enormous potential of this concept. So far, its utilization is primarily limited to a single area of application, i.e. super-resolution microscopy. However, pupil engineering using helical PSFs provides a much more general, versatile tool for computational imaging and sensing tasks. It facilitates a unique way of directly retrieving depth information from a simple PSF rotation angle measurement using a basic, linear relationship. Although its benefits have been primarily demonstrated in the frame of super-resolution microscopy, in general, they can be transferred to other areas of optical imaging. This is analogous to the pupil engineering concepts described in section 1.1.2. PSFs featuring an extended depth of focus or a central obscuration are utilized in multiple optical imaging application fields. Accordingly, the main motivation of the research performed here is to expand the application scope of helical PSFs and to address challenges in different areas of optical imaging and sensing beyond super-resolution microscopy. In particular, two optical imaging and sensing tasks shall be addressed.

The first task that shall be addressed is three-dimensional imaging and sensing in the particular context of machine vision applications. The acquisition of three-dimensional object information is a key technology for human-machine interaction and autonomous driving. It provides machines, including robots and autonomous vehicles, with the ability to properly orientate in a three-dimensional environment, as well as the capability of tracking and interacting with three-dimensional objects. In addition, three-dimensional imaging is an essential tool for the projection and the embedding of virtual content for extended reality application scenarios.

The second imaging task of interest corresponds to the measurement of an optical wavefront, which is a fundamental technology in multiple engineering disciplines. It is utilized as a metrology tool for precise, three-dimensional shape characterizing and inspection. Furthermore, it is used for evaluating and optimizing the image quality performance of optical setups and it allows for controlling adaptive optical systems.

Pupil engineering using helical PSFs has the potential to provide a powerful tool with unique benefits for these two optical imaging and sensing tasks. In general, it offers significant advantages for respective imaging systems as it provides a high level of compactness and a low hardware complexity, which further relates to physical robustness and high cost-efficiency. In order to make this technology applicable to these two application scenarios, however, multiple shortcomings in the current computational imaging application approach of helical PSFs need to be addressed.

1.2.1. DEPTH RETRIEVAL FOR EXTENDED OBJECTS

Currently, the application scope of helical PSFs is mainly limited to the microscopic detection of single particles or clusters thereof. The main reason for the narrow scope relies on the interplay between the spatial features of the object of interest and the engineered

PSF during the imaging process. Single particles provide distinct, point-like spatial features. The essential benefit of this aspect is shown in the top part of Fig. 1.4, which schematically illustrates imaging an exemplary cluster of particles using a double-helix PSF. The encoded image can be modeled by a mathematical convolution of the helical PSF and the object distribution according to Eq. (1.2). In fact, the encoded image of an individual particle closely reassembles the actual engineered PSF shape. Accordingly, the PSF rotation angle α is directly visible and can be extracted using conventional image segmentation and peak detection algorithms. The particle's axial focus position Δz can then be retrieved using the calibrated relationship $\Delta z(\alpha)$.

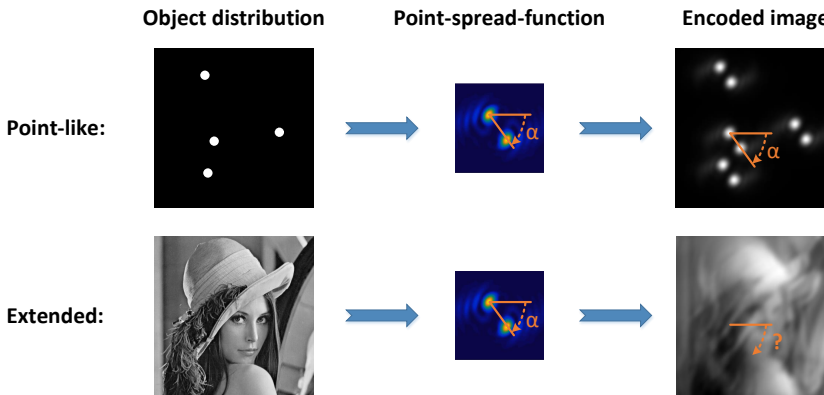


Figure 1.4: Illustration of the rotation angle α retrieval approach using helical PSFs for point-like objects (top) and extended scenes (bottom). Object and PSF spatial features are well separated for the case of point-like objects. The PSF rotation angle α , which directly corresponds to the object distance, can directly be obtained from the encoded image using conventional image segmentation and peak detection algorithms. In contrast, object and PSF spatial features are interlaced for the case of an extended object and the PSF rotation angle α cannot directly be retrieved.

The bottom part of Fig. 1.4 illustrates a scenario related to imaging an extended object distribution. In this case, the spatial features of the object distribution and the engineered PSF are interlaced as a result of the convolution. The PSF shape is not directly visible in the encoded image and the extraction of the PSF rotation angle α is not straightforward as in the previous case. A first attempt to separate spatial object and PSF features for imaging an extended object distribution has been proposed in ref. [54]. However, the utilized computational imaging system approach relies on the acquisition of multiple images using different pupil phase distributions, which provides a severe drawback i.e. for real-time imaging applications. Therefore, novel image processing concepts need to be explored in order to enable the application of helical point spread functions for single-shot, three-dimensional imaging of practical, extended objects. In particular, an approach needs to be developed that allows for separating (lateral) object features from PSF features in order to retrieve the object's depth information in a single acquisition. It is mentioned here that the term "three-dimensional imaging", as it is used in the frame of this thesis, refers to the acquisition of a unique depth information for each lateral

image position \mathbf{x}_i . It is also referred to as "2.5D imaging" for the machine vision applications addressed here and it does not refer to the extraction of the full, volumetric three-dimensional information of an object scene.

1.2.2. PRACTICAL PUPIL PHASE IMPLEMENTATION

Another shortcoming in the current application of helical PSFs for (super-resolution) microscopy applications corresponds to the practical implementation of the pupil engineered phase distribution. Commonly, a spatial light modulator (SLM), which is integrated inside a microscope's imaging path, is incorporated to generate the helical PSF distribution. However, the utilization of an SLM generally results in expensive and bulky optical imaging systems and requires a dedicated polarization state as well as a narrow spectral bandwidth of the incident light. In addition, SLMs provide a reduced light efficiency due to the limited fill factor of the individual elements of the modulator array.

Therefore, the application of helical PSFs for three-dimensional imaging in the context of machine vision is currently not feasible as this application demands for highly integrated, robust and cost-efficient optical setups. An alternative, practical implementation method for compact phase elements relies on the use of optical lithography fabrication techniques. Lithographic elements can be designed and manufactured to provide a high light efficiency and an operation over a broad spectral bandwidth. Initial results using optical lithography for the fabrication of phase elements to generate helical PSFs have been presented in ref. [48]. However, the incorporated phase elements are subject to severe limitations related to the available lateral extension, robustness and cost-efficiency. Therefore, their applicability for machine vision tasks is limited and the development as well as the demonstration of novel manufacturing approaches that overcome these limitations are required.

1.2.3. IMPROVED ABERRATION ROBUSTNESS

So far, only idealized optical systems have been considered in the context of computational imaging using helical PSFs. In particular, a diffraction limited imaging performance has been assumed in the literature. This can be considered an adequate assumption in the context of super-resolution microscopy since highly corrected objective lenses are used. In contrast, optical imaging systems used for machine vision applications generally do not operate in a diffraction limited regime and the image quality is limited by aberrations. In fact, these aberrations may distort the shape of a helical PSF and ultimately falsify the depth measurement in three-dimensional imaging applications. This is particularly harmful if it concerns field dependent aberrations as the depth estimation is deteriorated by a field-dependent bias. For example, objects at the edge of the field may appear closer than they actually are. In order to utilize computational imaging systems using helical PSFs for machine vision applications, a holistic optical design approach that considers the effect of aberrations on the depth retrieval accuracy needs to be developed. To this end, it is essential to identify which aberrations are most critical with respect to the rotation angle of a particular helical PSF design. This provides the basis for an optimized balancing of different aberrations during the optical design process. At the same time, new phase element designs that lead to a helical PSF rotation with increased aberration robustness may need to be explored.

1.2.4. WAVEFRONT RETRIEVAL FOR EXTENDED OBJECTS

The retrieval of depth information using pupil engineered computational imaging systems can be interpreted as a measurement of defocus aberration of an optical setup. This aberration is associated with a quadratic phase contribution of an optical wavefront, which leads to the rotation of a helical PSF as illustrated in Fig. 1.3. The question arises if more general information on an optical wavefront can be retrieved using helical PSFs, which constitutes the second optical imaging task that shall be addressed in the frame of this thesis. A multitude of approaches exists to measure an optical wavefront based on imaging a point object. However, such distinct objects are not always available in applications such as metrology, surveillance, or earth observation. Furthermore, the respective optical systems feature an extended field of view with field dependent aberrations. Only a few measurement methods are available if the wavefront emerges from an unknown, extended object distribution. They generally rely on imaging the extended scene and, similar to the depth retrieval problem illustrated in Fig. 1.4, necessitate the separation of spatial PSF and object features in order to retrieve the (field-dependent) wavefront information. Conventional image processing approaches require complex, iterative optimization routines that are very susceptible to the proper choice of regularization parameters. Moreover, the need for multiple iteration steps prevents their use for real-time wavefront measurements applications. Pupil engineered, computational imaging systems featuring helical PSFs provide the potential to overcome the need for such a complex and iterative image processing task in order to extract the (field-dependent) wavefront of an extended scene. Yet, a novel, more elaborate system approach needs to be developed that exploits general shape characteristics of helical PSFs beyond the commonly utilized relationship between the defocus aberration and the rotation angle.

1.2.5. OUTLINE OF THESIS

A computational imaging approach for acquiring three-dimensional object information based on the use of helical PSFs is initially presented in chapter 2 of this thesis. To this end, a novel image processing work flow is developed that enables to overcome the major challenge of retrieving the PSF rotation angle from the pupil engineered image of an extended object distribution. Two implementation approaches that enable the practical realization of highly integrated, robust and cost-efficient phase elements are investigated in the following two chapters. A novel fabrication scheme that applies a femto-second laser direct writing technique is developed in chapter 3. A second manufacturing process that incorporates a combination of optical lithography and UV-replication on a waver scale is demonstrated in chapter 4. In addition, the shortcoming of existing pupil engineered systems using helical PSFs with respect to optical aberrations is addressed in chapter 4. In particular, a new method for designing pupil masks that allow for the generation of multi-order-helix PSFs with superior aberration robustness is presented. Furthermore, a computational imaging approach is developed in chapter 5, which utilizes helical PSFs to estimate general wavefront aberrations based on the acquisition of an extended, unknown object scene. Finally, chapter 6 provides a summary and a discussion of the results obtained in the frame of this thesis.

REFERENCES

- [1] B. Marr, *The 7 biggest technology trends in 2020 everyone must get ready for now*, *Forbes* (September 30th, 2019).
- [2] M. Born, E. Wolf, A. B. Bhatia, P. C. Clemmow, D. Gabor, A. R. Stokes, A. M. Taylor, P. A. Wayman, and W. L. Wilcock, *Principles of Optics*, 7th ed. (Cambridge University Press, 2013).
- [3] E. Abbe, *Beiträge zur theorie des mikroskops und der mikroskopischen wahrnehmung*, *Archiv für Mikroskopische Anatomie* **9**, 413 (1873).
- [4] J. Tanida, T. Kumagai, K. Yamada, S. Miyatake, K. Ishida, T. Morimoto, N. Kondou, D. Miyazaki, and Y. Ichioka, *Thin observation module by bound optics (tombo): Concept and experimental verification*, *Applied Optics* **40**, 1806 (2001).
- [5] T. E. Bishop and P. Favaro, *The light field camera: extended depth of field, aliasing, and superresolution*, *IEEE Transactions on Pattern Analysis and Machine Intelligence* **34**, 972 (2012).
- [6] M. Minsky, *Memoir on inventing the confocal scanning microscope*, *Scanning* **10**, 128 (1988).
- [7] J. M. Schmitt, *Optical coherence tomography (oct): a review*, *IEEE Journal of Selected Topics in Quantum Electronics* **5**, 1205 (1999).
- [8] A. Ozcan and E. McLeod, *Lensless imaging and sensing*, *Annual review of biomedical engineering* **18**, 77 (2016).
- [9] G. Barbastathis, A. Ozcan, and G. Situ, *On the use of deep learning for computational imaging*, *Optica* **6**, 921 (2019).
- [10] J. R. Fienup, *Reconstruction of an object from the modulus of its fourier transform*, *Optics Letters* **3**, 27 (1978).
- [11] R. Horstmeyer, G. Euliss, R. Athale, and M. Levoy, *Flexible multimodal camera using a light field architecture*, in *2009 IEEE International Conference on Computational Photography (ICCP), San Francisco, CA, 2009*, pp. 1–8.
- [12] E. Betzig, G. H. Patterson, R. Sougrat, O. W. Lindwasser, S. Olenych, J. S. Bonifacino, M. W. Davidson, J. Lippincott-Schwartz, and H. F. Hess, *Imaging intracellular fluorescent proteins at nanometer resolution*, *Science (New York, N.Y.)* **313**, 1642 (2006).
- [13] T. A. Klar, S. Jakobs, M. Dyba, A. Egner, and S. W. Hell, *Fluorescence microscopy with diffraction resolution barrier broken by stimulated emission*, *Proceedings of the National Academy of Sciences* **97**, 8206 (2000).
- [14] E. R. Dowski and W. T. Cathey, *Extended depth of field through wave-front coding*, *Applied Optics* **34**, 1859 (1995).

- [15] O. Cossairt, C. Zhou, and S. Nayar, *Diffusion coded photography for extended depth of field*, in *ACM SIGGRAPH 2010 Papers*, SIGGRAPH '10 (Association for Computing Machinery, New York, NY, USA, 2010).
- [16] H. Arimoto and B. Javidi, *Integral three-dimensional imaging with digital reconstruction*, *Optics Letters* **26**, 157 (2001).
- [17] X. Xiao, B. Javidi, M. Martinez-Corral, and A. Stern, *Advances in three-dimensional integral imaging: sensing, display, and applications invited*, *Applied Optics* **52**, 546 (2013).
- [18] A. Wagadarikar, R. John, R. Willett, and D. Brady, *Single disperser design for coded aperture snapshot spectral imaging*, *Applied Optics* **47**, B44 (2008).
- [19] M. E. Gehm, R. John, D. J. Brady, R. M. Willett, and T. J. Schulz, *Single-shot compressive spectral imaging with a dual-disperser architecture*, *Optics express* **15**, 14013 (2007).
- [20] T. Colomb, P. Dahlgren, D. Beghuin, E. Cuche, P. Marquet, and C. Depeursinge, *Polarization imaging by use of digital holography*, *Applied Optics* **41**, 27 (2002).
- [21] M. F. Duarte, M. A. Davenport, D. Takhar, J. N. Laska, T. Sun, K. F. Kelly, and R. G. Baraniuk, *Single-pixel imaging via compressive sampling*, *IEEE Signal Processing Magazine* **25**, 83 (2008).
- [22] J. N. Mait, G. W. Euliss, and R. A. Athale, *Computational imaging*, *Advances in Optics and Photonics* **10**, 409 (2018).
- [23] M. J. Cieřlak, K. A. Gamage, and R. Glover, *Coded-aperture imaging systems: Past, present and future development – a review*, *Radiation Measurements* **92**, 59 (2016).
- [24] S. Prasad, *Rotating point spread function via pupil-phase engineering*, *Optics Letters* **38**, 585 (2013).
- [25] S. Quirin, G. Grover, and R. Piestun, *Optimal 3d single-molecule super-resolution microscopy with engineered point spread functions*, in *Proceedings - International Symposium on Biomedical Imaging* (2012) pp. 926–927.
- [26] S. M. Kay, *Fundamentals of statistical signal processing: Estimation theory*, Vol. 1 (Prentice-Hall, US, 1993).
- [27] E. Hershko, L. E. Weiss, T. Michaeli, and Y. Shechtman, *Multicolor localization microscopy and point-spread-function engineering by deep learning*, *Optics express* **27**, 6158 (2019).
- [28] G. Thériault, Y. de Koninck, and N. McCarthy, *Extended depth of field microscopy for rapid volumetric two-photon imaging*, *Optics express* **21**, 10095 (2013).

- [29] V. Sitzmann, S. Diamond, Y. Peng, X. Dun, S. Boyd, W. Heidrich, F. Heide, and G. Wetzstein, *End-to-end optimization of optics and image processing for achromatic extended depth of field and super-resolution imaging*, *ACM Transactions on Graphics* **37**, 1 (2018).
- [30] F. Guichard, H.-P. Nguyen, R. Tessières, M. Pyanet, I. Tarchouna, and F. Cao, *Extended depth-of-field using sharpness transport across color channels*, in *Digital Photography V*, SPIE Proceedings, edited by B. G. Rodricks and S. E. Süsstrunk (SPIE, 2009) p. 72500N.
- [31] T. Sakuyama, T. Funatomi, M. Iiyama, and M. Minoh, *Diffraction-compensating coded aperture for inspection in manufacturing*, *IEEE Transactions on Industrial Informatics* **11**, 782 (2015).
- [32] S. Litchfield, *Edof versus auto-focus: Understanding the compromises involved*, (2011).
- [33] *Ricoh's next-generation machine vision: A window on the future*, (2016).
- [34] M. Padgett, J. Courtial, and L. Allen, *Light's orbital angular momentum*, *Physics Today* **57**, 35 (2004).
- [35] B. Lyot, *Optical apparatus with wide field using interference of polarized light*, *C. R. Acad. Sci. Paris* **197**, 1593 (1933).
- [36] G. Foo, D. M. Palacios, and G. A. Swartzlander, *Optical vortex coronagraph*, *Optics Letters* **30**, 3308 (2005).
- [37] A. Aleksanyan, N. Kravets, and E. Brasselet, *Multiple-star system adaptive vortex coronagraphy using a liquid crystal light valve*, *Physical review letters* **118**, 203902 (2017).
- [38] G. Grover and R. Piestun, *New approach to double-helix point spread function design for 3d super-resolution microscopy*, *Proc. of SPIE* **8590**, 85900M (2013).
- [39] S. Quirin, G. Grover, and R. Piestun, *Optimal 3d single-molecule super-resolution microscopy with engineered point spread functions*, *Proceedings - International Symposium on Biomedical Imaging* **109**, 926 (2012).
- [40] A. Barsic, G. Grover, and R. Piestun, *Three-dimensional super-resolution and localization of dense clusters of single molecules*, *Scientific reports* **4**, 5388 (2014).
- [41] C. Roider, A. Jesacher, S. Bernet, and M. Ritsch-Marte, *Axial super-localisation using rotating point spread functions shaped by polarisation-dependent phase modulation*, *Optics express* **22**, 4029 (2014).
- [42] C. Roider, R. Heintzmann, R. Piestun, and A. Jesacher, *Deconvolution approach for 3d scanning microscopy with helical phase engineering*, *Optics express* **24**, 15456 (2016).

- [43] C. Roider, R. Piestun, and A. Jesacher, *3d image scanning microscopy with engineered excitation and detection*, *Optica* **4**, 1373 (2017).
- [44] A. R. Carr, A. Ponjavic, S. Basu, J. McColl, A. M. Santos, S. Davis, E. D. Laue, D. Klennerman, and S. F. Lee, *Three-dimensional super-resolution in eukaryotic cells using the double-helix point spread function*, *Biophysical Journal* **112**, 1444 (2017).
- [45] Z. Wang, Y. Cai, Y. Liang, X. Zhou, S. Yan, D. Dan, P. R. Bianco, M. Lei, and B. Yao, *Single shot, three-dimensional fluorescence microscopy with a spatially rotating point spread function*, *Biomedical optics express* **8**, 5493 (2017).
- [46] A. Greengard, Y. Y. Schechner, and R. Piestun, *Depth from diffracted rotation*, *Optics Letters* **31**, 181 (2006).
- [47] R. Piestun, Y. Y. Schechner, and J. Shamir, *Propagation-invariant wave fields with finite energy*, *Journal of the Optical Society of America A* **17**, 294 (2000).
- [48] G. Grover, S. Quirin, C. Fiedler, and R. Piestun, *Photon efficient double-helix psf microscopy with application to 3d photo-activation localization imaging*, *Biomedical optics express* **2**, 3010 (2011).
- [49] S. R. P. Pavani and R. Piestun, *Three dimensional tracking of fluorescent microparticles using a photon-limited double-helix response system*, *Optics express* **16**, 22048 (2008).
- [50] S. R. P. Pavani, M. A. Thompson, J. S. Biteen, S. J. Lord, N. Liu, R. J. Twieg, R. Piestun, and W. E. Moerner, *Three-dimensional, single-molecule fluorescence imaging beyond the diffraction limit by using a double-helix point spread function*, *Proceedings of the National Academy of Sciences of the United States of America* **106**, 2995 (2009).
- [51] G. Grover, S. R. P. Pavani, and R. Piestun, *Performance limits on three-dimensional particle localization in photon-limited microscopy*, *Optics Letters* **35**, 3306 (2010).
- [52] M. Badieirostami, M. D. Lew, M. A. Thompson, and W. E. Moerner, *Three-dimensional localization precision of the double-helix point spread function versus astigmatism and biplane*, *Applied Physics Letters* **97** (2010), 10.1063/1.3499652.
- [53] G. Dutton, *Imaging module gives 2d microscopes 3d vision*, *Genetic Engineering & Biotechnology News* **40** (05/04/2020).
- [54] S. Quirin and R. Piestun, *Depth estimation and image recovery using broadband, incoherent illumination with engineered point spread functions invited*, *Applied Optics* **52**, A367 (2013).

2

SINGLE SHOT THREE-DIMENSIONAL IMAGING USING AN ENGINEERED POINT SPREAD FUNCTION

A system approach to acquire a three-dimensional object distribution is presented using a compact and cost efficient camera system with an engineered point spread function. The corresponding monocular setup incorporates a phase-only computer-generated hologram in combination with a conventional imaging objective in order to optically encode the axial information within a single two-dimensional image. The object's depth map is calculated using a novel approach based on the power cepstrum of the image. The in-plane RGB image information is restored with an extended depth of focus by applying an adapted Wiener filter. The presented approach is tested experimentally by estimating the three-dimensional distribution of an extended passively illuminated scene.

Parts of this chapter have been published as R. Berlich, A. Bräuer, and S. Stallinga, Opt. Express **24**, 5946–5960 (2016) [1].

2.1. INTRODUCTION

The ability to acquire depth information in a single shot in addition to the conventional two-dimensional image of an object scene is of increased interest in modern applications for consumer electronics, bio-medical imaging, machine vision and automotive engineering. Depending on the particular application, optical system solutions rely on active or passive illumination. The former approach incorporates a tailored, artificial light source in addition to an image acquisition module to extract the depth information of an object. Existing technologies include structured light [2], time-of-flight (Lidar) [3] as well as interferometry [4]. Passive illumination methods purely rely on ambient light and thus generally benefit from reduced energy consumption and system complexity, as well as robustness with respect to stray light. Most common solutions are based on multi-aperture approaches, i.e. stereo setups. The major disadvantage of these setups is the necessity for multiple optical systems and image sensors that result in increased costs, higher complexity and the need for an elaborate calibration [5]. In contrast, conventional single aperture approaches based on depth from focus (DFF) or depth from defocus (DFD) extract depth information by analyzing the axially dependent image blur or by searching for the in-focus state of the imaging system, respectively [6]. These configurations provide less complexity, but commonly suffer from low axial precision or require multiple acquisitions [7]. An approach that enables combining the advantages of monocular and stereo systems is based on the integration of a diffraction grating in front of a single imaging configuration [8, 9]. But the utilization of higher diffraction orders in order to generate a stereo pair results in a significant spectral dependence of the image disparity. Accordingly, the method requires a quasi-monochromatic illumination or prior knowledge on the object spectrum in order to retrieve well-defined depth information. In the past decade, plenoptic cameras have been of increased interest due to their rather simple, cost efficient setup. However, the inherent loss in lateral object resolution due to the optical demagnification by the microlens array represents a severe drawback [10, 11].

An alternative method for acquiring three-dimensional object information utilizes temporally or spatially engineered point spread functions (PSFs). Temporal PSF engineering techniques exploit a tailored focus sweep to generate a depth dependent PSF distribution with an extended depth of focus, which requires complex and costly opto-mechanical components such as piezo-electric actuators or deformable lenses [12, 13]. Various spatially tailored PSFs have been proposed in order to enhance the depth discrimination capabilities of depth-from-defocus systems. In [14], adapted aperture masks are utilized to extract depth information, but severely reduce the light efficiency of an optical system. In order to overcome this constraint, complex segmented optical elements within the pupil can be employed to achieve an extended depth of focus, but only provide low depth discrimination [15]. Moreover, the respective PSF engineering approaches commonly require extensive computational effort due to the incorporated iterative error minimization methods [13–15].

A novel PSF engineering approach has been demonstrated by Piestun and coworkers, which utilizes a rotating double helix PSF [16, 17]. The corresponding system has been applied successfully in the area of microscopy, demonstrating an extended depth of focus and a high depth resolution for 3D single-molecule localization [18, 19]. Moreover,

the general feasibility for broadband, passive cameras has been verified [20]. However, the applicability to commercial camera systems, e.g. in the area of consumer electronics or machine vision, is strongly limited. The necessity of multiple image acquisitions in order to retrieve the axial and lateral object information represents a major drawback of the system and restricts its application to (near) static object scenes. Additional minor drawbacks of these systems include the complex and costly setup, as well as the low light efficiency due to the incorporated spatial light modulator, which requires polarization filtering. A similar system based on four rotating PSF peaks has been developed by Niihara et. al [21], which enables single shot depth acquisition. But in addition to the costly numerical reconstruction approach, the respective pupil elements are not optimized for an extended rotation range, which significantly limits the retrievable depth range.

Here, we present a closed system approach based on the combination of a compact cost efficient optical setup and customized image processing that enables obtaining three-dimensional, broadband (RGB) object information from a single image. In particular, we show how the image's power cepstrum can be used to retrieve the axially dependent PSF parameters, which encode the object's depth information, with low computational effort. Based on the obtained parameters, the lateral scene can be reconstructed by a tailored Wiener filter, which, in contrast to the filter proposed in [17, 20], does not require an additional reference frame.

Initially, the concept of the proposed image acquisition approach is presented and a simplified imaging model to describe the hybrid optical system is established. The work flow of the applied image processing steps, including the depth map retrieval and the object reconstruction, is subsequently described. In the final section, experimental results of a developed demonstration system are presented, which verify the applied system approach.

2.2. SYSTEM APPROACH

2.2.1. IMAGING SETUP

The general image acquisition setup is schematically shown in Fig. 2.1. A passively illuminated, three-dimensional object is imaged on a conventional image sensor. The hybrid optical system is based on a conventional camera objective in combination with a computer-generated hologram (CGH). The thin holographic element is located directly at the objective's aperture stop position in order to ensure a field independent transmission. The particular design of the CGH is based on the approach presented in [16]. An initial estimate is obtained analytically based on a tailored superposition of Gauss-Laguerre modes with respective indices (2,2), (4,6), (6,10), (8,14) and (10, 18). Subsequently, a phase-only element is retrieved by further iterative optimization. The element modifies the phase of the transmitted light, which results in characteristic spiral exit pupil phase distributions that are exemplarily shown in Fig. 2.2(a) for an in- and out-of-focus object point. The corresponding double-helix shaped PSF distribution features a depth dependent rotation with an extended depth of focus. When an extended object distribution is imaged, the depth dependence is encoded within the recorded two-dimensional image. By decoding this raw image, both the depth map and the lateral object information can be extracted.

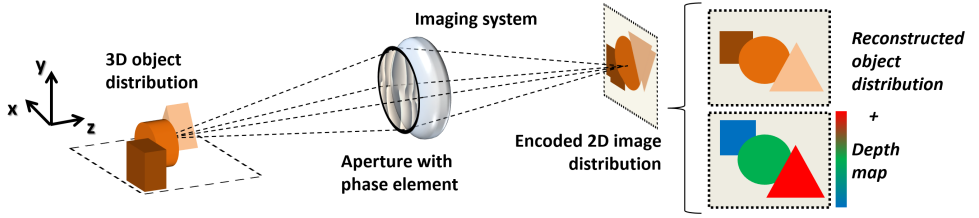


Figure 2.1: Schematic layout of the proposed image acquisition setup. A 3D object distribution is imaged by a conventional camera objective with an implemented glass substrate comprising the CGH surface profile. The lateral and axial object information is optically encoded within the raw image due to an engineered PSF and can be recovered by tailored image processing.

In contrast to the spatial light modulator used in [20], the presented setup incorporates a thin glass substrate with a structured surface profile, which provides a more compact and robust system solution. The glass element can be used with a broader temperature range and without the need for a polarization filter, which decreases the light efficiency. The profile is generated in two steps utilizing cost efficient, state-of-the-art wafer level technology that enables the processing of multiple-elements in a single iteration. Initially, a master sample is fabricated inside a photo resist layer using a novel grayscale, LED writing lithography system [22]. In particular, the utilized system provides a high accuracy, characterized by a lateral resolution below $1 \mu\text{m}$, a low wave front error of manufactured CGHs, and a highly dynamic dosage control. In comparison to the system applied in [23], the increased lateral processing area (11x) and the improved positioning accuracy (2x) enables highly parallelized, more cost efficient manufacturing of the CGH master samples. Using reactive-ion-etching or mask imprinting technology, the obtained profile is subsequently transferred onto the targeted substrate, which is diced in order to obtain the final elements. Ultimately, they are directly implemented inside a commercial camera objective. Note that the optical parameters (e.g. focal length, F-number) can be tailored to particular application needs. The optical setup is similar to the coded aperture configuration proposed in [14], which incorporates an adapted aperture mask. However, the systems light efficiency is significantly increased, due to the utilization of a phase-only element. In addition, the more confined double-helix PSF distribution inherently provides a higher lateral resolution.

2.2.2. IMAGE ACQUISITION

The proposed setup is modeled as an incoherent imaging system, described by [20]

$$\mathbf{i} = \{i_{kl}\} = \int_{-\infty}^{+\infty} \mathbf{o}(z) * \mathbf{h}(z) dz + \mathbf{n} , \quad (2.1)$$

where \mathbf{i} is the discretely sampled coded image distribution, $\mathbf{o}(z)$ is the object's discrete surface brightness, $\mathbf{h}(z)$ is the engineered point spread function and \mathbf{n} describes an additive noise term. Note that $*$ denotes the discrete lateral convolution integral with the laterally shift-invariant and axially shift-variant PSF. In the following, the indices (k, l) denote the pixel indexing within the discretely sampled, two-dimensional distributions.

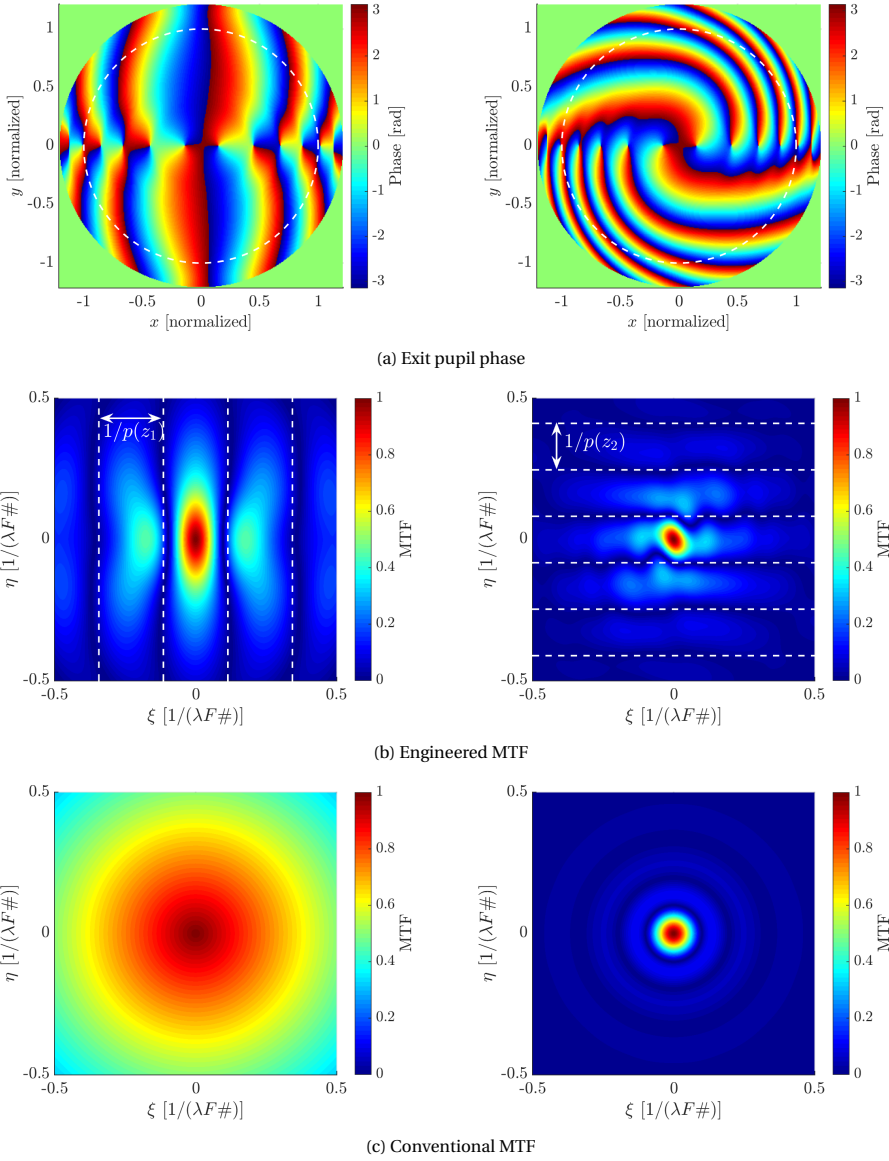


Figure 2.2: The phase distribution in the exit pupil plane of the hybrid optical system (a), the corresponding Modulation Transfer Function (MTF) (b), as well as the MTF of a conventional optical system (c) are plotted for an exemplary in- and out-of-focus object distance z_1 and z_2 , respectively. Note that the CGH is slightly oversized with respect to the actual pupil size, which is indicated by the dashed circle in (a). The spatial frequencies of the displayed MTFs are normalized according to the optical cut-off frequency given by the wavelength λ and the system's F-number. The engineered MTFs, shown in (b), exhibit a characteristic modulation with an axially dependent period $1/p(z)$ and orientation angle θ .

According to the design of the CGH, the axial dependence of the PSF can be described by a combination of a rotation and a lateral scaling of the double peak separation. At the same time, the engineered PSF inherently extends the system's depth of focus by minimizing the spreading of the individual peaks within the axial range of interest. If we assume that the two peaks of the double-helix PSF are well confined with negligible side-lobes over the entire axial range of interest, the PSF can be approximated by

$$\mathbf{h}(z) \cong \mathbf{h}_0 * \delta^+(z) + \mathbf{h}_0 * \delta^-(z) , \quad (2.2)$$

where \mathbf{h}_0 represents the nominal, shift-invariant distribution of a single PSF peak. The Delta-distributions $\delta^\pm(z)$ can be expressed by

$$\delta_{kl}^\pm(z) = \delta [k \pm p(z) \cos(\theta(z)), l \pm p(z) \sin(\theta(z))] , \quad (2.3)$$

with a peak separation $p(z)$ and an azimuth orientation angle $\theta(z)$ that linearly depend on z . Accordingly, Eq. (5.1) can be rewritten as

$$\mathbf{i} = \int_{-\infty}^{+\infty} \underbrace{\mathbf{o}(z) * \mathbf{h}_0}_{\mathbf{o}_0(z)} * [\delta^+(p(z), \theta(z)) + \delta^-(p(z), \theta(z))] dz + \mathbf{n} \quad (2.4)$$

The image is thus a superposition of two representations of the blurred object distribution \mathbf{o}_0 , which are shifted according to their axial position. Note that \mathbf{o}_0 describes the blurred object distribution, analogue to a conventional imaging system with an extended depth of focus.

2.2.3. IMAGE PROCESSING

The work flow of the proposed image processing procedure, based on the previously described image acquisition approach, is schematically shown in Fig. 2.3. First, the depth map of the encoded image is retrieved as described in the following section. In the second step, the object distribution is reconstructed by applying the decoding approach explained in the subsequent section.

DEPTH MAP RETRIEVAL

The key to retrieving the depth distribution of the object from the raw image \mathbf{i} is to determine the lateral distribution of the rotation angle θ_{kl} of the twin images. This is done by analyzing the object features in a $M \times N$ pixels large neighborhood of each image location (k, l) , which is valid under the assumption that the neighborhood corresponds to a part of the object distribution located at the same distance z_{kl} . Thus, a sliding window function

$$w_{mn} = \begin{cases} 1 & \text{if } |m|, |n| \leq |M/2|, |N/2| \\ 0 & \text{else} \end{cases} \quad (2.5)$$

is applied to the raw image \mathbf{i} , which results in the subimage distribution \mathbf{I}_{kl} defined by

$$I_{kl}^{mn} = i_{k+m, l+n} \cdot w_{mn} . \quad (2.6)$$

In order to reduce the numerical effort of the depth map retrieval, the subimage distribution may be sampled at a reduced rate given by the window size divided by a sampling

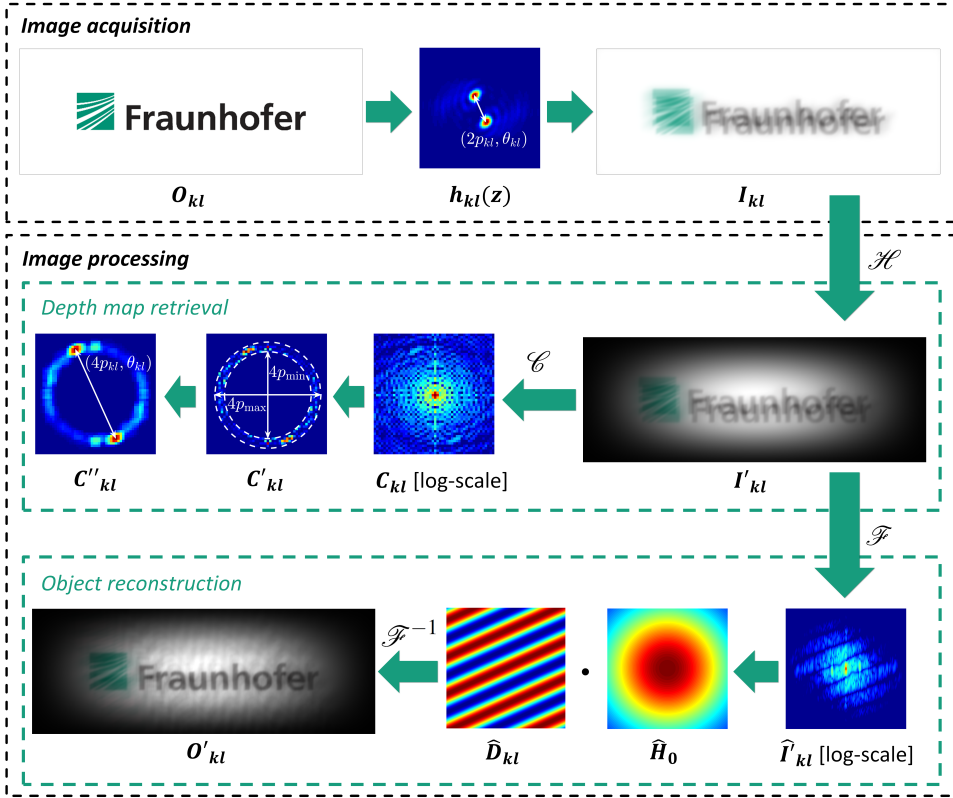


Figure 2.3: Schematic work flow of the proposed image acquisition and processing approach, which retrieves the depth information encoded in (p_{kl}, θ_{kl}) and reconstructs the object distribution O'_{kl} from a single subimage I_{kl} .

factor q , which is typically on the order of 2 to 4. According to Eq. (2.4), each windowed subimage distribution I_{kl} is given by the convolution

$$I_{kl} = O_{kl} * H_0 * [\delta^+(p_{kl}, \theta_{kl}) + \delta^-(p_{kl}, \theta_{kl})] + N_{kl} \quad , \quad (2.7)$$

where O_{kl} and N_{kl} denote the windowed subobject and noise distributions, respectively. The windowed nominal distribution of a single PSF peak is described by H_0 . In our approach, we apply the cepstrum concept to extract the corresponding, discretely sampled PSF parameters θ_{kl} and p_{kl} . The concept originates from pitch detection in human speech [24, 25] and can also be utilized to detect motion blur or stereo correspondence in imaging applications [26, 27], which in fact represent similar image processing problems. The power cepstrum distribution of I_{kl} is defined by

$$C_{kl} = \mathcal{C}\{I_{kl}\} := \mathcal{F}^{-1}\{\log(|\mathcal{F}\{I_{kl}\}|^2)\} \quad . \quad (2.8)$$

Accordingly, inserting Eq. (2.7) in Eq. (2.8) leads to

$$\mathbf{C}_{kl} = \mathcal{F}^{-1} \left\{ \log \left(\left| \mathcal{F} \{ \mathbf{I}_{0,kl} + \mathbf{N}_{kl} \} \right|^2 \right) \right\} \quad (2.9)$$

$$= \mathcal{F}^{-1} \left\{ \log \left(\left| \mathcal{F} \{ \mathbf{I}_{0,kl} \} \right|^2 \right) + \log \left(\left| 1 + \frac{\mathcal{F} \{ \mathbf{N}_{kl} \}}{\mathcal{F} \{ \mathbf{I}_{0,kl} \}} \right|^2 \right) \right\} \quad (2.10)$$

$$= \mathcal{C} \{ \mathbf{I}_{0,kl} \} + \mathcal{F}^{-1} \left\{ \log \left(\left| 1 + \frac{\mathcal{F} \{ \mathbf{N}_{kl} \}}{\mathcal{F} \{ \mathbf{I}_{0,kl} \}} \right|^2 \right) \right\}, \quad (2.11)$$

where $\mathbf{I}_{0,kl}$ denotes the subimage without noise. The obtained cepstrum is thus a superposition of the cepstrum of the encoded object distribution and a second contribution that depends on the spatial frequency content of the noise as well as the encoded object. The key property of the cepstrum calculation is that it maps a convolution into an addition. Thus, the first term in Eq. (2.11) can be written as

$$\mathcal{C} \{ \mathbf{I}_{0,kl} \} = \mathcal{C} \{ \mathbf{O}_{kl} * \mathbf{H}_0 \} + \mathcal{C} \{ \{ \delta^+ (p_{kl}, \theta_{kl}) + \delta^- (p_{kl}, \theta_{kl}) \} \}, \quad (2.12)$$

which separates the cepstrum of the blurred object distribution from the cepstrum of the shift term described by the delta distributions. According to [28], the latter leads to a symmetrical set of impulses within the cepstrum domain. The impulses are located along a line with a respective angle θ_{kl} and a separation $2p_{kl}$ and thus directly provide the engineered PSF parameters.

The main challenge of the proposed approach is to accurately identify these impulse peaks within each subimages cepstrum \mathbf{C}_{kl} . The first main limitation arises from the spatial frequency content of the object distribution. Fig. 2.2(b) shows the Modulation Transfer Function (MTF) of the proposed hybrid imaging system for two representative object distances z_1 and z_2 . It can be seen that the introduced phase element leads to a modulation of the conventional MTF shown in Fig. 2.2(c), which is characterized by a period p and an orientation θ . This modulation ultimately leads to the set of impulses within the cepstrum domain. Note that in comparison to performing an autocorrelation, the cepstrum analysis provides increased contrast of the impulse peak in case of a weak modulation. In fact, the separation between the source signal (blurred object distribution) and the carrier (double Delta-distribution) is improved due to the logarithmic enhancement of the modulation in the spatial frequency domain. However, the modulation turns invisible in case of a lack of sufficiently small spatial object features and the set of impulses in the cepstrum domain vanishes completely. Accordingly, the object's spatial frequency spectrum must span an area beyond the first modulation minimum at $1/(V \cdot p)$, considering the magnification V of the optical system. In other words, the object scene must contain spatial features that are comparable to or smaller than the double helix PSF extension $V \cdot p$ in object space. In addition, the peak identification can be ambiguous in case of periodic object features, which lead to an equivalent modulation of the image spectrum. The corresponding, additional peaks in the cepstrum domain may corrupt the peak identification and result in false depth information. The second major influence is given by the noise level. If the object's spatial frequency content in the range of interest is insufficient, peaks that originate from the noise contributions (second term in Eq. (2.11)) are dominating the cepstrum and the impulse identification becomes unreliable [27]. Accordingly, the window size needs to be increased at the expense of lateral

depth resolution in order to include more object features. It should be noted that both limitations are (in a slightly modified manner) inherent to all passive optical systems. In fact, the size of the considered neighborhood is crucial for a robust depth estimation of each object point. But making a reasoned choice for M and N is difficult because the noise in the cepstrum depends on the spatial frequency content in each window according to the second term in Eq. (2.11). The window size and the corresponding degree of noise averaging needed must then be set according to the particular object that is imaged.

In order to increase the reliability of the peak identification, a two-dimensional Hann window is initially applied to the individual subimages

$$I_{kl}^{\prime mn} = \mathcal{H}\{I_{kl}\} := I_{kl}^{mn} \cdot \left\{ \frac{1}{4} \left[1 - \cos\left(\frac{2\pi m}{M-1}\right) \right] \left[1 - \cos\left(\frac{2\pi n}{N-1}\right) \right] \right\}, \quad (2.13)$$

before the cepstrum calculation, in order to mitigate the influence of edge effects on the discrete Fourier transformation. In addition, a priori knowledge on the peak parameters θ and p is used. First, it is assumed that the axial extension of the object distribution is limited to a total PSF rotation range of 180 degree, which ensures a unique relationship between θ and z . Under this condition, the detection range of the impulses in the cepstrum domain can be truncated according to

$$C_{kl}^{\prime mn} = \begin{cases} C_{kl}^{mn} & \text{if } p_{\min} \leq \sqrt{m^2 + n^2}/2 \leq p_{\max} \\ 0 & \text{else} \end{cases}, \quad (2.14)$$

by applying a minimum and maximum double peak separation (p_{\min}, p_{\max}). Both should typically be in the order of 0.8 to 0.9 and 1.1 to 1.2 times the peak separation at the nominal (in-focus) object distance, respectively, which can be extracted from the optical system design. Second, the truncated cepstrum C_{kl}^{\prime} is convolved with a Gaussian kernel of size s to mitigate the impact of noise on the peak detection. The kernel width s should be selected in the range of 1-2 times the diffraction limited PSF peak size, which determines the minimum size of features in the cepstrum domain that do not originate from noise. In practice, s as well as (p_{\min}, p_{\max}) may be obtained by experimentally analyzing the PSF peak width σ and separation $p(z)$, respectively.

Finally, the pixel location (m_{\max}, n_{\max}) of the maximum in each convolved cepstrum $C_{kl}^{\prime\prime}$ is located and the cepstrum values in an s pixel wide neighborhood are extracted. The weighted position of the peak within this subset of $C_{kl}^{\prime\prime}$ can be calculated using a standard center of gravity detection algorithm and the rotation parameters θ_{kl} and p_{kl} are extracted for each subimage. In fact, the identification of a single peak in the cepstrum is sufficient, due to the symmetry of C_{kl} . The angle θ_{kl} is finally related to the object distance z_{kl} based on a look-up table of the calibrated relationship $z(\theta)$. We emphasize that the described peak identification approach focuses on a high computational efficiency. More advanced methods, e.g. based on maximum likelihood estimators, can provide a higher accuracy and robustness, but require computationally expensive iterative algorithms.

OBJECT RECONSTRUCTION

In order to reconstruct the original object information from a single acquisition, the twin images in \mathbf{i} need to be merged. This can be done by means of a deconvolution operation

using the double helix PSF. The shape of the PSF can, however, be distorted in comparison to the original design due to geometrical and chromatic aberrations, as well as mechanical system tolerances. A direct deconvolution may thus result in severe artifacts depending on these shape deviations. In general, it is possible to determine the exact PSF distribution experimentally. However, this may require measuring the two-dimensional PSF shape within the entire three-dimensional region of interest due to the lateral and axial dependency of potential PSF distortions, i.e. in case of significant off-axis aberrations. In addition to the extensive calibration efforts, either a comprehensive look-up table or complex interpolation schemes based on analytic or numerical approximations need to be incorporated. Alternatively, blind deconvolution algorithms can be applied that are however numerically demanding due to the necessity for iterative optimization procedures.

In order to facilitate a fast and reliable image decoding, the proposed object reconstruction focuses on removing the twin image within \mathbf{i} and partially recovering sharp object features. We retrieve the windowed subobject distributions \mathbf{O}'_{mn} with a linear Wiener-type (deconvolution) filter. The Fourier transform of Eq. (2.7) can be expressed as

$$\hat{\mathbf{I}}'_{kl} = \hat{\mathbf{O}}'_{kl} \cdot \hat{\mathbf{H}}_0 \cdot \hat{\mathbf{D}}_{kl} + \hat{\mathbf{N}}'_{kl} \quad (2.15)$$

where $\hat{\mathbf{I}}'_{kl}$ and $\hat{\mathbf{O}}'_{kl}$ denote the Fourier transformation of the Hann windowed distributions \mathbf{I}_{kl} and \mathbf{O}_{kl} , respectively. The Fourier transform $\hat{\mathbf{D}}_{kl}$ of the delta-distributions is

$$\hat{\mathbf{D}}_{kl}^{mn} = \cos [2\pi p_{kl} \{k \cos(\theta_{kl}) + l \sin(\theta_{kl})\}] , \quad (2.16)$$

which corresponds to the axially dependent MTF modulation illustrated in Fig. 2.2(b). The parameters θ_{kl} and p_{kl} are already obtained during the depth map retrieval. The Fourier transform $\hat{\mathbf{H}}_0$ of a single PSF peak with neglected side-lobes is approximated by a Gaussian function

$$\hat{H}_0^{mn} = \frac{1}{2\pi\hat{\sigma}^2} \exp\left(-\frac{m^2 + n^2}{2\hat{\sigma}^2}\right) , \quad (2.17)$$

with a width $\hat{\sigma}$. The sharpened object spectrum $\hat{\mathbf{O}}'_{kl}$ is reconstructed by a Wiener filter

$$\hat{\mathbf{O}}'_{kl} = \hat{\mathbf{I}}'_{kl} \cdot \left[\frac{\hat{\mathbf{H}}_0^* \cdot \hat{\mathbf{D}}_{kl}^*}{|\hat{\mathbf{H}}_0 \cdot \hat{\mathbf{D}}_{kl}|^2 + \mathbf{SNR}_{kl}^{-1}} \right] , \quad (2.18)$$

where \mathbf{SNR}_{kl} is the signal-to-noise ratio of each subwindow. In addition to limiting the amplification of noise, \mathbf{SNR}_{kl} is essential in order to compensate for zero values of $\hat{\mathbf{D}}_{kl}$ within the denominator of Eq. (2.18). On the one hand, $\hat{\mathbf{D}}_{kl}$ removes the modulation of the spectrum, which eliminates the twin image in \mathbf{i} . On the other hand, $\hat{\mathbf{H}}_0$ recovers high spatial frequency contributions. Therefore, a respective Gaussian width $\hat{\sigma} > \max\{N, M\}/(2\pi\sigma)$ should be selected according to the PSF peak width σ in order to avoid ringing artifacts. Note that a proper removal of the twin images necessitates accurate estimation of the local PSF parameters θ_{kl} and p_{kl} in the order of the pixel size of the image sensor. A false estimation, i.e. due to a high noise level or due to an oversized sliding window that spans over a significant depth range, can result in severe artifacts within the reconstructed object distribution. Contrarily, estimation errors based on lack

of small object features in certain object regions only lead to minor reconstruction artifacts due to the absence of high spatial frequencies. Finally, an inverse Fourier transformation of Eq. (2.18) leads to the recovered distribution \mathbf{O}'_{kl} . Adding these windowed subobjects according to

$$o_{kl} = \sum_{m,n} O'_{k-m,l-n}{}^{mn} \quad (2.19)$$

provides the reconstructed object distribution \mathbf{o} . The Hann window, which is maintained within each subobject, leads to a smooth overlap of the individual \mathbf{O}_{kl} , which mitigates stitching artifacts within \mathbf{o} even in case of a small sampling factor q . It should be pointed out that the object reconstruction significantly benefits from the extended depth of focus of the hybrid optical system. As can be seen in Fig. 2.2(b), the presented out-of-focus MTF is generally increased (i.e. for spatial frequencies $|\xi|, |\eta| > 0.1/(\lambda F\#)$) in comparison to the conventional MTF in Fig. 2.2(c). Hence, it enables an improved reconstruction of these frequencies, which results in an enhanced image resolution for object areas that are significantly out-of-focus. In addition, we emphasize that the Fourier transform $\mathcal{F}\{\mathbf{I}'_{kl}\} = \hat{\mathbf{I}}'_{kl}$, which is required to determine $\hat{\mathbf{O}}'_{kl}$ in Eq. (2.18), is already calculated during the prior cepstrum analysis. The total numerical effort for the depth estimation in combination with the object retrieval is thus mainly determined by only three Fourier transformations. Hence, it provides significantly reduced numerical costs in comparison to regularized iterative error minimization methods used in [13–15, 21]. It facilitates a fast approach that performs up to 1-2 fps for a megapixel image using our current software implementation in MATLAB on a conventional desktop PC. The frame rate can be increased furthermore by employing state-of-the-art hardware and using a dedicated computation on a GPU, which can potentially allow for a real time implementation on the order of 10-20 fps.

2.3. PROOF-OF-PRINCIPLE EXPERIMENT

2.3.1. SETUP IMPLEMENTATION

A demonstration system according to the proposed imaging setup shown in Fig. 2.1 is realized in order to verify the presented approach. For demonstration purposes, the developed photo resist master, which is obtained in the first step of the CGH fabrication process, is directly utilized without the subsequent transfer of the surface profile onto the final substrate. The surface profile of the corresponding element, which is measured using a white light interferometer, is shown in Fig. 2.4(a). Note that its lateral extension is slightly oversized with respect to the aperture stop diameter of 10 mm (indicated by a white circle in Fig. 2.4(a)) in order to accommodate alignment tolerances. The maximum profile height of 885 ± 10 nm complies with the maximum required phase shift of 2π , considering a design wavelength of 550 nm and the photo resist refractive index of 1.62. The major difference in comparison to the phase element manufacturing in [23] relies on the applied exposure scheme. In contrast to a single shot exposure, the element shown in Fig. 2.4(a) is manufactured by optimized lateral stitching of multiple substructure exposures in order to achieve a more than 4 times increased diameter of 12 mm. The advanced fabrication thus enables versatile lateral scaling of the designed CGHs in

order to match the apertures of commercially available objective lenses. Additional minor advantages include an improved surface smoothness with minimum imperfections, which results in reduced straylight, as well as an enhanced height discretization of 10bit in comparison to 30 levels in [23]. The phase element is placed at the aperture location of a compact optical demonstration setup, which consists of an achromatic doublet pair. In particular, we utilize two conventional achromats from Thorlabs with a focal length of 100 mm (AC254-250-A) and 250 mm (AC254-100-A), respectively. The diffraction limited optical system is optimized for a nominal object distance of 1 m and features a focal length of 83 mm and an F-number of 8.4. The correction of axial color aberrations is essential in order to minimize the spectral dependence of the rotation angle θ , which limits the axial resolution. However, it should be pointed out that a tailored spectral dependence can also provide an additional degree of freedom that can potentially increase the reliability of the depth measurement. A 1/2.3-inch CMOS image sensor (Aptina MT9F002) with a total pixel count of 4384×3290 (14MP) and a standard Bayer pattern for RGB imaging is placed at the nominal image position. The pixel size of $1.4 \mu\text{m} \times 1.4 \mu\text{m}$ with a Nyquist frequency of 357 lp/mm leads to a minor undersampling of the image considering the optical cut-off frequency of 216 lp/mm of the nominal system, but provides sufficiently high sampling of the engineered image distribution. The final system covers a lateral object field extension of $75 \times 53 \text{ mm}^2$ at the nominal distance.

2.3.2. DEPTH ESTIMATION

First, the relationship between the rotation angle θ and the object distance z is calibrated by successively imaging three LED point sources with peak irradiances at 465 nm, 540 nm and 625 nm, respectively. The noise is reduced by averaging over 10 image acquisitions. Note that the calibration can be limited to on-axis points due to the diffraction limited performance of the demonstration system over the entire three-dimensional field of interest. The corresponding PSF distribution, which is illustrated in the two insets of Fig. 2.4(b), clearly shows two distinct peaks (separated by approximately $20 \mu\text{m}$), which can be analyzed in order to obtain the axial dependence of $\theta(z)$ shown in Fig. 2.4(b). It can be seen that a linear relationship is maintained over a large range of approximately 170° . The effective depth range that can be utilized is 160 mm. Beyond this range, the rotation rate begins to decrease drastically and the distorted shape of the PSF prohibits reliable depth estimation. In comparison to conventional multi-aperture approaches that utilize multiple optical systems, no further calibration routines, such as the determination of the relative positions of the subsystems, need to be performed.

An extended, three-dimensional scene is imaged at the nominal object distance of 1 m using the calibrated system. The setup includes multiple objects located at different distances within the calibrated range between 960 mm and 1060 mm. The scene is illuminated by a conventional, broad-band halogen desk lamp without any spectral or polarization filtering. The left part of Fig. 2.5(a) shows the imaged nominal object scene, which is initially obtained without the CGH inside the optical system. The enlarged image sections on the right side of Fig. 2.5(a) exemplarily highlight two distinct object parts that are located at an in- and out-of-focus location. After the CGH is implemented into the system, the encoded image shown in Fig. 2.5(b) is obtained. As can be seen in the two enlarged image sections, the engineered PSF results in twin images of the captured

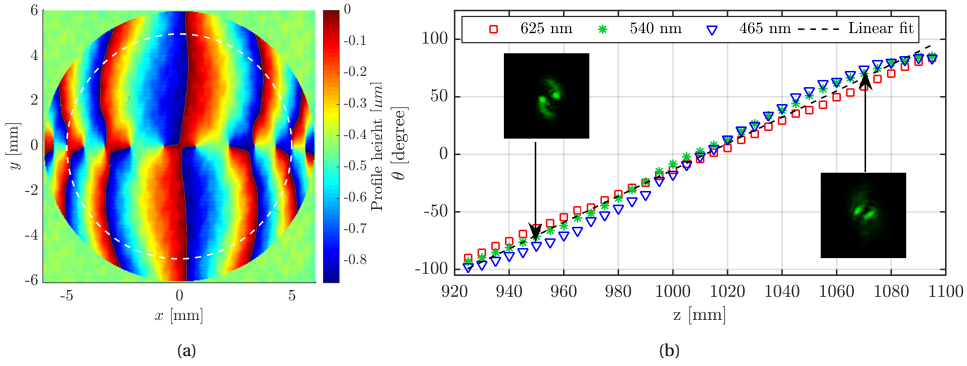


Figure 2.4: (a) Measured surface profile of realized CGH. The dashed circle indicates the aperture size of 10 mm within the optical setup. (b) Measured relationship between object distance z and rotation angle θ for three different wavelengths. The insets display the shape of the PSF at 540 nm for the corresponding object distance.

features, which are laterally shifted in a direction according to their axial position. The depth map of the object scene is obtained by applying the proposed cepstrum approach to the captured image. The sampling of the depth map is selected based on a compromise between maximizing the lateral resolution on the one hand and ensuring sufficient spatial object features to increase the signal to noise ratio for the peak identification in the cepstrum domain on the other hand. In particular, a windowing size of $M = N = 256$ and a sampling factor $q = 4$ are applied based on an empirical selection. After the determination of the angle distribution θ_{kl} and a subsequent evaluation of the corresponding distance z_{kl} using the linear calibration fit (Fig. 2.4(b)), the final depth map is calculated after applying a 3×3 pixel median filter [29] in order to reduce outliers. The resulting depth distribution shown in Fig. 2.6 covers the entire field of view over a depth range of approximately 100 mm. It clearly exhibits distinct objects of the captured scene and provides a spatially resolved visualization of their axial position.

2.3.3. IMAGE DECODING

Finally, the angle distribution θ_{kl} , obtained during the depth retrieval, is combined with the information on the peak separation p_{kl} to reconstruct the object distribution. The deconvolved image distribution, shown in Fig. 2.5(c), is obtained after applying the proposed filter function according to Eq. (2.18) using a width $\hat{\sigma} = 18$, which effectively avoids ringing artifacts. For demonstration purposes, a simplified, constant signal-to-noise ratio of 33 is applied for all subwindows, which provides a compromise between minimum noise amplification and an effective twin image removal. The image shows the uncoded RGB color information of the object and is only subject to minor reconstruction artifacts. A comparison between the decoded and the uncoded object distributions in Fig. 2.5 demonstrates the successful removal of the twin-image and an increased image contrast. A residual background, i.e. in the direction of the double-helix orientation, remains after the deconvolution due to the elongated side-lobes of the PSF, which are not accounted for in the approximated PSF in Eq. (2.2) and the corresponding filter in



(a) Nominal image



(b) Encoded image



(c) Decoded image

Figure 2.5: (a) Nominal image distribution of the three-dimensional object scene, captured without the CGH. The two insets on the right side exemplarily highlight an in- and out-of-focus part of the object scene, respectively. (b) Raw, encoded image distribution of the scene using the CGH. The in- and out-of-focus insets exhibit the blurred twin image with a lateral shift according to the distance of the respective object part. (c) Decoded image. The exemplary text features, displayed in both insets, can clearly be identified after the removal of the twin image.

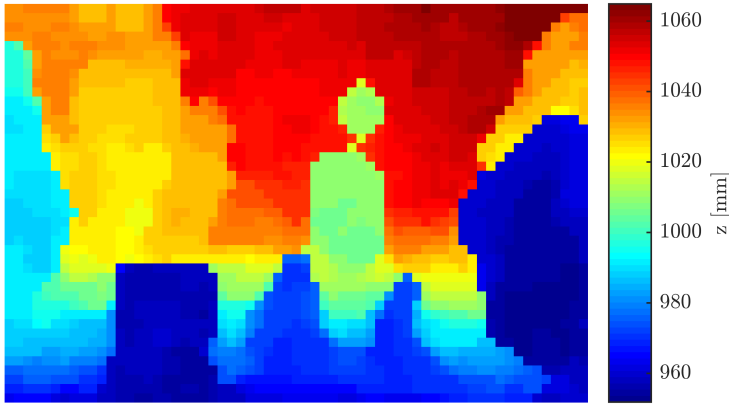


Figure 2.6: Retrieved depth map of the imaged, three-dimensional scene.

Eq. (2.18). These side lobes are a residue of the CGH design approach as well as fabrication tolerances, which can potentially be minimized further by optimizing the design, as well as the fabrication method. Alternatively, the experimental PSF can directly be used in the deconvolution approach, which necessitates a comprehensive three-dimensional characterization of the PSF distribution in order to minimize reconstruction artifacts. Furthermore, a comparison between the highlighted object parts of the nominal and the decoded image in Fig. 2.5 demonstrates the extended depth of focus property of the proposed hybrid system. Whereas the features of the out-of-focus part (highlighted in blue) of the nominal image are significantly blurred in comparison to the in-focus part (highlighted in red), the deconvolved image provides a comparable resolution throughout the entire axial range of interest. In fact, the out-of-focus part in Fig. 2.5(c) features an increased contrast in comparison to the same part in Fig. 2.5(a).

2.4. CONCLUSION

A system approach describing a passive optical setup combined with a tailored image processing concept is presented, which enables the acquisition of three-dimensional object information using a monocular camera system. The method is based on integrating a computer-generated hologram, fabricated on a thin glass substrate, into a conventional camera setup, which facilitates a compact, robust and cost efficient system with an extended depth of focus. Moreover, the optical setup does not require additional wavelength or polarization filters, which enables a light efficient image acquisition that maintains the RGB color information of the object. An efficient image processing approach has been developed that analyzes the cepstrum distribution of the image and incorporates a Wiener filter in order to provide a fast calculation of the axial and lateral object distribution based on a single image. Without the need for extensive iterative optimization procedures of common image deconvolution algorithms, the system potentially allows for three-dimensional video acquisition.

An experimental system has been implemented, demonstrating the capabilities of the

proposed system approach. The depth map as well as the lateral (RGB) information of an extended scene has been obtained based on a single acquisition using a compact, light efficient optical system with an engineered point spread function.

In addition to the qualitative demonstration presented here, future work will include a quantitative assessment of the systems imaging performance. In particular, we aim to address scaling laws of the axial and lateral resolution limits, which potentially allows for a system optimization according to a particular application and enables a proper comparison to other three-dimensional imaging approaches, i.e. based on stereo or plenoptic configurations.

ACKNOWLEDGMENTS

The authors would like to thank Marko Stumpf for manufacturing the CGH and Lucas van Vliet for a critical reading of the manuscript. This work was performed in the frame of the Photonics Research Germany funding program by the German Federal Ministry of Education and Research under contract 13N13667.

REFERENCES

- [1] R. Berlich, A. Bräuer, and S. Stallinga, *Single shot three-dimensional imaging using an engineered point spread function*, *Optics Express* **24**, 5946 (2016).
- [2] J. Salvi, J. Pagès, and J. Batlle, *Pattern codification strategies in structured light systems*, *Pattern Recognition* **37**, 827 (2004).
- [3] M.-C. Amann, T. Bosch, M. Lescure, R. Myllylä, and M. Rioux, *Laser ranging: a critical review of usual techniques for distance measurement*, *Optical Engineering* **40**, 10 (2001).
- [4] D. Huang, E. A. Swanson, C. P. Lin, J. S. Schuman, W. G. Stinson, W. Chang, M. R. Hee, T. Flotte, K. Gregory, and C. A. Puliafito, *Optical coherence tomography*, *Science* **254**, 1178 (1991).
- [5] M. Z. Brown, D. Burschka, and G. D. Hager, *Advances in computational stereo*, *IEEE Transactions on Pattern Analysis and Machine Intelligence* **25**, 993 (2003).
- [6] Y. Y. Schechner and N. Kiryati, *Depth from defocus vs. stereo: How different really are they?* *International Journal of Computer Vision* **39**, 141 (2000).
- [7] M. Subbarao and G. Surya, *Depth from defocus: A spatial domain approach*, *International Journal of Computer Vision* **13**, 271 (1994).
- [8] R. Horisaki and J. Tanida, *Multi-channel data acquisition using multiplexed imaging with spatial encoding*, *Optics express* **18**, 23041 (2010).
- [9] R. Horisaki and J. Tanida, *Preconditioning for multiplexed imaging with spatially coded psfs*, *Optics express* **19**, 12540 (2011).

- [10] T. Georgeiv, K. C. Zheng, B. Curless, D. Salesin, S. Nayar, and C. Intwala, *Spatio-angular resolution tradeoffs in integral photography*, Proceedings of the 17th Eurographics Conference on Rendering Techniques , 263 (2006).
- [11] A. Lumsdaine and T. Georgiev, *The focused plenoptic camera*, [Computational Photography \(ICCP\), 2009 IEEE International Conference on](#) , 1 (2009).
- [12] D. Miao, O. Cossairt, and S. K. Nayar, *Focal sweep videography with deformable optics*, [2013 IEEE International Conference on Computational Photography, ICCP 2013](#) , 1 (2013).
- [13] P. Llull, X. Yuan, L. Carin, and D. J. Brady, *Image translation for single-shot focal tomography*, [Optica](#) **2**, 822 (2015).
- [14] A. Levin, R. Fergus, F. Durand, and W. T. Freeman, *Image and depth from a conventional camera with a coded aperture*, [ACM Transactions on Graphics](#) **26**, 70 (2007).
- [15] A. Levin, S. W. Hasinoff, P. Green, F. Durand, and W. T. Freeman, *4d frequency analysis of computational cameras for depth of field extension*, [ACM Transactions on Graphics](#) **28**, 1 (2009).
- [16] S. R. P. Pavani and R. Piestun, *High-efficiency rotating point spread functions*, [Optics express](#) **16**, 3484 (2008).
- [17] A. Greengard, Y. Y. Schechner, and R. Piestun, *Depth from diffracted rotation*, [Optics Letters](#) **31**, 181 (2006).
- [18] S. Quirin, G. Grover, and R. Piestun, *Optimal 3d single-molecule super-resolution microscopy with engineered point spread functions*, in [Proceedings - International Symposium on Biomedical Imaging](#) (2012) pp. 926–927.
- [19] S. R. P. Pavani, A. Greengard, and R. Piestun, *Three-dimensional localization with nanometer accuracy using a detector-limited double-helix point spread function system*, [Applied Physics Letters](#) **95**, 021103 (2009).
- [20] S. Quirin and R. Piestun, *Depth estimation and image recovery using broadband, incoherent illumination with engineered point spread functions invited*, [Applied Optics](#) **52**, A367 (2013).
- [21] T. Niihara, R. Horisaki, M. Kiyono, K. Yanai, and J. Tanida, *Diffraction-limited depth-from-defocus imaging with a pixel-limited camera using pupil phase modulation and compressive sensing*, [Applied Physics Express](#) **8**, 012501 (2015).
- [22] H.-C. Eckstein, M. Stumpf, P. Schleicher, S. Kleinle, A. Matthes, U. D. Zeitner, and A. Brauer, *Direct write grayscale lithography for arbitrary shaped micro-optical surfaces*, in [The Twentieth Microoptics Conference](#), edited by M. Conference (IEEE, [Piscataway, NJ], 2015) pp. 1–2.
- [23] G. Grover, S. Quirin, C. Fiedler, and R. Piestun, *Photon efficient double-helix psf microscopy with application to 3d photo-activation localization imaging*, [Biomedical optics express](#) **2**, 3010 (2011).

- [24] A. M. Noll, *Short-time spectrum and “cepstrum” techniques for vocal-pitch detection*, *The Journal of the Acoustical Society of America* **36**, 296 (1964).
- [25] A. M. Noll, *Cepstrum pitch determination*, *The Journal of the Acoustical Society of America* **41**, 293 (1967).
- [26] M. Cannon, *Blind deconvolution of spatially invariant image blurs with phase*, *IEEE Transactions on Acoustics, Speech, and Signal Processing* **24**, 58 (1976).
- [27] P. W. Smith and N. Nandhakumar, *An improved power cepstrum based stereo correspondence method for textured scenes*, *IEEE Transactions on Pattern Analysis and Machine Intelligence* **18**, 338 (1996).
- [28] R. Rom, *On the cepstrum of two-dimensional functions (corresp.)*, *IEEE Transactions on Information Theory* **21**, 214 (1975).
- [29] W. K. Pratt, *Digital image processing* (John Wiley & sons, S.I., 1978).

3

FABRICATION OF COMPUTER GENERATED HOLOGRAMS USING FEMTOSECOND LASER DIRECT WRITING

We demonstrate a single-step fabrication method for Computer Generated Holograms (CGHs) based on Femtosecond Laser Direct Writing (FLDW). Therefore, a tightly arranged, longitudinal waveguide array is directly inscribed into a transparent material. By tailoring the individual waveguide length, the phase profile of an incident laser beam can be adapted arbitrarily. The approach is verified in common borosilicate glass by inscribing a designed phase hologram which forms the desired intensity pattern in its far field. The resulting performance is analysed and the potential as well as limitations of the method are discussed.

Parts of this chapter have been published as R. Berlich, D. Richter, M. Richardson, and S. Nolte, *Optics Letters* **41**, 1752–1755 (2016). [1].

3.1. INTRODUCTION

Computer generated holograms (CGHs) are utilized in a wide range of applications such as beam shaping and steering as well as testing of aspherical, refractive optical components [2–5]. Their main advantages rely on their compactness and simple optical alignment compared to refractive elements. They can provide an extensive depth of sharpness in addition to a high efficiency. However, the manufacturing process is typically rather complex, since conventional fabrication techniques using UV or e-Beam radiation are based on mask or scanning lithography [6–8]. Although these methods are already well established in commercial applications, they still require a sequence of sample preparation and processing steps. The processing time as well as the high complexity of the fabrication consequently constitute severe constraints. Furthermore, the produced CGHs are limited to surface structures and are thus less resistant to external mechanical influences. In this letter we present how Femtosecond Laser Direct Writing (FLDW) can be employed to fabricate CGHs in a single step, directly inside the bulk substrate.

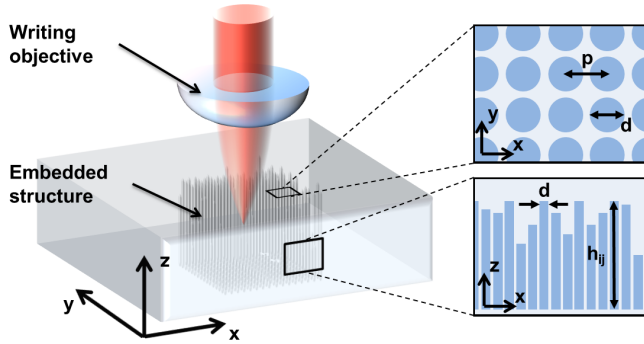


Figure 3.1: FLDW fabrication of embedded CGH structure comprising an array of longitudinal waveguides with distinct height profile h_{ij} .

3.2. THEORETICAL CGH MODELING

In order to discuss this approach, let us first consider the theoretical modeling of the CGH. The interaction of an incident field $u_{in}(x, y, z)$ of wavelength λ and a CGH is commonly described using the Thin Element Approximation (TEA) at a reference distance z_0 . Within this approximation, which is initially considered for the design of the CGH here, diffraction effects are neglected during the light propagation through the structure [9]. The resulting field $u_{out}(x, y, z_0)$ in the element plane is consequently obtained by a multiplication of the incoming field $u_{in}(x, y, z)$ with the transfer function $t(x, y)$ of the hologram

$$\begin{aligned} u_{out}(x, y, z_0) &= u_{in}(x, y, z_0) \cdot t(x, y) \\ &= u_{in}(x, y, z_0) \cdot A(x, y) e^{i\Delta\phi(x, y)} \end{aligned} \quad (3.1)$$

where $A(x, y)$ and $\Delta\phi(x, y)$ denote the corresponding amplitude and phase change, respectively. The CGH fabrication approach described in this letter is based on a phase change $\Delta\phi(x, y)$ that is introduced onto the incident field after the propagation through an extended three-dimensional refractive index modification profile $\Delta n(x, y, z)$. This modification, which is directly embedded inside the CGH substrate, is realized using FLDW [10, 11]. By adjusting the corresponding writing parameters, the absorption coefficient of these structures can be minimized and the respective amplitude change $A(x, y)$ can be considered negligible. In contrast to techniques that employ femtosecond laser-induced microexplosion [12, 13] to generate absorbing CGH structures, the phase only elements, proposed here, enable significantly improved diffraction efficiency. Under the assumption of TEA, the introduced phase change is determined by

$$\Delta\phi(x, y) = \frac{2\pi}{\lambda} \int_0^{h_{\max}} \Delta n(x, y, z) dz, \quad (3.2)$$

where h_{\max} denotes the maximum depth of the FLDW induced index modification. In our approach, the inscribed structure $\Delta n(x, y, z)$ is created by writing an array of $N \times N$ longitudinal waveguides, separated by a lateral pitch p as illustrated in Fig. 3.1. Each individual waveguide (i, j) ($i, j = 1, \dots, N$) comprises a specified axial height h_{ij} . A proper choice of the substrate material and optimized writing parameters ensure very smooth and crack-free FLDW structures [14, 15], so that the waveguides can be approximated by ideal cylinders of diameter d and height h_{ij} with a constant refractive index change Δn_{eff} . Accordingly, the inscribed structure can be modeled as

$$\Delta n(x, y, z) = \sum_{i,j} [\Delta n_{\text{eff}} \cdot \text{circ}(x - ip, y - jp) \cdot \text{rect}_{ij}(z)], \quad (3.3)$$

where

$$\text{circ}(x, y) = \begin{cases} 1 & \text{for } x^2 + y^2 \leq (d/2)^2 \\ 0 & \text{else} \end{cases} \quad (3.4)$$

and

$$\text{rect}_{ij}(x, y) = \begin{cases} 1 & \text{for } 0 \leq z \leq h_{ij} \\ 0 & \text{else} \end{cases} \quad (3.5)$$

By inserting Eq.(3.3) into Eq.(3.2), the phase change introduced by the waveguide assembly is determined by

$$\Delta\phi(x, y) = \sum_{i,j} \underbrace{\frac{2\pi}{\lambda} \cdot \Delta n_{\text{eff}} \cdot h_{ij}}_{\Delta\phi_{ij}} \cdot \text{circ}(x - ip, y - jp). \quad (3.6)$$

Thus, an arbitrary computer generated phase profile $\Delta\phi_{ij}$ can be generated for a given wavelength by adapting the profile height h_{ij} . Note that $\text{circ}(x, y)$ in Eq.(3.6) defines the fill factor of the FLDW structure, which directly affects the diffraction efficiency of the CGH [16].

3.3. CGH DESIGN AND FABRICATION

In order to verify the feasibility of the proposed fabrication approach, a first CGH is manufactured to generate the far field intensity pattern illustrated in Fig. 3.2(a). The sample image (IOF logo) only covers the upper half of the total 128x128 pixel target area. This enables the separation and evaluation of the zero diffraction order during the experimental analysis in order to determine the overall diffraction efficiency. The required phase distribution $\Delta\phi_{ij}$ shown in Fig. 3.2(b) is designed by employing an Iterative Fourier Transform Algorithm (IFTA) [17].

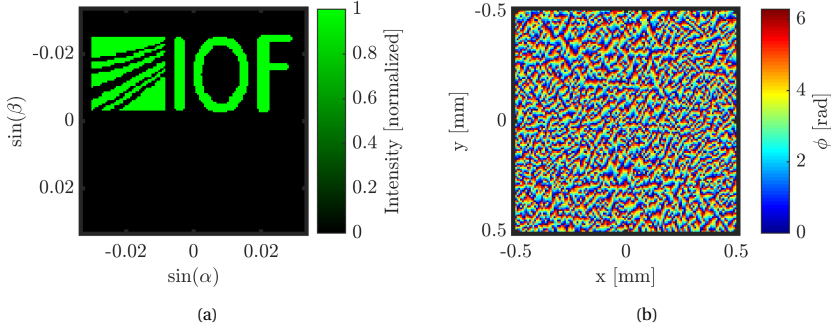


Figure 3.2: (a) Targeted far field intensity distribution of CGH element. (b) Corresponding phase profile in (x, y) element plane. The diffraction angles in (a) are denoted by α and β , respectively, assuming a lateral phase sampling pitch of $p = 8\mu\text{m}$ and a wavelength of 532nm.

An amplified Ti:Sapphire laser system (Coherent RegA), working at a center wavelength of 800nm is incorporated for the fabrication of the designed CGH. The repetition rate is fixed to 100kHz and the pulse duration is set to 150fs. The laser is tightly focused into borosilicate glass (Corning Eagle 2000) without special sample preparation necessary. Utilizing a 20x objective with a numerical aperture of 0.35 provides a practical compromise between small waveguide diameters of approximately $6\mu\text{m}$ and a sufficient working distance. A computer controlled three axes positioning system (Aerotech ALS 130) furthermore enables precise and fast positioning. The translation speed is set to a maximum of 100mm/s in the axial direction in order to facilitate a fast fabrication of the large amount of waveguides. The writing direction is set from the bottom to the top in order to avoid that the modified region within a single waveguide influences the incident laser beam. The writing power is eventually optimized to result in a maximum refractive index contrast while ensuring smooth, crack-free features at the same time. In this respect, the practical method presented in [18] is incorporated to measure the absolute refractive index modification and an optimized value of $\Delta n_{\text{eff}} = 7 \cdot 10^{-4}$ is obtained for an average power of 60mW.

The required axial writing distance Δz_{ij} of each waveguide (i, j) can be calculated by inserting the determined amount of Δn_{eff} into Eq.(3.6) and accounting for the effective focus depth due to the linear refractive index n_0 of the borosilicate glass

$$\Delta z_{ij} = \frac{h_{ij}}{n_0} = \frac{\lambda \cdot \Delta\phi_{ij}}{2\pi \cdot \Delta n_{\text{eff}} \cdot n_0}. \quad (3.7)$$

In fact, an additional offset is introduced for each waveguide due to the elongated extension of an individual FLDW spot in the order of $40\mu\text{m}$. It does however not effect the far field image according to Eq.(3.1) since it corresponds to a constant additional phase term in u_{out} . It should be emphasized that there is no discretization of the profile phase $\Delta\phi_{ij}$ which would lead to a decrease in efficiency [16, 19]. In comparison to common lithographic techniques, the FLDW method is capable of a nearly continuous phase implementation.

The design wavelength λ is set to 532nm which leads to a maximum modification length of $700\mu\text{m}$ considering a maximum phase change of 2π . The CGH is placed $150\mu\text{m}$ above the bottom of the 1mm thick borosilicate glass samples to center the structure. Although a constant spot size is assumed within the writing process, it has to be noted that the large longitudinal extension of the waveguides can lead to an inhomogeneous implementation in different depths of the glass. Thus, the diameter and the amount of Δn_{eff} can vary with the depth due to aberrations occurring from the glass surface. This effect is neglected but improvements can be achieved using adaptive optics in combination with the translation stage [20].

A minimum spacing of $8\mu\text{m}$ between the individual waveguides is selected to prevent an overlap of adjacent modifications which would lead to an unpredictable change of the induced refractive index profile. Contrarily, larger separations would severely decrease the diffraction efficiency [16]. The ratio κ between the diameter of the incident illumination laser and the 1.024mm width ($128\text{ pixel} \times 8\mu\text{m}$) of the single CGH constitutes another crucial factor for the CGH implementation. A small ratio leads to a significant overlap of adjacent image pixels and the resulting interaction decreases the signal to noise ratio (SNR) of the image. As demonstrated in [21], it can be avoided effectively by adjusting the illumination beam diameter for values of $\kappa > 2.6$. However, the small extension of the single CGH compared to the incident laser beam would result in a large intensity of the zeroth diffraction order, since a significant part would not be diffracted by the CGH. The waveguide profile h_{ij} is thus replicated by a lateral factor of three in order to overcome this effect. The respective overall amount of 384×384 waveguides results in a total lateral size of $3.072 \times 3.072\text{mm}^2$ of the 3×3 CGH pattern. The corresponding fabrication time of 28 hours remains a major drawback but it is inherent for point-wise fabrication methods. A reduction could be achieved by further maximizing the induced amount of refractive index change, e.g. by selecting a different substrate glass material or by incorporating higher repetition rate laser systems [22]. Eventually, parallelizing the fabrication process by generating a pattern of multiple writing beams, e.g. using diffractive optical elements or spatial light modulators [23, 24], constitutes a promising approach to mitigate the severe time constraint. Figure 3.3 shows microscope images of the fabricated CGH at two cross sections in the (x, y) -plane. Whereas the bottom of the CGH in Fig. 3.3(a) comprises the full waveguide array, only a fraction of the entire assembly extends up to the exemplary height of $300\mu\text{m}$ presented in Fig. 3.3(b). Hence, a refractive index pattern based on axially extended waveguides, which tailor the phase profile of an incident laser beam, is facilitated. The magnified insets also confirm the prevention of a waveguide overlap.

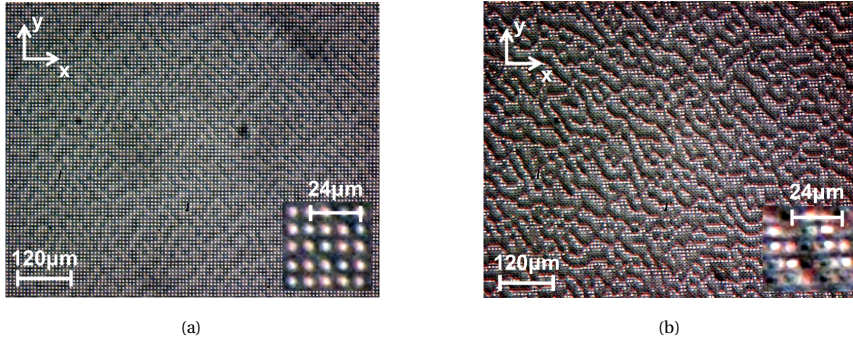


Figure 3.3: Microscope images displaying two cross sections ((x, y) -plane) of fabricated CGH at a respective height of (a) $0\mu\text{m}$ and (b) $300\mu\text{m}$.

3.4. EXPERIMENTAL PERFORMANCE VALIDATION

The sample is finally illuminated under normal incidence with a Nd:YAG laser at 532nm to investigate the performance of the fabricated CGH. The diameter of the beam with a top hat profile is adapted to 3mm using a standard telescope setup in order to fit the size of the CGH and to fulfill the condition $\kappa > 2.6$. The transmitted beam is subsequently focused ($f=50\text{mm}$) to project the far field intensity pattern onto a CCD camera as illustrated in Fig. 3.4(a). Fig. 3.4(b) demonstrates that the resulting irradiance distribution complies qualitatively with the aimed pattern of Fig. 3.2(a). The approach to fabricate CGHs using FLDW is thus verified. However, the image quality is still subject to different kinds of degradation. In addition to a relatively inhomogeneous background noise of the intensity distribution, Fig. 3.4(b) shows a strong zeroth diffraction order. The total diffraction efficiency η of the CGH is approximately 37% . Moreover, Fig. 3.4(b) reveals a weak mirrored image of the actual logo with 7% of the overall power.

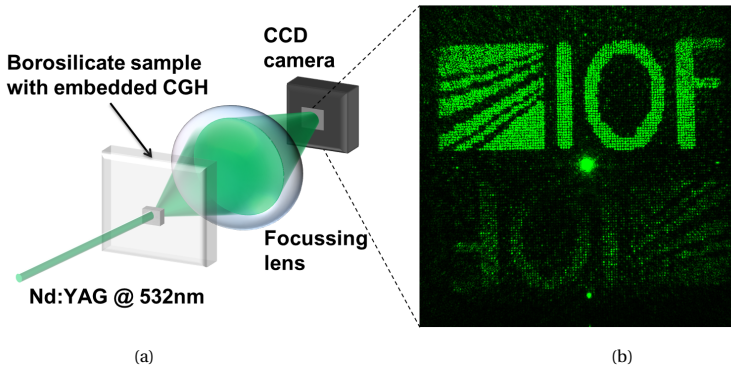


Figure 3.4: (a) CGH performance characterization under 532nm laser illumination and subsequent imaging of the resulting diffraction pattern onto a CCD detector. (b) Captured irradiance distribution of fabricated CGH.

In order to assess the origin of the image degradation, the CGH performance is sim-

ulated numerically. In particular, the light propagation through the FLDW structure is modeled using a fast Fourier transform beam propagation method (FFT-BPM). The resulting scalar field distribution u_{out} behind the CGH is shown in Fig. 3.5. It can be seen that the inscribed element significantly alters the amplitude distribution of u_{in} in addition to the desired phase change ϕ . Due to the long extension of the axial waveguide structure, light is coupled into the longitudinal waveguides from the space between and subsequently guided during the propagation. Consequently, the performance of the inscribed phase element cannot accurately be described using TEA despite the weak modification of the refractive index and the large feature sizes compared to the wavelength. The theoretical irradiance distribution on the CCD camera is calculated by a Fourier transformation of u_{out} (Fraunhofer approximation). As illustrated in Fig. 3.6(a), it complies with the image obtained experimentally and provides comparable diffraction efficiencies of 41% and 7% for the nominal and the mirrored image, respectively.

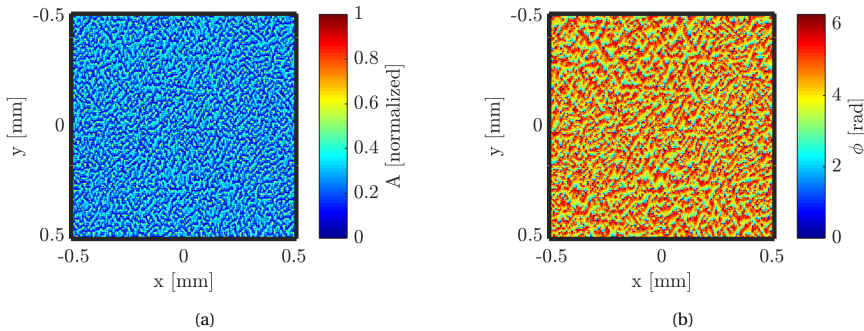


Figure 3.5: Theoretical amplitude (a) and phase (b) distribution of the scalar field u_{out} behind the CGH based on a FFT-BPM simulation.

The main reason for the limited diffraction efficiency η originates from the low waveguide fill factor of approximately 44%. Figure 3.6(b) illustrates the theoretical dependency of η on the waveguide spacing p considering a constant waveguide diameter of $6\mu\text{m}$. Note that the diameter of the incident illumination laser beam is scaled in order to maintain a constant value of κ . A maximum of 45% can be obtained by the proposed fabrication scheme in case p coincides with the waveguide diameter d , which corresponds to a fill factor of 79%. For comparison, Fig. 3.6(b) provides the corresponding diffraction efficiency in case of an equivalent thin phase element (e.g. realized by a spatial light modulator with a limited fill factor) under the assumption of TEA. It can be seen that the respective values of η are significantly reduced for $p > d$. Hence, the performance of the FLDW CGH clearly benefits from the amplitude alteration due to the light guiding effect of the inscribed waveguides. In fact, this unique feature of the thick CGH structure partially compensates for the low fill factor that needs to be applied in order to prevent overlap of adjacent waveguides. Contrarily, it should be noted that the mirror image obtained, which also originates from the changed amplitude profile, represents a minor drawback.

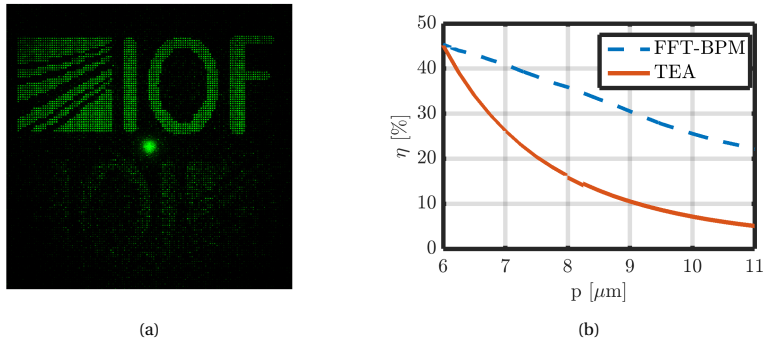


Figure 3.6: (a) Theoretical CCD (far field) image of the fabricated CGH based on an FFT-BPM simulation. (b) Simulated dependency of the diffraction efficiency η on the waveguide period p , considering a thin (TEA) and a thick (FFT-BPM) CGH modeling. The corresponding waveguide diameter d is $6\mu\text{m}$.

3.5. CONCLUSION

In conclusion, it was demonstrated how FLDW can be applied to create computer generated holograms in a single writing process. Hence, fabrication costs and effort can potentially be decreased. The elements are moreover buried inside the substrate, improving their resistance against external influences. The possibility to implement arbitrary phase profiles without a discretization furthermore promises high diffraction efficiencies. First experimental results to validate the feasibility of the approach were obtained for a CGH fabricated inside borosilicate glass. The achieved intensity distribution in the far field complied with the design and performed a moderate diffraction efficiency of 37%. While the thin element approximation could successfully be applied to design the CGH, we demonstrated that it does not accurately describe the final performance of the FLDW element. In fact, the elongated extension of the CGH structure leads to a significantly improved diffraction efficiency compared to an equivalent thin element. The fabrication time is currently rather long, which limits the capabilities of the CGHs in terms of resolution and quality. Strategies for improving the CGH fabrication as well as the performance were however pointed out and will be addressed in future work. It is finally noted that the presented approach can be extended to create multiple layers of FLDW elements within a single sample. Accordingly, CGHs with multiplexing capabilities, as presented in [21], could be fabricated in a single substrate.

This work was performed as part of the Atlantis MILMI program, funded jointly by the U.S. Department of Education and the European Commission, and was funded in part by the National Science Foundation and the State of Florida as well as by the Thuringian Ministry of Education, Science and Culture under contract B514-10061 (OptiMi 2020).

REFERENCES

- [1] R. Berlich, D. Richter, M. Richardson, and S. Nolte, *Fabrication of computer-generated holograms using femtosecond laser direct writing*, *Optics Letters* **41**, 1752 (2016).

- [2] K. Dholakia and T. Čižmár, *Shaping the future of manipulation*, *Nat. Photon.* **5**, 335 (2011).
- [3] F. Burmeister, U. D. Zeitner, S. Nolte, and A. Tünnermann, *High numerical aperture hybrid optics for two-photon polymerization*, *Optics Express* **20**, 7994 (2012).
- [4] A. J. MacGovern and J. C. Wyant, *Computer generated holograms for testing optical elements*, *Applied Optics* **10**, 619 (1971).
- [5] M. Beier, D. Stumpf, U. D. Zeitner, A. Gebhardt, J. Hartung, S. Risse, R. Eberhardt, H. Gross, and A. Tünnermann, *Measuring position and figure deviation of freeform mirrors with computer generated holograms*, in *Imaging and Applied Optics* (2015) p. FT3B.2.
- [6] L. Yang, A. El-Tamer, U. Hinze, J. Li, Y. Hu, W. Huang, J. Chu, and B. N. Chichkov, *Parallel direct laser writing of micro-optical and photonic structures using spatial light modulator*, *Optics and Lasers in Engineering* **70**, 26 (2015).
- [7] Y. Bourgin, T. Siefke, T. Käsebier, P. Genevée, A. Szeghalmi, E.-B. Kley, and U. D. Zeitner, *Double-sided structured mask for sub-micron resolution proximity i-line mask-aligner lithography*, *Optics Express* **23**, 16628 (2015).
- [8] W. Freese, T. Kämpfe, W. Rockstroh, E.-B. Kley, and A. Tünnermann, *Optimized electron beam writing strategy for fabricating computer-generated holograms based on an effective medium approach*, *Optics express* **19**, 8684 (2011).
- [9] J. W. Goodman, *Introduction to Fourier optics*, fourth edition ed., Vol. 15 (W.H. Freeman Macmillan Learning, New York, 2017).
- [10] K. M. Davis, K. Miura, N. Sugimoto, and K. Hirao, *Writing waveguides in glass with a femtosecond laser*, *Optics Letters* **21**, 1729 (1996).
- [11] R. R. Gattass and E. Mazur, *Femtosecond laser micromachining in transparent materials*, *Nat. Photon.* **2**, 219 (2008).
- [12] Y. Li, K. Yamada, T. Ishizuka, W. Watanabe, K. Itoh, and Z. Zhou, *Single femtosecond pulse holography using polymethyl methacrylate*, *Optics express* **10**, 1173 (2002).
- [13] Z. Guo, S. Qu, and S. Liu, *Generating optical vortex with computer-generated hologram fabricated inside glass by femtosecond laser pulses*, *Optics Communications* **273**, 286 (2007).
- [14] S. Nolte, M. Will, J. Burghoff, and A. Tünnermann, *Ultrafast laser processing: new options for three-dimensional photonic structures*, *Journal of Modern Optics* **51**, 2533 (2004).
- [15] S. M. Eaton, H. Zhang, M. L. Ng, J. Li, W.-J. Chen, S. Ho, and P. R. Herman, *Transition from thermal diffusion to heat accumulation in high repetition rate femtosecond laser writing of buried optical waveguides*, *Optics Express* **16**, 9443 (2008).

- [16] D. Palima and V. R. Daria, *Effect of spurious diffraction orders in arbitrary multifoci patterns produced via phase-only holograms*, *Applied Optics* **45**, 6689 (2006).
- [17] W. Gerchberg and W. O. Saxton, *A practical algorithm for the determination of phase from image and diffraction plane pictures*, *Optik* **35**, 237 (1972).
- [18] R. Berlich, J. Choi, C. Mazuir, W. V. Schoenfeld, S. Nolte, and M. Richardson, *Spatially resolved measurement of femtosecond laser induced refractive index changes in transparent materials*, *Optics Letters* **37**, 3003 (2012).
- [19] W. Freese, T. Kämpfe, E.-B. Kley, and A. Tünnermann, *Design of binary sub-wavelength multiphase level computer generated holograms*, *Optics Letters* **35**, 676 (2010).
- [20] N. Huot, R. Stoian, A. Mermillod-Blondin, C. Mauclair, and E. Audouard, *Analysis of the effects of spherical aberration on ultrafast laser-induced refractive index variation in glass*, *Optics express* **15**, 12395 (2007).
- [21] T. Kämpfe, E.-B. Kley, and A. Tünnermann, *Designing multiplane computer-generated holograms with consideration of the pixel shape and the illumination wave*, *Journal of the Optical Society of America A* **25**, 1609 (2008).
- [22] S. M. Eaton, M. L. Ng, R. Osellame, and P. R. Herman, *High refractive index contrast in fused silica waveguides by tightly focused, high-repetition rate femtosecond laser*, in *Journal of Non-Crystalline Solids*, Vol. 357 (2011) pp. 2387–2391.
- [23] M. Pospiech, M. Emons, A. Steinmann, G. Palmer, R. Osellame, N. Bellini, G. Cerullo, and U. Morgner, *Double waveguide couplers produced by simultaneous femtosecond writing*, *Optics express* **17**, 3555 (2009).
- [24] M. Sakakura, T. Sawano, Y. Shimotsuma, K. Miura, and K. Hirao, *Fabrication of three-dimensional 1 x 4 splitter waveguides inside a glass substrate with spatially phase modulated laser beam*, *Optics express* **18**, 12136 (2010).

4

HIGH-ORDER-HELIX POINT SPREAD FUNCTIONS FOR MONOCULAR THREE-DIMENSIONAL IMAGING WITH SUPERIOR ABERRATION ROBUSTNESS

An approach for designing purely refractive optical elements that generate engineered, multi-order-helix point spread functions (PSFs) with large peak separation for passive, optical depth measurement is presented. The influence of aberrations on the PSF's rotation angle, which limits the depth retrieval accuracy, is studied numerically and analytically. It appears that only Zernike modes with an azimuthal index that is an integer multiple of the number of PSF peaks introduce PSF rotation, and hence a depth estimation error. This implies that high-order-helix designs have superior robustness with respect to aberrations. This is experimentally demonstrated by imaging an extended scene in the presence of severe system aberrations using novel, cost-efficient phase elements based on UV-replication on wafer-scale.

Parts of this chapter have been published as R. Berlich, and S. Stallinga, Opt. Express **26**, 4873-4891 (2018) [1].

4.1. INTRODUCTION

The depth dependence of the Point Spread Function (PSF) of an imaging system can be customized by engineering the pupil phase with a Computer Generated Hologram (CGH). This approach has been widely studied with the goal to extend the depth of focus of conventional imaging systems [2–4]. In addition, it has gained interest for monocular, three-dimensional imaging [5]. Phase element designs have been proposed that generate two separated PSF peaks with a defocus dependent, double-helix shaped rotation [6, 7]. If the relationship between the rotation angle α and the distance of an object point z is known, a measurement of α enables retrieving the axial location of an object point in addition to its lateral location. So far, this method has mainly been applied for three-dimensional particle localization and tracking [8–14]. Further studies have demonstrated that the entire depth map of an extended, three-dimensional scene can be obtained for a broadband illumination [15, 16].

Previous studies have commonly considered idealized optical systems with an imaging performance close to the diffraction limit. The imaging performance of state-of-the-art optical systems in application fields such as machine vision, automotive or consumer electronics is, however, commonly far away from the diffraction limit. It is therefore essential to investigate how susceptible helical PSFs are to aberrations and how the rotation of the engineered PSF and ultimately the depth retrieval may be corrupted. In fact, the required calibration of the relationship between the rotation angle α and the object distance z only partially accounts for aberration introduced rotation. The calibration step is commonly performed close to the optical axis, which does not allow for compensating for the effect of off-axis system aberrations such as astigmatism. A calibration of the entire field of view of the pupil engineered system would be necessary in order to eliminate respective rotation angle uncertainties. Moreover, this characterization would have to be performed for each nominal object distance setting, which requires an immense calibration effort. In addition, aberration conditions may vary for different application scenarios, e.g. due to thermally induced effects or imaging through thick media. Thus, the question arises if the influence could be mitigated by altering the design of the rotating PSF.

The particular influence of primary spherical aberration, as well as coma and astigmatism has been investigated in the literature for the specific case of double-helix PSFs [17–19]. In this paper, we study the robustness for aberrations of helical PSFs in a generalized framework in which we consider designs with N peaks ($N = 2, 3, 4, \dots$). The aim of this analysis is to provide the necessary foundation for balancing the impact of different aberrations on the rotation of the PSF in order to develop high accuracy, pupil engineered optical systems for 3D image acquisition. Furthermore, we demonstrate how high-order-helix designs that feature more than two PSF peaks provide improved robustness regarding the rotation of the PSF with defocus. The respective designs thus allow for less stringent requirements on the optical system, e.g. with respect to the residual wave front error, which reduces system complexity and costs. Especially astigmatism is of considerable importance, as it scales quadratically with the field coordinates, and therefore usually dominates over other aberrations that scale with higher powers of the field coordinates.

Initially, we present a new design method for higher order helical PSFs and evaluate its

performance in section 2. In section 3, we analyze the sensitivity of the PSF rotation to different aberrations using numerical and theoretical means. Experimental results are presented in section 4 and the main results of the paper are concluded in section 5.

4.2. MULTI-ORDER-HELIX DESIGNS

4.2.1. DESIGN APPROACH

A design approach to generate PSF distributions that provide a depth dependent rotation was initially introduced based on a set Bessel beams [20]. Subsequently, these designs were described using a composition of Gauss-Laguerre (GL) modes [21] and extended towards phase only elements [6, 22]. An alternative design method using a set of Fresnel zones to generate rotating, single-helix PSFs ($N = 1$) was described by Prasad in ref. [7] and extended for double-helix shapes by Roider et al. in ref. [12]. These two design approaches provide a basis for customized double-helix CGH designs that are, however, limited in different ways. On the one hand, we find that the GL mode based designs provide limited capability to generate largely separated PSF peaks with an extended rotation range. In particular, the iterative optimization results in undesired side lobes that limit the depth retrieval accuracy as well as the image quality. On the other hand, the Fresnel zone designs do not allow for direct optimization of the PSF peak confinement over a specific axial range of interest. Moreover, both methods lead to very complex CGH designs with a significant number of phase discontinuities and dislocations that degrade the PSF shape when imaging using a broad wavelength spectrum.

Here, we propose a novel phase element design routine to overcome these limitations and moreover to allow for generating generalized N th order helix PSFs. To this end, we initially generalize the Fresnel zone design approach [7, 12] by exploiting three main design parameters. The number of zones that lie within the phase element radius R is defined by the design parameter L . Each of the $l = 1, \dots, L$ zones is bounded by circles of radius R_{l-1} and R_l , where $R_l = R(l/L)^\epsilon$. The second design parameter ϵ can be used to tailor the trade-off between the helix peak confinement and the shape invariance during rotation. The phase of the l th ring of the CGH is given by

$$\Phi_l(\phi) = [(l-1)N+1]\phi \quad (4.1)$$

where ϕ is the azimuthal coordinate. Here, we consider a third design parameter N in the phase definition, which represents a generalization of existing designs [7, 12]. It directly defines the peak number of the generalized multi-order-helix PSF. Note that for $N = 1$, Eq. (4.1) reduces to the original single-helix phase element design proposed in [7]. In general, the peak separation, the rotation rate as well as the total depth range of the corresponding, engineered PSF are jointly influenced by the three design parameters $[N, L, \epsilon]$. On the one hand, the maximum depth range is limited by ambiguities in case of a rotation beyond $[-\pi/N, \pi/N]$ since the depth retrieval is based on relating the rotation angle α to the object distance z . Consequently, a high number of peaks also reduces the available depth range. On the other hand, the PSF rotates at a rate $1/(N \cdot L)$ rad per unit defocus change for the particular case of $\epsilon = 0.5$, according to the analytical PSF approximation given in [7]. Hence, the respective maximum, unambiguous defocus range equals $2\pi L$, which is independent of the peak number N . This range can be related to the

maximum available depth range Δz_{\max} of the pupil engineered optical system according to

$$\Delta z_{\max} = \frac{2\lambda d_0^2 L}{R^2 - \lambda^2 d_0^2 L^2 / R^2}, \quad (4.2)$$

where the variables λ , d_0 and R denote the wavelength, the object distance from the entrance pupil and the entrance pupil radius, respectively. The relationship is more complex for a general parameter ϵ , but it appears empirically that the depth range increases for decreasing ϵ .

The generalized Fresnel zone elements are considered as start designs for the following design process. In fact, the parameter set $[N, L, \epsilon]$ directly determines the number of peaks, the peak separation, the rotation rate, as well as the maximum depth range of the final element. The individual steps of the overall design process are depicted in Fig. 4.1 for the design of a phase distribution Φ_p of exemplary double- and triple-helix CGHs. For illustration purposes, Fig. 4.1 additionally provides the corresponding in-focus PSF distributions, which are calculated based on a Fourier transformation and considering a circular aperture. Figure 4.1(a) and 4.1(b) show the two Fresnel zone start design examples with design parameters $[N, L, \epsilon]$ equal to $[2, 16, 0.8]$ and $[3, 11, 0.8]$, respectively. Note that the corresponding PSFs provide comparable peak distances with respect to the optical axis. We find that each of the N PSF peaks can be allocated to a dedicated circular sector of the Fresnel zone design with azimuthal extensions of $2\pi/N$, respectively. Accordingly, the next design step only considers a single sector of the overall pupil area. In fact, restricting the design optimization to an individual subsection is essential in order to circumvent phase dislocations in the final phase element design. Figure 4.1(c) and 4.1(d) illustrate the respective sections and the corresponding PSF peak. Next, a modified version of the iterative optimization approach as proposed for the GL mode design approach [6] is applied. It is based on an Iterative Fourier Transform Algorithm (IFTA) and applies two main constraints. The first constraint maximizes the energy in the main lobes of the helical PSF for a high peak confinement. The second constraint enforces a phase only transfer function in the aperture plane. In contrast to the original method, the third constraint in the GL modal plane is voided and the pupil aperture is restricted to the circular sector of a single peak. The optimization results in a well-confined peak over a rotation range of $2\pi/N$ even for the large peak separations of the two examples, which are on the order of ten times the peak diameter. The obtained exemplary phase distributions are shown in Fig. 4.1(e) and 4.1(f). The remaining $N - 1$ circular sections of the CGH are subsequently filled with rotated copies of the optimized subarea as illustrated in Fig. 4.1(g) and 4.1(h). This leads to N equal peaks in the focal plane, which form a completely symmetric multi-order-helix PSF. Note that phase dislocations inside the CGH are only located at distinct lines, which separate the individual circular section. The phase distributions within each section can thus be easily transformed into continuous profiles by using a conventional one-dimensional phase unwrapping method [23]. Figure 4.1(i) and 4.1(j) show the respective profiles for the two design examples. We emphasize that these continuous pupil phase shifts can be realized by purely refractive (free-form) optical elements. These elements provide an improved performance when a broad spectral range is used for imaging. They offer minimized color artifacts, which is particularly critical for designs with a large peak separation. In fact, the double-helix

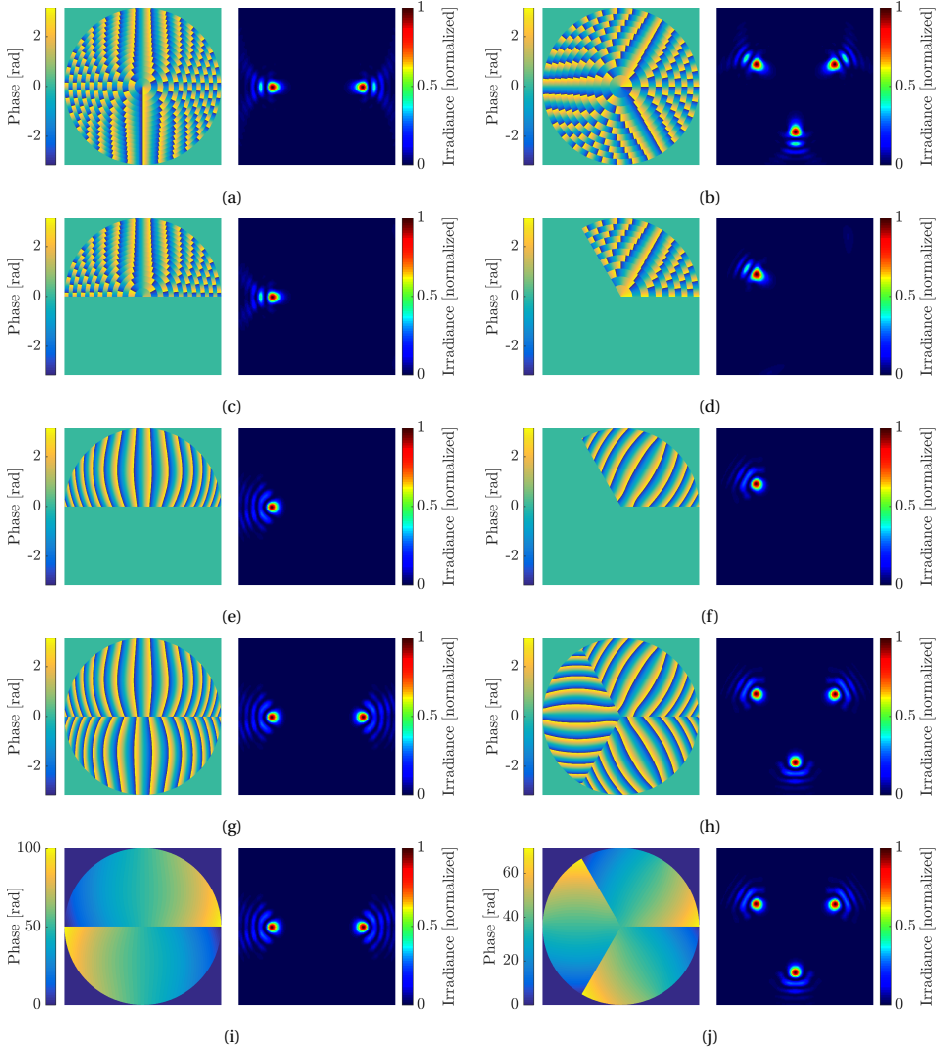


Figure 4.1: The individual steps of the proposed design process for multi-order-helix PSFs are exemplary illustrated for a double- (left column) and a triple- (right column) helix design. The phase distributions Φ_P as well as the corresponding PSFs are shown for the individual design steps. The Fresnel zone start designs (a,b) are initially truncated to an angular section, dedicated to a single PSF peak (c,d). The respective section is optimized for a high peak confinement (e,f) and subsequently used to fill the overall phase element with rotated copies (g,h). A purely refractive design is finally obtained by phase unwrapping in an optional step (i,j).

element shown in Fig. 4.1(i) is similar to the double wedge type designs that have already been proposed in the literature [24, 25]. However, our design approach enables an improved PSF confinement with minimized peak spreading over a customized defocus range as shown in the next subsection.

4.2.2. PERFORMANCE EVALUATION

The appropriateness of engineered PSFs for depth estimation is typically measured by the Cramér Rao Lower Bound (CRLB) [6, 9, 15], which quantifies the theoretical limit of precision in axial ranging. The CRLB for an imaged, broadband point source is given by [15]

$$\sigma_{\text{CRLB}}^{-2} = \frac{1}{\sigma_N^2} \sum_{v=1}^V \sum_{w=1}^W \left(\frac{\partial}{\partial z} H'[v, w; z] \right)^2, \quad (4.3)$$

where

$$H'[v, w; z] = \int_{\lambda_1}^{\lambda_2} \eta(\lambda) H[v, w; z; \lambda] d\lambda \quad (4.4)$$

is the incoherent superposition of the discretely sampled spectral PSF components and σ_{CRLB} defines the standard deviation of the lower limit to measurement precision. A system operating in the detector-limited regime is assumed in Eq. (4.3), which is applicable for imaging extended scenes with a generally high background level using low-end cameras with high readout noise. Accordingly, the readout noise and the shot noise of the background irradiance level dominate the shot noise from the peak signal. The parameter σ_N^2 denotes the variance of per-pixel noise, which is taken to be the sum of the two dominating noise contributions. Note that the three-dimensional PSF distribution $H'[v, w; z]$ is normalized such that their maximum irradiance is equal to one. A simplified, constant relative illumination spectrum $\eta(\lambda) = 1$, which ranges from $\lambda_1 = 450$ to $\lambda_2 = 650$ nm, is considered in the following.

The goal of the subsequent analysis is to compare the performance of different helical PSF designs under broadband imaging conditions. The optical system parameters used for the experimental study in section 5.5 are exemplarily applied for this investigation. A signal-to-noise ratio of 20 is assumed, which results in $\sigma_N = 0.05$. The designs under investigation include the double-helix Fresnel zone design, the optimized double- and triple-helix designs as well as the purely refractive double-helix design shown in Fig. 4.1(a), 4.1(g), 4.1(h) and 4.1(i), respectively. In addition, a nominal, clear aperture system is analysed as a reference. The broadband, axial distributions $H'[v, w; z]$ of the considered pupil functions are calculated at different object distances z and illustrated in the top part of Fig. 4.2. The selected axial range of 600 mm corresponds to a rotation of approximately 180° of the double-helix PSF designs. The rotation continues beyond this range but the double-helix peaks start experiencing significant spreading. In fact, the triple-helix design is only optimized for a range of approximately 300 mm but continues rotating beyond this range with accelerated peak spreading.

The simulated axial PSF distributions in the top part of Fig. 4.2 qualitatively illustrate the improved peak confinement of the novel, double-helix CGH design over the entire rotation range in comparison to the double-helix Fresnel zone design. The CRLB analysis moreover allows for a quantitative comparison, which shows that σ_{CRLB} is improved

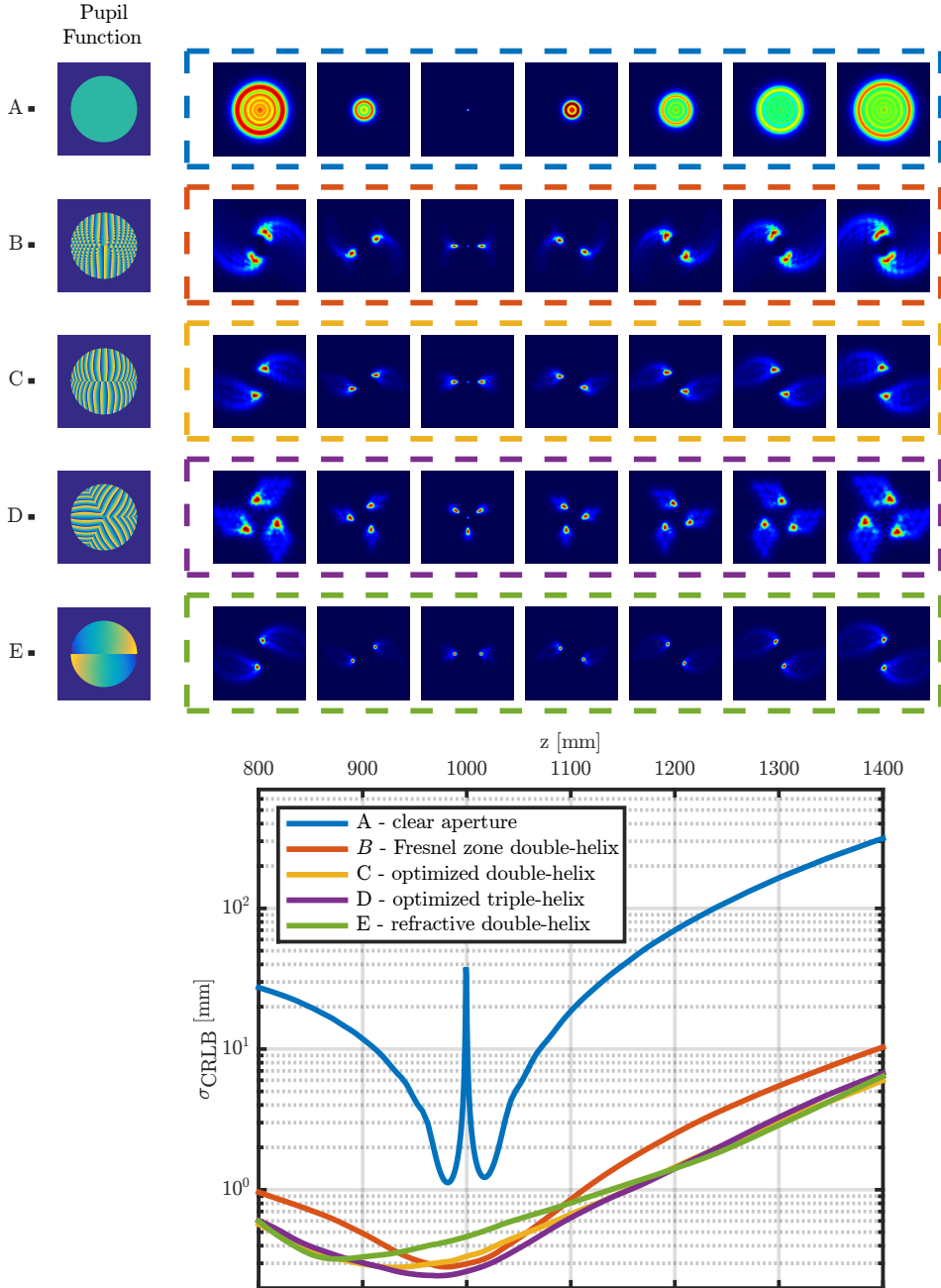


Figure 4.2: Top: Simulated, axial PSF dependency $H'[v, w; z]$ of five considered pupil functions as indicated in the left part: A, nominal PSF for a clear aperture; B, Fresnel zone double-helix PSF; C, optimized double-helix PSF; D, optimized triple-helix PSF; E, refractive double-helix PSF. A broadband illumination spectrum ranging from 450 – 650 nm is assumed. Bottom: Corresponding axial dependencies of the standard deviation of the lower limit to measurement precision σ_{CRLB} . Note that the nominal object distance is 1000 mm.

by a factor of 2 at the edges of the axial range of interest. In general, the proposed pupil engineered PSF designs feature superior values for σ_{CRLB} that are at least an order of magnitude decreased compared to the clear aperture system, which is consistent with previous results reported in [5, 9, 15]. In addition, the PSF comparison of the refractive double-helix design with the diffractive elements demonstrates their improved peak confinement under broadband imaging conditions. In particular, the PSFs of the diffractive elements in Fig. 4.2 comprise increased peak spreading in addition to the presence of a central peak at the nominal object distance. Both impairments of the PSF shape originate from a mismatch of the 2π phase jumps in the CGH design at wavelength that differ from the nominal wavelength. Finally, Fig. 4.2 reveals that the novel triple-helix design comprises a reduced axial resolution limit around the nominal object distance in comparison to the optimized double-helix design. In contrast, the axial resolution limit is increased for defocus values $|\Delta z| \gtrsim 100 \text{ mm}$, which is in accordance with the reduced axial range that is considered for the design optimization.

4

4.3. INFLUENCE OF ABERRATIONS ON PSF ROTATION

In the following investigation, the effect of individual optical aberrations on the rotation angle of multi-order-helix PSFs is analyzed. Initially, the influence is investigated by numerical simulations for the two design examples given in section 4.2 as well as a tetra-helix example with design parameters $[N, L, \epsilon] = [4, 8, 0.8]$. Note that no single peak design ($N = 1$) is considered, since it cannot be applied for 3D measurement using the approaches presented in [15, 16]. Finally, an analytic rotation assessment is provided for general, multi-helix CGH designs in order to obtain a theoretical understanding on which aberrations cause rotation. To this end, a general, quantitative measure for rotation of multi-order-helix PSFs is defined and evaluated in order to derive a general condition for identifying aberrations that result in a (false) PSF rotation.

4.3.1. NUMERICAL INVESTIGATION OF PSF ROTATION

The pupil phase $\Phi(u, v)$ of an aberrated, pupil engineered optical system is given by a superposition of the phase element part Φ_p and the aberrated part according to

$$\Phi(u, v) = \Phi_p(u, v) + \sum_{n,m} A_n^m \cdot Z_n^m(u, v), \quad (4.5)$$

where (u, v) denote the Cartesian coordinates of the pupil plane. The aberrated part is described by a set of Zernike polynomials Z_n^m and their respective amplitudes A_n^m . The individual polynomials Z_n^m are defined in polar coordinates by

$$Z_n^m(\rho, \phi) = R_n^m(\rho) \cos m\phi \quad (4.6)$$

for even and

$$Z_n^{-m}(\rho, \phi) = R_n^m(\rho) \sin m\phi \quad (4.7)$$

for odd polynomials, respectively. The term $R_n^m(\rho)$ denotes the radial dependency according to [26] and (m, n) are non-negative integers that satisfy $m \leq n$, $n - m = \text{even}$. The effect of first order Zernike aberrations on the double- and triple-helix PSF distributions is qualitatively shown in Fig. 4.3. The amplitude A_n^m of each Zernike aberration

is successively increased in Fig. 4.3, which introduces an rms phase error in a range of $[0, \pi/2]$ rad. Note that the first three modes associated with piston, tip and tilt errors are omitted, since they do not affect the PSF shape. The actual depth retrieval using helical PSFs is based on the desired rotation with an increasing amplitude of defocus (Z_2^0). However, Fig. 4.3 reveals that other Zernike aberrations lead to distortions of the original PSF shape that also give rise to an apparent rotation.

In order to quantify the effect on the rotation of the multi-order-helix PSF distributions,

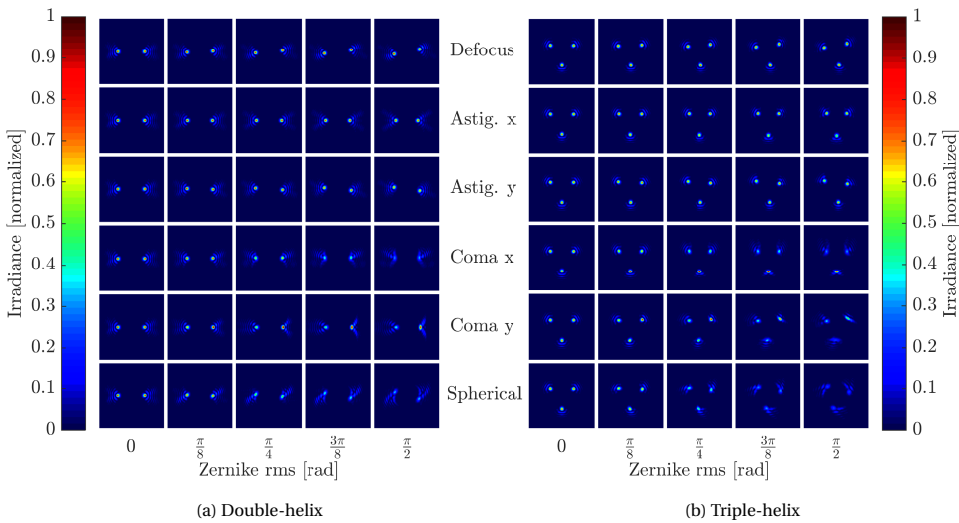


Figure 4.3: Influence of primary Zernike aberrations on the shape of an engineered (a) double- and (b) triple-helix PSF design including the effect of defocus (Z_2^0) as well as first order astigmatism (Z_2^{-2}, Z_2^2), coma (Z_3^{-1}, Z_3^1) and spherical aberration (Z_4^0).

an overall rotation angle α is defined as the average

$$\alpha = \frac{1}{N} \sum_{j=1}^N \Delta\alpha_j, \quad (4.8)$$

where $\Delta\alpha_j$ is the difference between the individual peak angle with and without aberrations, respectively. Note that the individual angles $\Delta\alpha_j$ can be positive or negative depending on the rotation direction. The change of the overall rotation angle α with increasing amplitudes of the first 21 Zernike aberrations is shown in Fig. 4.4 for the three multi-order-helix designs under investigation. The individual values are obtained by fitting N Gaussian peaks to the respective PSF distributions and extracting the fitted peak angle difference $\Delta\alpha_j$. The numerical fitting accuracy is on the order of 1° due to shape distortions and side lobes of the aberrated peaks. The overview in Fig. 4.4 demonstrates that the effect on the PSF rotation angle significantly depends on the particular Zernike mode as well as the order N of the engineered PSF. Aberrations that cause a significant rotation, i.e. $|\alpha(\pi/2)| > 1^\circ$, are highlighted by rectangular boxes in Fig. 4.4. An increasing

defocus rms error leads to the desired linear change of α for all three design examples, as expected. It can be seen that primary spherical aberration (Z_4^0) results in a significant increase of the rotation angle α as well. In contrast, the numerical simulations reveal that coma (Z_3^{-1}, Z_3^1) does not lead to a change of the overall rotation angle α . The effect of astigmatism (Z_2^{-2}, Z_2^2) depends on the particular CGH design. No rotation can be observed for the triple- and tetra-helix design, whereas the double-helix design is subject to significant rotation for astigmatism in x . In fact, the PSF distributions shown in Fig. 4.3(b) indicate that the individual peak angles of the triple-helix PSF vary indeed. However, the differences $\Delta\alpha_i$ appear to compensate each other. The results are in agreement with previous analyses of double-helix designs [17–19], which demonstrated a high rotation susceptibility to spherical aberration and astigmatism, but a robustness with respect to coma. A general trend can be observed in Fig. 4.4 that suggests that a higher number of peaks N leads to less modes that cause significant PSF rotation. The simulations particularly suggest that the overall rotation angle is zero unless the mode order m is a multiple of the PSF peak number N . In the following, we will develop a theoretical framework that explains this result.

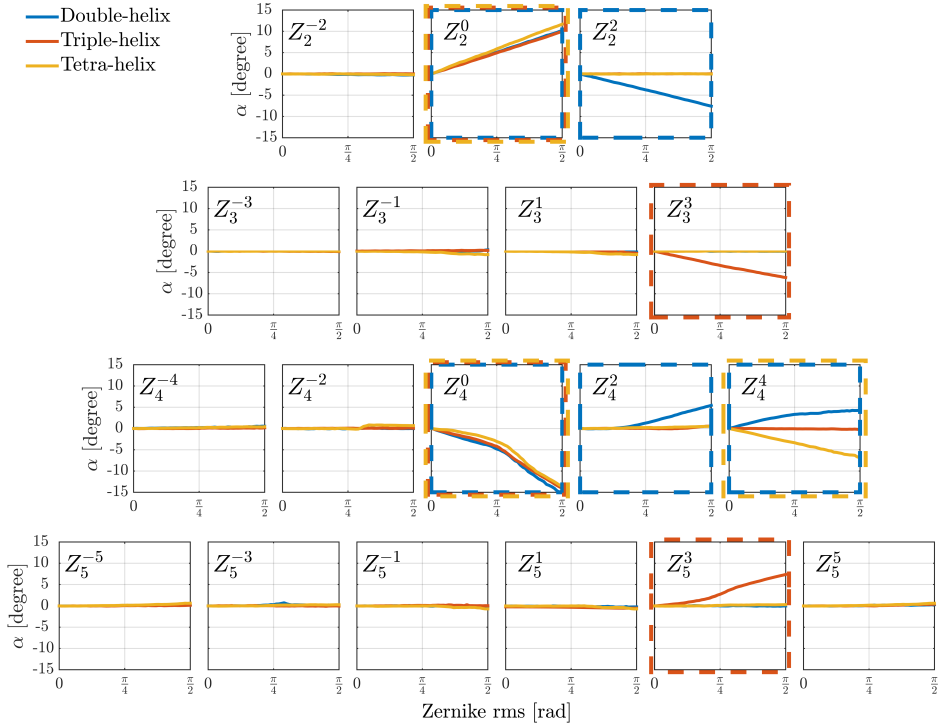


Figure 4.4: Comparison of the rotation angle dependency α of multi-helix-PSFs on the rms phase error for the first 21 Zernike aberrations (excluding piston, tip and tilt). Aberrations that cause a significant rotation, i.e. $|\alpha(\pi/2)| > 1^\circ$, on a particular multi-helix design are highlighted by rectangular boxes with the respective plot color.

4.3.2. THEORETICAL ROTATION ASSESSMENT

Considering geometrical optics, the two-dimensional position vector \vec{c} where a single ray intersects the image plane is determined by the local slope of the wave front $W(u, v)$ in the corresponding pupil location. The (coherent) superposition of all individual rays that emerge from an object point and pass through the pupil provides the centroid location of the PSF. As shown in [27], the centroid vector $\langle \vec{c} \rangle = (\langle c_x \rangle, \langle c_y \rangle)$ of the PSF according to wave optics is identical with that according to geometrical optics. It can be obtained by integrating the gradient distribution of the wavefront $W(u, v)$ over the exit pupil (EP) area according to:

$$\langle \vec{c} \rangle = -\frac{D}{E} \iint_{\text{EP}} \vec{\nabla} W(u, v) \, dudv \quad (4.9)$$

where D is the exit pupil distance to the image plane and E denotes a normalization factor. In the following, only a single Zernike aberration is considered. The wave front $W(u, v)$ of the aberrated, pupil engineered system is related to the pupil phase in Eq. (4.5) by the wavelength λ according to:

$$\begin{aligned} W(u, v) &= \frac{\lambda}{2\pi} \cdot \Phi(u, v) \\ &= \underbrace{\frac{\lambda}{2\pi} \cdot \Phi_p(u, v)}_{W_p} + \underbrace{\frac{\lambda}{2\pi} \cdot A_n^m \cdot Z_n^m(u, v)}_{W_n^m} \end{aligned} \quad (4.10)$$

and can be decomposed into a sum of the aberrated (Zernike) part $W_n^m(u, v)$ and the phase element part $W_p(u, v)$. The multi-order-helix design approach presented in section 4.2 demonstrates that the phase element effectively divides the wavefront $W(u, v)$ into N angular segments S_j in the pupil plane that are defined by the azimuthal range:

$$\frac{2\pi(j-1)}{N} \leq (\phi_u - \phi_0) < \frac{2\pi j}{N} \quad | \quad j = 1, \dots, N, \quad (4.11)$$

where ϕ_0 denotes a rotational offset. Each segment S_j directly corresponds to a particular PSF peak j . Therefore, the centroids $\langle \vec{c} \rangle_j$ of each partial wavefront $W_j(u, v)$ can be considered individually. We want to emphasize that this approximation is also applicable to the conventional design approaches based on GL-modes or Fresnel zones. The individual centroids are obtained by inserting Eq. (4.10) into Eq. (4.9), which leads to:

$$\begin{aligned} \langle \vec{c} \rangle_j &= -\frac{D}{E} \iint_{S_j} \vec{\nabla} W(u, v) \, dudv \\ &= -\frac{D}{E} \iint_{S_j} \vec{\nabla} W_p(u, v) \, dudv - \frac{D}{E} \iint_{S_j} \vec{\nabla} W_n^m(u, v) \, dudv \\ &= \langle \vec{p} \rangle_j + \langle \vec{z}_n^m \rangle_j \end{aligned} \quad (4.12)$$

Figure 4.5(a) illustrates the respective subareas S_1 and S_2 of the phase element part $W_p(u, v)$ for the double-helix design. Furthermore, the corresponding gradient vector distribution, which needs to be integrated over the subareas to determine the centroid

vectors according to Eq. (4.9) is indicated. An equivalent plot of defocus aberration $W_2^0(u, v)$ is shown in Fig. 4.5(b). The respective vectors $\langle \vec{p} \rangle_j$ and $\langle \vec{z}_n^m \rangle_j$ according to Eq. (4.12) are indicated in Fig. 4.5(c) for the exemplary case of a defocus aberration on a double-helix design. Note that the centroid positions of the individual PSF peaks do not quantitatively match the peak locations detected by a Gaussian fit, which is due to the side lobes in combination with spot deformations and the background irradiance level. However, both methods to locate the PSF peaks agree on the presence or absence of rotation, which is the main goal of this theoretical investigation.

In general, the deformation of a ring of N engineered PSF peaks can be described geometrically by an overall shift, a scaling, an anisotropic stretch and a rotation, provided that the deformation of the shape of the sub-spots themselves is neglected. Accordingly, we define the (scalar) measure:

$$M_n^m = \hat{z} \cdot \left(\sum_{j=1}^N \langle \vec{p} \rangle_j \times \langle \vec{z}_n^m \rangle_j \right), \quad (4.13)$$

where \hat{z} is the unit vector in the z -direction (along optical axis). The measure M_n^m is only sensitive to rotation and not affected by the other shape distortions. The detailed

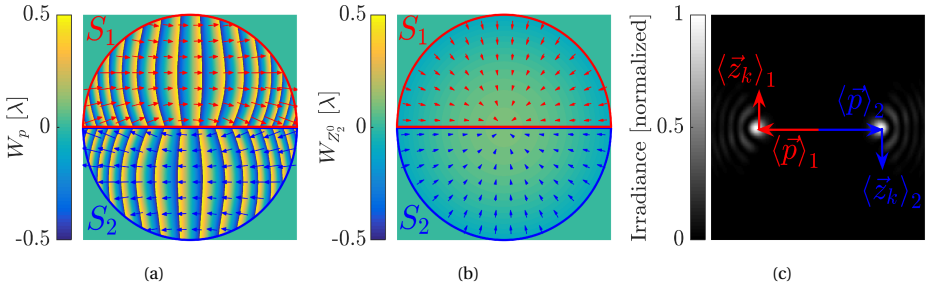


Figure 4.5: Wavefront distribution of (a) phase element part W_p and (b) defocus aberration part $W_{z_2^0}$ (b) as well as respective gradient fields $\vec{\nabla}W_p$ and $\vec{\nabla}W_{z_4}$. The two highlighted subareas S_1 and S_2 directly correspond to the two peaks of the double-helix PSF. (c) PSF distribution associated with W_p . The direction of the centroid vectors $\langle \vec{p} \rangle$ and $\langle \vec{z}_k \rangle$ are indicated for both subareas S_1 and S_2 , respectively.

evaluation of the PSF rotation measure M_n^m is disclosed in the appendix (see section 4.6). The theoretical analysis proves that an aberrated wavefront W_n^m only leads to rotation of a multi-order-helix PSF (i.e. $M_n^m \neq 0$), if the azimuthal order m is an integer multiple κ of the peak number N according to the derived condition

$$m = \kappa \cdot N \quad | \quad \kappa = 0, 1, 2, \dots \quad (4.14)$$

which provides the major outcome of the assessment. It particularly demonstrates that all types of multi-order-helix PSFs are sensitive to spherical aberration of all orders (Z_4^0, Z_6^0, \dots). Moreover, it reveals that double-helix designs are sensitive to astigmatism of all orders ($Z_2^{\pm 2}, Z_4^{\pm 2}, \dots$), whereas higher-order designs are not. In fact, triple-helix designs are sensitive to trefoil of all orders ($Z_3^{\pm 3}, Z_5^{\pm 3}, \dots$), tetra-helix designs to tetrafoil etc. In addition, the rotation measure for odd Zernike aberrations in Eq. (4.34) vanishes for

the particular case of $\phi_0 = 0$. These results are in agreement with the numerical simulations performed in section 4.3.1 and qualitatively match the rotation angle investigation shown in Fig. 4.4. In general, the analysis verifies that a higher number of peaks N leads to less Zernike modes that result in (unwanted) rotation and thus provides an increased aberration robustness with regard to monocular depth measurements. However, it should be recalled from section 4.2 that a larger parameter N results in a reduced depth range of $[-\pi/N, \pi/N]$ at the same time.

4.4. EXPERIMENTAL RESULTS

4.4.1. OPTICAL SETUP

A demonstration setup based on a hybrid optical imaging system is realized according to the system concept proposed in [16]. The three phase element designs studied in section 4.3 (double-, triple- and tetra-helix) are implemented using state-of-the-art micro-optics manufacturing processes on wafer-scale. A thin photoresist layer is initially spun on a borosilicate glass substrate and subsequently structured using the LED writing lithography approach presented by Eckstein et al. in [28]. The next steps provide a significant advancement in the manufacturing of phase elements for monocular depth estimation compared to previous elements [10, 16]. The surface profile of the photoresist layer is directly transferred onto the borosilicate glass substrate by applying reactive-ion-etching to generate a highly accurate and robust imprinting tool. Subsequently, a thin polymer layer is deposited on a second borosilicate glass substrate. The final wafer is obtained by transferring the surface profile of the tool to the polymer layer of the second substrate using UV-imprinting. We want to emphasize that the etched borosilicate glass tool potentially allows for manufacturing large numbers of polymer-on-glass wafers containing the respective phase elements. In addition to the high cost-efficiency, the utilized hybrid polymers, such as ORMOCERE[®] [29], provide increased temperature and mechanical stability, as well as improved transparency over the entire visual range compared to previous elements that were directly realized in a photo resist layer. However, the main challenge relies in minimizing surfaces distortions during the replication process, which would directly compromise the performance of the CGH with respect to the introduced wave front error. The final optical elements are obtained by dicing the manufactured wafers and mounting the individual designs in customized, opaque frames, which define circular apertures of 10 mm diameter. The measured surface profiles $h(x, y)$ of the tool and the replication are plotted in Fig. 4.6 for the double-helix CGH design. The plot shows that the profile of the tool element accurately complies with the phase element design shown in Fig. 4.1 (g). Moreover, the surface measurement of the replicated element demonstrates the successful transfer of the tool profile using UV replication. The apparent shape deviation is likely due to a bending of the 1 mm thin replication substrate, which does, however, not affect the PSF distribution significantly. A quantitative analysis of the residual wavefront error would additionally require the profile of the substrates back side, which is not directly accessible using a white light interferometer measurement.

An optical system based on two achromatic doublets (Thorlabs AC254-200-A and AC254-100-A) is set up to verify the functionality of the new phase elements and further to

demonstrate the enhanced aberration robustness of high-order-helix designs. A frame with a particular CGH design can be placed in front of the two lenses, where it defines the entrance pupil of the optical demonstration system. The resulting setup, which is characterized by a focal length of 71 mm and an F-number of 7.4, is placed in front of a commercial camera system (AVT Pike F-505). The monochrome 2/3 inch CCD sensor (Sony ICX625) provides a pixel size of $3.45\text{ }\mu\text{m}$ and a total pixel count of 2452×2054 , which leads to an overall field of view (FOV) of $114\text{ mm} \times 96\text{ mm}$ at the nominal object distance of 1 m . The system provides diffraction limited performance on the optical axis for the design wavelength of 540 nm . However, it is intentionally subject to significant off-axis aberrations dominated by astigmatism and field curvature.

4

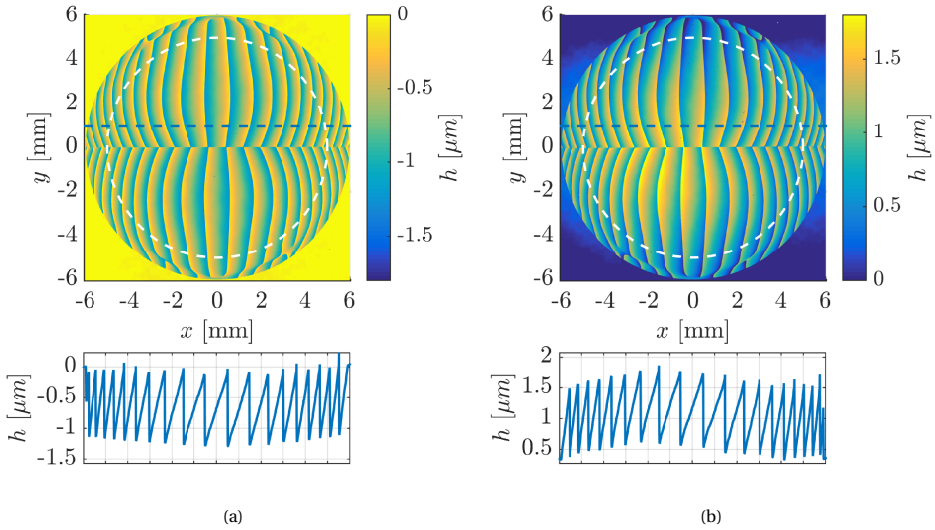


Figure 4.6: Top: Measured surface profile height $h(x, y)$ of (a) the tool and (b) the replication of the double-helix CGH design. The dashed white circle indicates the aperture size of 10 mm used in the optical setup. Bottom: horizontal cross-section of the profile height $h(x)$ at $y = 1\text{ mm}$ as indicated by dashed blue lines in the respective upper plots.

4.4.2. DEMONSTRATION OF ON-AXIS PSF ROTATION

Initially, the depth dependent rotation of the engineered PSF is investigated for the three CGH designs of interest. To this end, an on-axis LED point source with a peak irradiance at 540 nm is imaged for different object distances in a range between 860 mm and 1180 mm , which covers the optimized 90° rotation range of the tetra-helix PSF design. It is pointed out that the double- and triple helix PSFs continue rotating beyond this range. The top part of Fig. 4.7 illustrates the respective PSF distributions at multiple object distances. The displayed irradiance levels are normalized to the maximum peak value at $z = 1000\text{ mm}$ for each design, respectively. The individual plots demonstrate a continuous PSF rotation, featuring clearly defined peaks. Solely one of the tetra helix PSF spots exhibits accelerated spreading with increasing object distance. This may be attributed

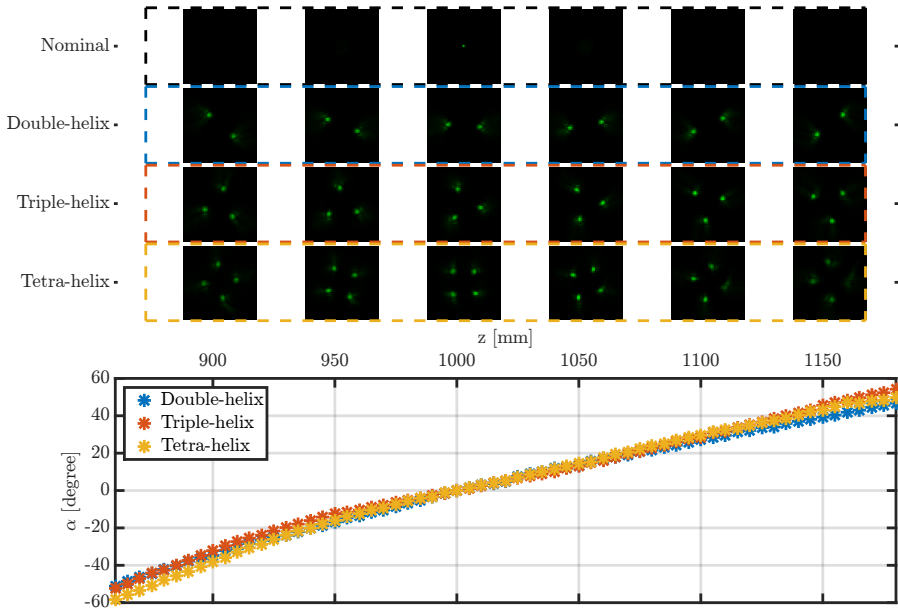


Figure 4.7: Top: Measured on-axis distributions of the engineered double-, triple- and tetra-helix PSFs at multiple object distances z ($\lambda = 540 \text{ nm}$). Bottom: Corresponding dependency of the rotation angle α on the object distance z .

to minor CGH distortions introduced during the manufacturing process, which affect the individual focus position as well as the depth of focus of the PSF spots. Nevertheless, Fig. 4.7 demonstrates that the helical PSF shape of all realized PSFs is maintained throughout an extended axial range of at least 300 mm . Accordingly, the axial range significantly extends over the diffraction limited depth of field of the nominal PSF, which is in the order of $\lambda/\text{NA}^2 \approx 22 \text{ mm}$. The bottom part of Fig. 4.7 shows a close to linear dependency of the rotation angle α on the object distance z . The individual data points are obtained by fitting N Gaussian peaks to the respective PSF images and averaging over the fitted angular changes $\Delta\alpha_i$ according to Eq. (4.8). The center of each helical PSF is determined by calculating the center of gravity of the individual distributions. Note that the respective localization accuracy, which is limited by noise and a finite sampling, is in the same order as the accuracy of the peak localization and adds a comparable error contribution to the overall rotation angle measurement. In fact, the angle determination for the tetra-helix design is ambiguous for angles $|\alpha| > 45^\circ$, which generally prohibits a depth retrieval beyond this angle. Prior knowledge on the rotation is used in Fig. 4.7 to circumvent these ambiguities for comparison purposes only. The PSFs feature comparable rotation rates $\Delta\alpha/\Delta z$ on the order of $0.3^\circ/\text{mm}$, which is in accordance with the design parameters of the three CGHs due to the similar values of $N \cdot L$. Moreover, the peak distances p of approximately 12 pixels also agree for the three designs. Finally, we point out that the proper functionality of the replicated phase elements with respect to the PSF rotation confirms the successful manufacturing by UV replication. Thus, we ver-

ified a cost-efficient manufacturing approach of pupil engineering CGHs with enhanced optical, thermal and mechanical properties compared to previous photoresist-on-glass elements for monocular, three-dimensional imaging.

4.4.3. PSF ROTATION ACROSS AN EXTENDED FIELD OF VIEW

IMAGE ACQUISITION

We exploit the severe off-axis aberrations of the demonstration setup in order to provide experimental verification of the superior aberration robustness of high-order-helix designs. To this end, the pupil engineered image of a planar screen located at the nominal object distance of 1 m and homogeneously illuminated by the previously applied LED source, is acquired. Figure 4.8(a) shows the nominal image distribution if no phase element is mounted inside the aperture stop. The white screen features a random pattern of black dots, which provide the required spatial features for the following analysis. It can already be observed that the image quality is significantly decreased at the edges of the field of view due to field curvature and astigmatism. The three CGHs with the designs under investigation are successively incorporated to image the same scene. For comparison purposes, only the central portion of the overall FOV is shown in Fig. 4.8(b)-4.8(e) for each of the three PSF designs in addition to the nominal case without a CGH, respectively. The shown subimages illustrate the effect of pupil engineering, which can be modeled as a convolution of the helical PSFs, shown in Fig. 4.7, with the nominal subimage shown in Fig. 4.8(b).

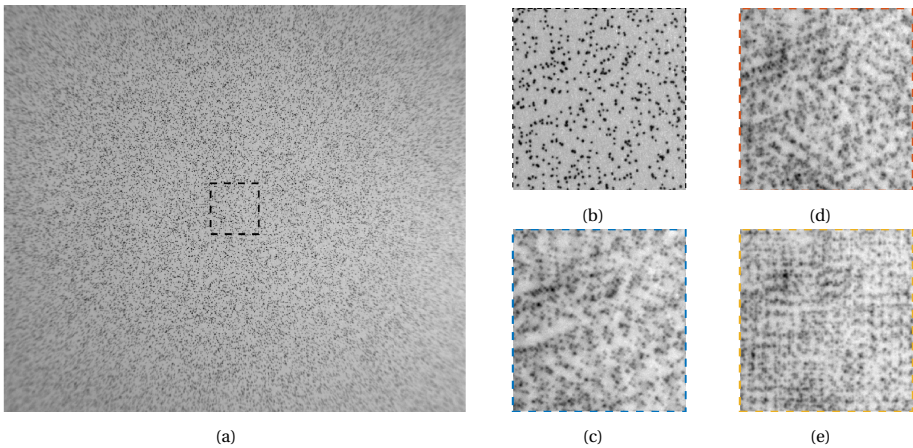


Figure 4.8: (a) Nominal distribution of the imaged test screen if no CGH is implemented in the demonstration system. The subimage shown in (b) correspond to the inset indicated in (a). The subimages (c)-(e) show the same part of the image after the double-, triple- and tetra-helix CGHs are implemented in the demonstration system, respectively.

CEPSTRUM DISTRIBUTION

The cepstrum approach previously introduced by us [16] is used in order to extract the lateral rotation angle distribution $\alpha(x, y)$ of the engineered PSFs from the acquired images. This method is based on calculating the image cepstrum in a local environment

around (x, y) and searching for peaks in the cepstrum domain. The location of the cepstrum peaks provides the information on the local PSF rotation. The approach was initially developed for double-helix designs but can be extended in order to accommodate for higher-order-helix PSFs. In fact, the number of first order peaks K in the cepstrum domain is equal to $N(N - 1)$ for the rotating PSF designs introduced in section 4.2. However, peaks in the cepstrum may overlap due to symmetry in the respective PSF. This is the case for high-order-helix PSFs with even peak numbers and $N > 2$. The corresponding number of distinguishable peaks reduces to $N^2/2$. In addition, aberrations can change the number of cepstrum peaks that can be distinguished by changing the PSF shape and thus eliminating or adding symmetry in the PSF peak locations. Figure 4.9 illustrates the cepstrum of the 256×256 pixel subimages shown in Fig. 4.8(c)-4.8(e), respectively, after a Hann window is applied to mitigate edge effects. Note that these distributions are smoothed and the regions of interest are truncated as described in [16] in order to isolate first order cepstrum peaks. It can be observed that the double- and triple-helix designs exhibit clearly distinguishable cepstrum peaks with a constant radial distance and comparable magnitudes. The peaks of the tetra-helix design are, however, located at different radial distances and partially overlap, which results in 8 distinguishable peaks.

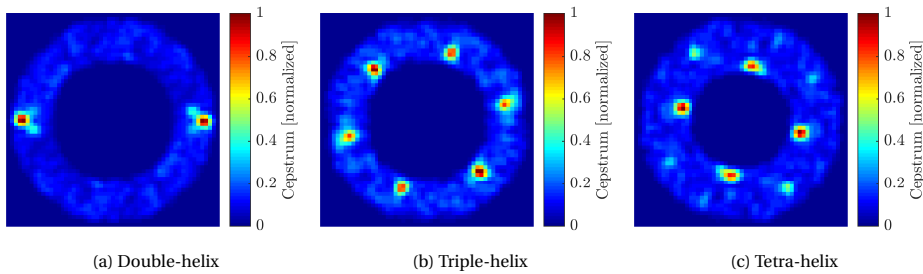


Figure 4.9: Processed Cepstrum distributions of the subimages shown in Fig. 4.8(c)-4.8(e).

ROTATION ANGLE ANALYSIS

The information on the location of the cepstrum peaks is used to determine to the rotation angle α and in that way enable a local depth estimation. Due to the complex tetra-helix cepstrum distribution with varying peak distances and overlapping peaks, we limit ourselves to the double- and triple-helix design in order to demonstrate the difference in aberration robustness. The local cepstrum distributions are calculated for each image position (x, y) in a 256×256 pixel environment. The first order cepstrum peaks are located by fitting Gaussian functions to the peaks. The overall rotation angle α directly corresponds to the average of the $K/2$ peak angle changes in the cepstrum domain. It is noted that the cepstrum approach reduces the unambiguous angular rotation range of the triple-helix designs by a factor of two, i.e. $[-30^\circ, 30^\circ]$, due to the PSF symmetry. The calculated overall rotation angle distribution of the test images are shown in Fig. 4.10(a) and 4.10(c). It can be observed that $\alpha(x, y)$ is increasing towards the edges of the FOV despite the constant depth of the imaged screen. This observation can be related to a

significant field curvature, a field dependent defocus aberration (Z_2^0) that results in undesired rotation for all multi-order-helix designs. Note that a comparison between the two plots yet reveals a significant shape deviation.

In order to eliminate the effect of field curvature and enable the analysis of effects from other aberrations, a parabolic function is fitted and subtracted from the rotation angle distribution $\alpha(x, y)$. In practice, this could be achieved by incorporating a customized field flattening element in close proximity to the image sensor. Figure 4.10(c) and 4.10(d) show the respective angular distributions $\alpha_r(x, y)$ with field curvature removed. The remaining error is mainly due to field dependent astigmatism, which results in false PSF rotation for the double-helix design, as predicted in section 4.3. In contrast, the triple-helix design does not suffer from this error, which allows for a significantly increased accuracy of the depth measurement. The RMS error in the angle estimation over the entire FOV is reduced from 1.7° to 0.3° , which demonstrates the superior aberration robustness of a high-order-helix PSF compared to the conventional double-helix PSF shape. We emphasize that the improved robustness is particularly crucial for low-NA, large FOV optical systems in machine vision or automotive applications, where astigmatism is one of the major aberrations.

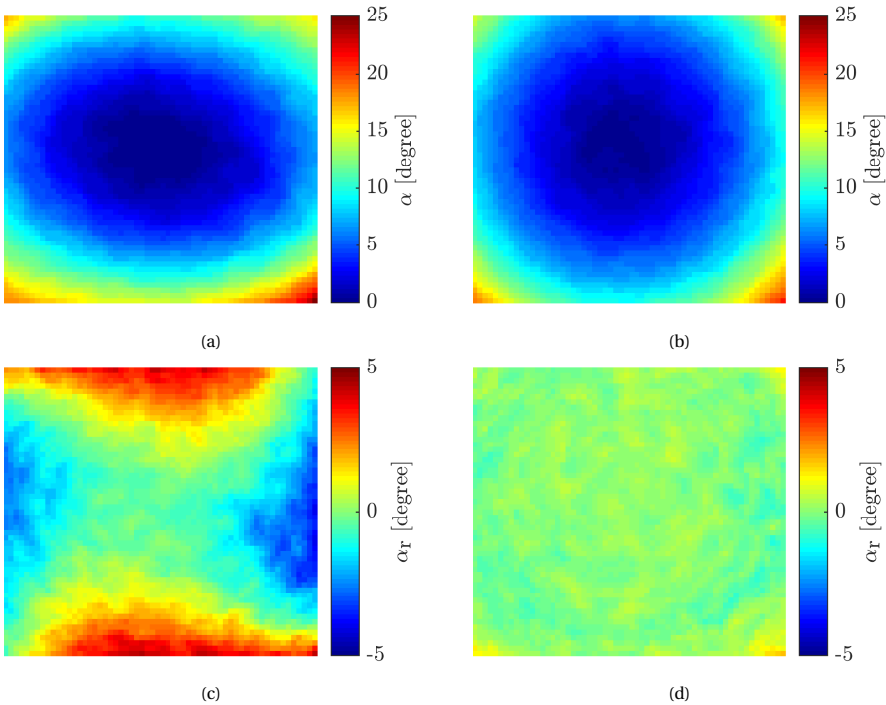


Figure 4.10: Measured rotation angle distribution α of the imaged demonstration scene using a (a) double- and (b) triple-helix PSF. (c) and (d) show the residual rotation angle distributions $\alpha_r(x, y)$ for the two cases after eliminating the effect of field curvature by fitting and subtracting a parabolic function from $\alpha(x, y)$.

4.5. CONCLUSION

A novel approach for the design of phase elements to generate engineered, multi-order-helix PSFs with a depth dependent rotation is presented. The approach is based on a combination of two previously introduced design methods and enables PSF distributions with a large peak separation and a high peak confinement over an extended depth range. In addition, it allows for the design of purely refractive optical elements, which potentially provide an enhanced imaging performance with respect to color artifacts. The performance of the novel designs is assessed based on Cramér-Rao Lower Bound analysis. The influence of Zernike aberrations on the rotation of engineered, multi-order-helix PSFs has been investigated. The numerical analysis revealed that high-order-helix designs ($N > 2$) facilitate a more robust depth estimation in the presence of aberrations. In particular, a theoretical assessment showed that only Zernike aberrations with an azimuthal order $m = \kappa \cdot N$ ($\kappa = 0, 1, 2, \dots$) lead to PSF rotation.

Furthermore, the successful manufacturing of cost-efficient phase elements based on UV-replication on wafer-scale is verified. A demonstration system has been implemented to demonstrate the proper depth dependent rotation of novel triple- and tetra-helix PSF designs. In addition to a theoretical assessment, the superior aberration robustness of high-order-helix designs is demonstrated experimentally by analyzing the rotation angle distribution of an imaged scene.

The main goal of this paper is to provide a basis for balancing optical aberrations during the design process of pupil engineered, 3D imaging systems, which require minimized unwanted PSF rotation for an accurate monocular depth measurement. In contrast, future work will include investigating the possibility for a dedicated measurement of aberrated wavefronts using optical systems that feature a multi-order-helix PSF. In particular, we aim to exploit the effect of different aberrations on the shape of the PSF in order to extract information on present aberrations for potential applications such as adaptive optics.

It is mentioned that higher order helix PSFs can also find application in the field of single molecule imaging, where imaging at relatively large depth in cells and tissue gains considerable importance, implying that aberration robust PSFs could potentially be of use.

4.6. APPENDIX: EVALUATION OF ROTATION MEASURE M_n^m

The evaluation of the measure for PSF rotation M_n^m , as introduced in Eq. (4.13), is provided in the following. The centroid positions $\langle \vec{p} \rangle_j$ of each multi-order-helix PSF peak $j = 1, 2, \dots, N$ can be written as:

$$\langle \vec{p} \rangle_j = p \cdot \begin{pmatrix} \cos \phi_j \\ \sin \phi_j \end{pmatrix}, \quad (4.15)$$

where:

$$\phi_j = \phi_0 + \frac{\pi}{2} - \frac{\pi}{N} + j \frac{2\pi}{N} \quad (4.16)$$

according to the design approach described in section 4.2. After transition to polar coordinates, the position vectors can be expressed as:

$$\langle \vec{p} \rangle_j = p \cos(\phi - \phi_j) \hat{\rho} - p \sin(\phi - \phi_j) \hat{\phi}, \quad (4.17)$$

where $\hat{\rho}$ and $\hat{\phi}$ are unit vectors in the radial and azimuthal direction, and p is the distance of the peak to the PSF center. The Zernike centroid vector $\langle \vec{z}_n^m \rangle_j$ is determined by the gradient in polar coordinates according to:

$$\langle \vec{z}_n^m \rangle_j = \langle -\vec{\nabla} W_n^m \rangle_j = \left\langle -\frac{\partial W_n^m}{\partial \rho} \hat{\rho} - \frac{1}{\rho} \frac{\partial W_n^m}{\partial \phi} \hat{\phi} \right\rangle_j \quad (4.18)$$

Inserting Eq. (4.17) and Eq. (4.18) into the rotation measure defined in Eq. (4.13) leads to the following expression:

$$M_n^m = p \cdot \sum_{j=1}^N \left\langle -\frac{1}{\rho} \cos(\phi - \phi_j) \frac{\partial W_n^m}{\partial \phi} - \sin(\phi - \phi_j) \frac{\partial W_n^m}{\partial \rho} \right\rangle_j \quad (4.19)$$

The integration variable $\psi = 2\pi j/N + \phi_0 - \phi$ is used for the average over the pupil in Eq. (4.19) so that for all segments j the integration range is:

$$0 \leq \psi \leq \frac{2\pi}{N} \quad (4.20)$$

The rotation measure then follows as:

$$M_n^m = \frac{pD}{E} \int_{\rho=0}^1 \int_{\psi=0}^{2\pi/N} \sum_{j=1}^N \left[\frac{1}{\rho} \sin\left(\frac{\pi}{N} - \psi\right) \frac{\partial W_n^m\left(\rho, \frac{2\pi j}{N} + \phi_0 - \psi\right)}{\partial \psi} \right. \\ \left. + \cos\left(\frac{\pi}{N} - \psi\right) \frac{\partial W_n^m\left(\rho, \frac{2\pi j}{N} + \phi_0 - \psi\right)}{\partial \rho} \right] \rho d\rho d\psi \quad (4.21)$$

First, the rotation measure is considered for even Zernike aberration functions Z_n^m defined in Eq. (4.6), which includes modes with $m = 0$. It can be written as:

$$M_n^m = \frac{2\pi p D A_n^m}{\lambda E} \left[m F_{ss} \int_{\rho=0}^1 R_n^m(\rho) d\rho + F_{cc} \int_{\rho=0}^1 \rho \frac{\partial R_n^m(\rho)}{\partial \rho} d\rho \right] \quad (4.22)$$

using the definition of W_n^m in Eq. (4.10). The two respective integrals over the azimuthal angle ψ are defined by:

$$F_{ss} = \int_{\psi=0}^{2\pi/N} \left[\sin\left(\frac{\pi}{N} - \psi\right) \sum_{j=1}^N \sin\left(\frac{2\pi j m}{N} + m\phi_0 - m\psi\right) \right] d\psi \quad (4.23)$$

$$F_{cc} = \int_{\psi=0}^{2\pi/N} \left[\cos\left(\frac{\pi}{N} - \psi\right) \sum_{j=1}^N \cos\left(\frac{2\pi j m}{N} + m\phi_0 - m\psi\right) \right] d\psi \quad (4.24)$$

In fact, both integrals equal zero unless m is a multiple of the PSF peak number N according to:

$$m = \kappa \cdot N \quad | \quad \kappa = 0, 1, 2, \dots \quad (4.25)$$

For these specific cases, the integrals take the form:

$$F_{ss} = \frac{N}{\kappa^2 N^2 - 1} \left[-2\kappa N \sin\left(\frac{\pi}{N}\right) \cos(\kappa N \phi_0) \right] \quad (4.26)$$

$$F_{cc} = \frac{N}{\kappa^2 N^2 - 1} \left[-2 \sin\left(\frac{\pi}{N}\right) \cos(\kappa N \phi_0) \right] \quad (4.27)$$

The latter integral over the radial coordinate in Eq. (4.22) can be simplified by partial integration according to:

$$\int_{\rho=0}^1 \rho \frac{\partial R_n^m(\rho)}{\partial \rho} d\rho = 1 - \int_{\rho=0}^1 R_n^m(\rho) d\rho \quad (4.28)$$

The remaining integral over the the radial Zernike polynomial R_n^m turns out to be:

$$\int_{\rho=0}^1 R_n^m(\rho) d\rho = \frac{(-1)^{(n-m)/2}}{(n+1)} \quad (4.29)$$

This result was found using Mathematica, but no formal proof could be found in the literature. Thus, the rotation measure in Eq. (4.22) takes the form:

$$M_n^m = \frac{2\pi p D A_n^m}{\lambda E} \left[F_{cc} + (m F_{ss} - F_{cc}) \left((-1)^{(n-m)/2} \cdot \frac{1}{(n+1)} \right) \right] \quad (4.30)$$

Inserting Eq. (4.26) and Eq. (4.27) in Eq. (4.30) and considering only Zernike aberrations that fulfill condition (4.25) results in:

$$M_n^{\kappa N} = \frac{-4\pi p D A_n^{\kappa N} N}{\lambda E (\kappa^2 N^2 - 1)} \sin\left(\frac{\pi}{N}\right) \cos(\kappa N \phi_0) \left[1 + \left((-1)^{(n-\kappa N)/2} \cdot \frac{(\kappa^2 N^2 - 1)}{(n+1)} \right) \right] \quad (4.31)$$

For odd Zernike aberration functions defined in Eq. (4.7) the two integrals over the azimuthal angle ψ in Eq. (4.21) also equal zero unless condition (4.25) is fulfilled. In this case, the respective integrals take the form

$$F_{sc} = \frac{N}{\kappa^2 N^2 - 1} \left[2\kappa N (-1)^\kappa \sin\left(\frac{\pi}{N}\right) \sin(\kappa N \phi_0) \right] \quad (4.32)$$

$$F_{cs} = \frac{N}{\kappa^2 N^2 - 1} \left[-2(-1)^\kappa \sin\left(\frac{\pi}{N}\right) \sin(\kappa N \phi_0) \right] \quad (4.33)$$

and the rotation measure results in

$$M_n^{-\kappa N} = (-1)^\kappa \frac{-4\pi p D A_n^{\kappa N} N}{\lambda E (\kappa^2 N^2 - 1)} \sin\left(\frac{\pi}{N}\right) \sin(\kappa N \phi_0) \left[1 - \left((-1)^{(n-\kappa N)/2} \cdot \frac{(\kappa^2 N^2 + 1)}{(n+1)} \right) \right] \quad (4.34)$$

FUNDING

This work was performed in the frame of the Photonics Research Germany funding program by the German Federal Ministry of Education and Research under contract 13N13667.

ACKNOWLEDGMENTS

The authors would like to thank Marko Stumpf, Andre Matthes and Peter Dannberg for manufacturing the CGHs, as well as Jens Dunkel for performing the surface profile measurements.

REFERENCES

- [1] R. Berlich and S. Stallinga, *High-order-helix point spread functions for monocular three-dimensional imaging with superior aberration robustness*, *Opt. Express* **26**, 4873 (2018).
- [2] E. R. Dowski and W. T. Cathey, *Extended depth of field through wave-front coding*, *Applied Optics* **34**, 1859 (1995).
- [3] A. Castro and J. Ojeda-Castañeda, *Asymmetric phase masks for extended depth of field*, *Applied Optics* **43**, 3474 (2004).
- [4] Q. Yang, L. Liu, and J. Sun, *Optimized phase pupil masks for extended depth of field*, *Optics Communications* **272**, 56 (2007).
- [5] A. Greengard, Y. Y. Schechner, and R. Piestun, *Depth from diffracted rotation*, *Optics Letters* **31**, 181 (2006).
- [6] S. R. P. Pavani and R. Piestun, *High-efficiency rotating point spread functions*, *Optics express* **16**, 3484 (2008).
- [7] S. Prasad, *Rotating point spread function via pupil-phase engineering*, *Optics Letters* **38**, 585 (2013).
- [8] S. R. P. Pavani and R. Piestun, *Three dimensional tracking of fluorescent microparticles using a photon-limited double-helix response system*, *Optics express* **16**, 22048 (2008).
- [9] S. R. P. Pavani, A. Greengard, and R. Piestun, *Three-dimensional localization with nanometer accuracy using a detector-limited double-helix point spread function system*, *Applied Physics Letters* **95**, 021103 (2009).
- [10] G. Grover, S. Quirin, C. Fiedler, and R. Piestun, *Photon efficient double-helix psf microscopy with application to 3d photo-activation localization imaging*, *Biomedical optics express* **2**, 3010 (2011).
- [11] A. Barsic, G. Grover, and R. Piestun, *Three-dimensional super-resolution and localization of dense clusters of single molecules*, *Scientific reports* **4**, 5388 (2014).

- [12] C. Roider, A. Jesacher, S. Bernet, and M. Ritsch-Marte, *Axial super-localisation using rotating point spread functions shaped by polarisation-dependent phase modulation*, *Optics express* **22**, 4029 (2014).
- [13] S. Quirin, G. Grover, and R. Piestun, *Optimal 3d single-molecule super-resolution microscopy with engineered point spread functions*, in *Proceedings - International Symposium on Biomedical Imaging* (2012) pp. 926–927.
- [14] C. Roider, R. Heintzmann, R. Piestun, and A. Jesacher, *Deconvolution approach for 3d scanning microscopy with helical phase engineering*, *Optics express* **24**, 15456 (2016).
- [15] S. Quirin and R. Piestun, *Depth estimation and image recovery using broadband, incoherent illumination with engineered point spread functions invited*, *Applied Optics* **52**, A367 (2013).
- [16] R. Berlich, A. Bräuer, and S. Stallinga, *Single shot three-dimensional imaging using an engineered point spread function*, *Trans. Pattern Anal. Mach. Intell. IEEE Trans. Info. Theory IEEE Signal Process. Mag. IEEE Signal Process. Mag. ICIP06 OPTICS EXPRESS* **24**, 5946 (2016).
- [17] S. Ghosh and C. Preza, *Characterization of a three-dimensional double-helix point-spread function for fluorescence microscopy in the presence of spherical aberration*, *Journal of Biomedical Optics* **18**, 036010 (2013).
- [18] Z. Cao and K. Wang, *Effects of astigmatism and coma on rotating point spread function*, *Applied Optics* **53**, 7325 (2014).
- [19] M. Baránek, P. Bouchal, M. Šiler, and Z. Bouchal, *Aberration resistant axial localization using a self-imaging of vortices*, *Optics express* **23**, 15316 (2015).
- [20] R. Piestun and J. Shamir, *Generalized propagation-invariant wave fields*, *Journal of the Optical Society of America A* **15**, 3039 (1998).
- [21] R. Piestun, Y. Y. Schechner, and J. Shamir, *Propagation-invariant wave fields with finite energy*, *Journal of the Optical Society of America A* **17**, 294 (2000).
- [22] G. Grover and R. Piestun, *New approach to double-helix point spread function design for 3d super-resolution microscopy*, *Proc. of SPIE* **8590**, 85900M (2013).
- [23] K. Itoh, *Analysis of the phase unwrapping algorithm*, *Applied Optics* **21**, 2470 (1982).
- [24] D. Baddeley, M. B. Cannell, and C. Soeller, *Three-dimensional sub-100 nm super-resolution imaging of biological samples using a phase ramp in the objective pupil*, *Nano Research* **4**, 589 (2011).
- [25] A. N. Simonov and M. C. Rombach, *Passive ranging and three-dimensional imaging through chiral phase coding*, *Optics Letters* **36**, 115 (2011).

- [26] M. Born and E. Wolf, *Principles of optics: Electromagnetic theory of propagation, interference and diffraction of light / by Max Born and Emil Wolf with contributions by A.B. Bhatia ... [et al.]*, 6th ed. (Pergamon, Oxford, 1980).
- [27] V. N. Mahajan, *Line of sight of an aberrated optical system*, *Journal of the Optical Society of America A* **2**, 833 (1985).
- [28] H.-C. Eckstein, U. D. Zeitner, R. Leitel, M. Stumpf, P. Schleicher, A. Bräuer, and A. Tünnermann, *High dynamic grayscale lithography with an led-based micro-image stepper*, in *Optical Microlithography XXIX*, SPIE Proceedings, edited by A. Erdmann and J. Kye (SPIE, 2016) p. 97800T.
- [29] K.-H. Haas and H. Wolter, *Synthesis, properties and applications of inorganic-organic copolymers (ormocer®s)*, *Current Opinion in Solid State and Materials Science* **4**, 571 (1999).

5

IMAGE BASED ABERRATION RETRIEVAL USING HELICAL POINT SPREAD FUNCTIONS

A practical method for determining wavefront aberrations in optical systems based on the acquisition of an extended, unknown object is presented. The approach utilizes a conventional phase diversity approach in combination with a pupil-engineered, helical point spread function (PSF) to discriminate the aberrated PSF from the object features. The analysis of the image's power cepstrum enables an efficient retrieval of the aberration coefficients by solving a simple linear system of equations. An extensive Monte-Carlo simulation is performed to demonstrate that the approach makes it possible to measure low order Zernike modes including defocus, primary astigmatism, coma and trefoil. The presented approach is tested experimentally by retrieving the two-dimensional aberration distribution of a test setup by imaging an extended, unknown scene.

5.1. INTRODUCTION

Optical aberrations limit the performance of imaging and illumination systems in terms of resolution and signal-to-noise ratio. Even well optimized and tolerated optical designs may still be subject to severe aberrations when put into practice. Depending on the particular application scenario, this is due to external effects such as mechanically or thermally induced deformations, atmospheric turbulence or residual misalignment (i.e. for segmented mirrors) and manufacturing tolerances. These effects can be mitigated by means of adaptive optics or dedicated image post processing, which generally require detailed knowledge of the aberrations and ultimately the wavefront. The most common concepts for measuring the wavefront utilize interferometers or Shack-Hartman sensors. An alternative approach with a lower hardware complexity relies on the direct analysis of the effect of the aberrations on the point spread function (PSF) of the system. Existing methods are mainly based on iterative Fourier transform or maximum-likelihood estimation methods that determine the wavefront phase from a single PSF image or a through-focus PSF stack [2–5]. The estimation can be performed with high numerical efficiency in the approximation of small aberrations and low-NA optical systems using a linear system approach [6–9]. Machine learning offers alternative approaches that have gained increased interest in recent years. Using proper training sets and artificial neural networks it has been shown that aberrations can be retrieved from image intensity measurements [10–14]. Yet, most of the proposed intensity based methods are only applicable to point sources [4–13] and only a few consider simplified objects such as a sphere or single letters [14]. Moreover, they only provide the aberration information for a single dedicated field point.

Such distinct objects, however, are not always available in applications such as surveillance, microscopy or earth observation. Also, the respective optical systems feature an extended field of view with field dependent aberrations. In order to estimate the (field dependent) aberrations for an unknown scene, the object features need to be separated from the PSF, which provides the information on the aberration. One widely studied method to accomplish this is phase diversity (PD) [15, 16], which is based on a maximum-likelihood estimation [15–18], image contrast optimization [19] or other metrics [20, 21]. It has been applied for the co-phasing of segmented mirrors [20, 22] or high resolution coronagraphic imaging [23]. In general, the PD methods that consider an extended object scene necessitate numerically expensive, iterative optimization procedures that prohibit real time (snapshot) measurements. Moreover, they require a priori assumptions on object spectrum, as well as a careful choice of optimization parameters and regularization measures [18], which significantly influence their performance. A modified PD method is based on the analysis of the change of the image intensity distribution introduced by an adaptive optical component [24, 25]. The approach requires little a priori knowledge of the object but necessitates specialized adaptive-optical hardware and multiple, iterative image acquisition steps. A linear aberration retrieval model that eliminates the need for an iterative optimization in the case of an extended object has been proposed by Mocœur et al. [26]. However, the applicability of this method in practice is not demonstrated, since the authors neither provide a general numerical demonstration of the method for multiple sets of objects and aberrations, nor perform an experimental proof-of-concept. A recently proposed, non-iterative aberration

retrieval method for extended scenes utilizes a combination of PD and deep learning [27]. Yet, the approach can only be applied if image noise is negligible as otherwise the incorporated image processing routine becomes numerically unstable. Additionally, the approach has been demonstrated experimentally for simplified extended objects, i.e. single numbers, only.

In this paper, we introduce a novel approach which extends the conventional phase diversity concept using helical PSFs, which are used for three-dimensional localization and imaging [28–30]. These PSFs typically consist of a number of well identifiable sub-peaks that rotate around the focal point as a function of defocus. In [31], it is shown that aberrations distort the PSF sub-peak positions and ultimately influence their rotation angle. Therefore, they deteriorate the depth measurement accuracy of such pupil engineered (PE) systems. In contrast to previous work, this dependency is actually exploited in the approach presented here in order to retrieve information on the aberrations that are present.

At first, the general concept of pupil engineered phase diversity (PEPD) using helical PSFs is introduced. A linear model is derived, which enables the direct retrieval of aberrations without the need for iterative optimization or blind deconvolution. Then, a numerical assessment is conducted for an exemplary PEPD system, which quantifies the performance of the proposed method considering low order aberrations for unknown, natural objects. In particular, we analyse theoretical precision limits provided by the Cramér-Rao Lower Bound (CRLB) as well as the aberration retrieval success rate, which represents a suitable figure of merit for practical imaging applications. Finally, an experimental proof of concept is demonstrated by measuring low order aberration coefficients for a misaligned optical system considering a point source as well as an extended object.

5.2. PUPIL ENGINEERED PHASE DIVERSITY

The general phase diversity concept for measuring an aberrated wavefront is based on capturing a number of M images of the same object distribution $o(\mathbf{x})$. Each of these images $i_m(\mathbf{x})$ is obtained by introducing a known phase distribution $\phi_{d,m}(\mathbf{u})$, referred to as *phase diversity*. Here, \mathbf{x} and \mathbf{u} denote the image plane and pupil plane coordinates, respectively. The imaging process for each configuration m , referred to as channels, can be described by the following convolution:

$$i_m(\mathbf{x}) = \underbrace{K_m o_{\text{norm}}(\mathbf{x}) * h_m(\mathbf{x})}_{\tilde{i}_m(\mathbf{x})} + v_m(\mathbf{x}) \quad , \quad (5.1)$$

where $o_{\text{norm}}(\mathbf{x})$ is the normalized object distribution and $\tilde{i}_m(\mathbf{x})$ is the signal of the m th channel in the absence of noise. The number of photons per channel is denoted by K_m , the image noise is described by $v_m(\mathbf{x})$ and $h_m(\mathbf{x})$ is the point-spread function. The latter is obtained by taking the absolute square of the Fourier transformation of the pupil function $g_m(\mathbf{u})$ according to:

$$\begin{aligned} h_m(\mathbf{x}) &= |\mathcal{F}[g_m(\mathbf{u})]|^2 \\ &= |\mathcal{F}[A(\mathbf{u}) \exp[i(\phi_m(\mathbf{u}))]]|^2 \quad , \end{aligned} \quad (5.2)$$

i.e. we assume incoherent imaging conditions. The amplitude function $A(\mathbf{u})$ corresponds to a circular transmission window and is assumed to be equal for all channels. The pupil phase $\phi_m(\mathbf{u})$ of each channel is a result of the superposition of the wavefront aberration ϕ_a and the introduced diversity $\phi_{d,m}$. In accordance with the conventional PD approach, both contributions are decomposed into Zernike modes Z_n according to:

$$\begin{aligned}\phi_m(\mathbf{u}) &= \phi_a(\mathbf{u}) + \phi_{d,m}(\mathbf{u}) \\ &= \sum_n (\alpha_n + \Delta_{n,m}) Z_n(\mathbf{u}) ,\end{aligned}\quad (5.3)$$

where n labels the different contributing Zernike modes. The aberration retrieval using the conventional PD method then corresponds to retrieving the coefficients α_n , which are equal for all channels m , by introducing known diversity coefficients $\Delta_{n,m}$. The first 3 Zernike modes (piston, tip and tilt) are excluded, as they cannot be accessed directly using PD which is a common limitation of the technique. In order to retrieve higher order coefficients, multiple estimation approaches based on maximum-likelihood estimation [15, 17], image contrast optimization [19] or alternative metrics [20, 21] have been introduced and applied. All of these require iterative optimization procedures that prohibit fast, real-time measurements (e.g. in a closed-loop) for high-resolution images with a sampling on the order of megapixels.

We propose the use of pupil engineering to overcome these restrictions of conventional phase diversity. To this end, an additional phase term $\phi_{PE}(\mathbf{u})$ is added to Eq. (5.3) and the pupil phase $\phi_m(\mathbf{u})$ of the m th channel is then given by:

$$\phi_m(\mathbf{u}) = \sum_n (\alpha_n + \Delta_{n,m}) Z_{n,m}(\mathbf{u}) + \phi_{PE}(\mathbf{u}) \quad (5.4)$$

The PE term $\phi_{PE}(\mathbf{u})$ is assumed to be equal for all channels. It can thus be realized using a single phase element, which simplifies the practical implementation and eliminates systematic errors due to different tolerances of the elements. The most common diversity implementation, which is also assumed for the PEPD method proposed here, incorporates a known defocus aberration Δ_4 between $M = 2$ different imaging configurations. The choice of this configuration is primarily motivated by practical considerations, as this can be realized relatively easily by a sequential shift of the image distance or by using a beam splitting configuration, which allows for capturing the two images at the same time. The PEPD configuration is shown schematically in the top part of Fig. 5.1.

Here, the goal of the additional phase term ϕ_{PE} in Eq. (5.4) is to eliminate the need for iterative retrieval methods by generating a PSF that makes a decoupling of object and aberration (PSF) information possible. This can be achieved using phase elements (i.e. computer generated holograms (CGHs)), which lead to helical PSFs that rotate through defocus, because of two unique characteristics of such a PSF. First, helical PSFs provide a distinct shape distortion in the presence of low order aberrations that can be retrieved even in the case of an extended object. In conventional PD, the required image diversity is introduced by an aberration dependent blurring of the PSF, which depends on the defocus coefficient $\Delta_{4,m}$. In general, the complex relationship between this blur and the aberrated pupil phase $\phi_m(\mathbf{u})$ necessitates the use of iterative blind deconvolution methods for an extended, unknown object distribution. In contrast, helical PSFs exhibit distinct shifts of the PSF peaks as described in [31] depending on the particular aberration

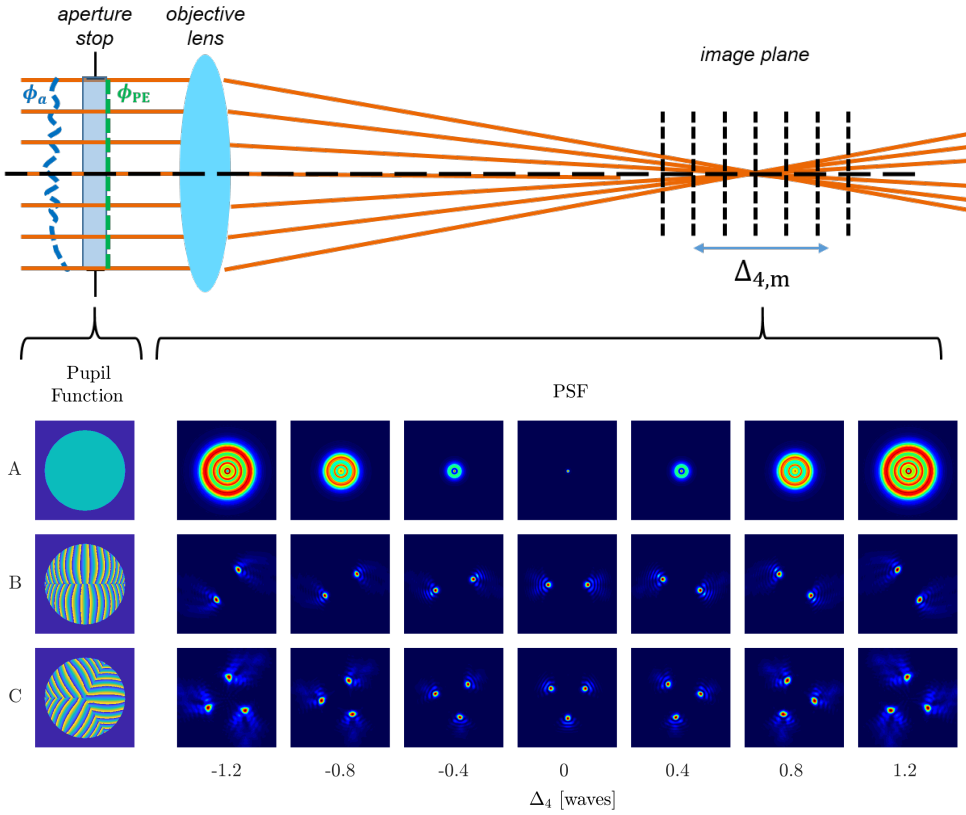


Figure 5.1: Top: Schematic setup overview of the proposed PEPD approach for aberration retrieval. Bottom: PSF dependency on the defocus diversities Δ_4 for different pupil phase functions that generate (A) a nominal PSF (B) a double- and (C) a triple-helix PSF

coefficient α_n and the defocus diversity $\Delta_{4,m}$. These shifts are encoded in the acquired images $i_m(\mathbf{x})$ of the extended object and can be retrieved using the cepstrum approach presented in [32]. The second unique characteristic of helical PSFs is illustrated in the bottom part of Fig. 5.1 for two particular examples of a double- and a triple-helix PSF. The PSFs provide an inherent peak rotation for different amounts of defocus diversities $\Delta_{4,m}$ while preserving the confined shape of the individual peaks. This feature can be utilized to diversify the PSF response to individual aberration coefficients α_n and to eliminate ambiguities by acquiring two images with different diversities $\Delta_{4,m}$. All things considered, these two properties enable a unique retrieval of aberration coefficients α_n by measuring peak shifts for two defocus diversities. The idea of using helical PSFs for aberration retrieval based on a through focus measurement has been previously applied in [33]. The practicality of that approach is limited since it requires the acquisition of three subsequent image stacks ($M > 30$) and it is only applicable to point objects.

5.3. LINEAR ABERRATION RETRIEVAL MODEL

The aberration retrieval is based on exploiting the effect of different aberrations on the PSF shape. Aberrations generally lead to a spreading of a conventional PSF. It turns out, however, that low order aberrations lead to a shift of the individual peaks in the case of a helical PSF [31]. In particular, defocus, astigmatism and spherical aberration lead to an overall rotation of a double-helix PSF. In contrast to previous work, which only analyzed the aberration effect on the overall PSF rotation angle, the individual location $(x_j^{\text{PSF}}, y_j^{\text{PSF}})$ of each PSF peak is now considered.

In the PEPD approach described in the previous section, the PSF $h_m(\mathbf{x})$ is not directly accessible from the measured image irradiance $i_m(\mathbf{x})$, in case an unknown, extended object is considered. However, the approach described in [32] can be utilized to obtain the helical PSF peak locations $(x_j^{\text{PSF}}, y_j^{\text{PSF}})$. It is based on retrieving the location (x_j^c, y_j^c) of peaks in the power cepstrum distribution of the acquired, pupil engineered image. These peaks can be associated with the helical PSF peak positions, if the object contains small spatial features with a size that is comparable to or smaller than the helical PSF (projected in object space) as elaborated in ref. [32]. Under this condition, the aberration retrieval method proposed here is based on analyzing the change of the power cepstrum's peak positions due to aberrations. In general, a larger number J of PSF peaks results in a larger number of degrees of freedom. Yet, the larger the peak number J , the more complex the cepstrum analysis, which contains $J(J-1)/2$ peaks to be identified. Further, a larger value for J results in a smaller maximum range of aberration coefficients that can be retrieved without ambiguities. Only triple-helix PSFs are therefore considered here, which provide a practical compromise between the maximization of the number of degrees of freedom and robust cepstrum peak identification.

In the following, the influence of the first 8 Zernike aberrations (excluding piston, tip and tilt) on the cepstrum peak positions (x_j^c, y_j^c) with $j = [1, 2, 3]$ is assessed. These aberrations are defocus (Z_4), primary astigmatism (Z_5, Z_6), coma (Z_7, Z_8), trefoil (Z_9, Z_{10}) and spherical aberration (Z_{11}). The cepstrum distribution of the aberrated PSF is calculated for each individual aberration coefficients in a range of $\alpha_n = [-0.16, 0.16]$ waves rms. The peak positions are extracted by processing the cepstrum distribution and performing a Gaussian peak fit as described in [32]. The dependencies of the position changes $(\delta x_j^c, \delta y_j^c)$ are exemplarily plotted in Fig. 5.2 for an in-focus diversity channel ($\Delta_4 = 0$ waves). The same set of parameters describing the optical system will be used throughout the theoretical and numerical investigations in this paper.

It can be seen that the aberration coefficients α_n lead to a close to linear change of the PSF parameters for the coefficient range of approximately $\alpha_n = [-0.1, 0.1]$. Hence, the PEPD approach is described by a linear system model and the effect of an aberration vector α on the PSF peak locations $(\mathbf{x}^c, \mathbf{y}^c)_m$ of a particular channel m is approximated by a linear transfer matrix $\hat{\mathbf{T}}_m$ according to:

$$\begin{aligned} \begin{pmatrix} \mathbf{x}^c(\alpha) \\ \mathbf{y}^c(\alpha) \end{pmatrix}_m &= \begin{pmatrix} \mathbf{x}^c \\ \mathbf{y}^c \end{pmatrix}_{m,0} + \begin{pmatrix} \delta \mathbf{x}^c(\alpha) \\ \delta \mathbf{y}^c(\alpha) \end{pmatrix}_m \\ &= \begin{pmatrix} \mathbf{x}^c \\ \mathbf{y}^c \end{pmatrix}_{m,0} + \hat{\mathbf{T}}_m \cdot \alpha, \end{aligned} \quad (5.5)$$

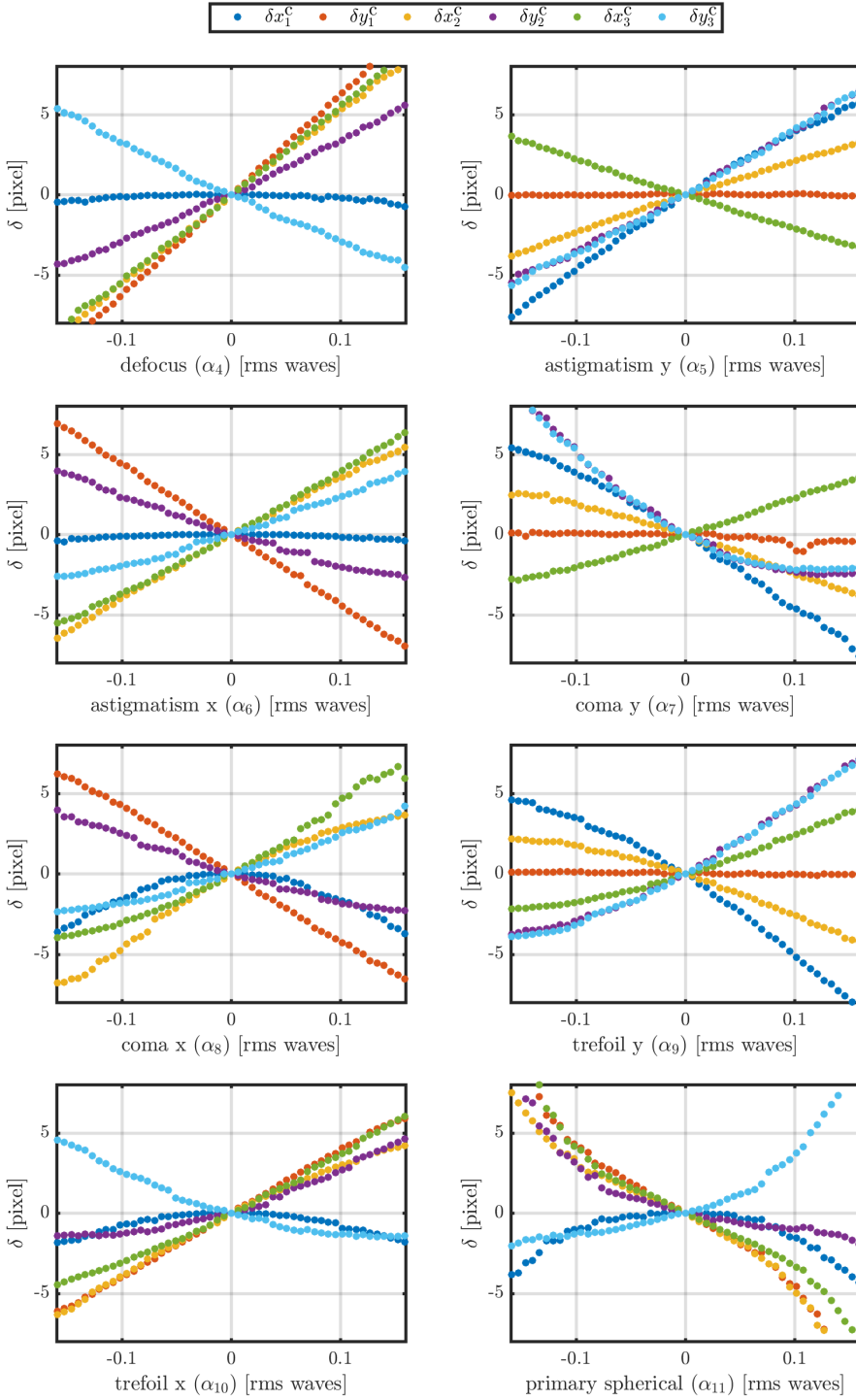
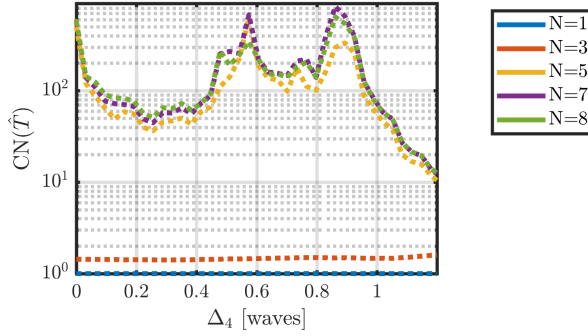


Figure 5.2: Dependency of cepstrum peak location shift ($\delta x_j^c, \delta y_j^c$) on the coefficients α_n of low order Zernike aberrations ($N \leq 8$), excluding piston, tip and tilt.

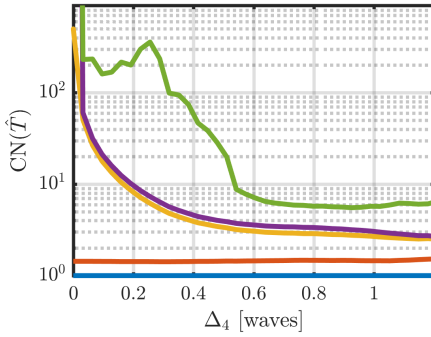
where $(\mathbf{x}^c, \mathbf{y}^c)_{m,0}$ denotes the nominal cepstrum peak location in case no aberrations are present. Note that the size of the transfer matrix \hat{T}_m is $6 \times N$, where N is the number of Zernike modes to be retrieved. The determination of the linear model parameters, which include the nominal cepstrum vector $(\mathbf{x}^c, \mathbf{y}^c)_{m,0}$ as well as the elements of the transfer matrix \hat{T}_m , can be understood as a necessary calibration procedure for the PEPD system. These parameters could be obtained experimentally by introducing a set of known aberrations to the system. Although this approach provides a high robustness with respect to intrinsic tolerances of a real system, such a pre-defined set is not always accessible. An alternative approach is based on using a theoretical model of the optical system design and performing purely numerical simulations of the aberration influence as performed in Fig. 5.2. To this end, the nominal peak vectors as well as the transfer matrix can be obtained by fitting linear functions to the simulated dependencies $(x_j^c(\alpha), y_j^c(\alpha)_m)$ for each peak i and channel m . We consider a particular aberration coefficient fit range of approximately $\alpha_n = [-0.1, 0.1]$ waves rms, where a close to linear dependency is maintained for all Zernike modes under consideration. As can be seen in Fig. 5.2, the deviation from this linear approximation is significantly increased for larger coefficients, i.e. for spherical aberration, coma and trefoil, which results in a reduced accuracy of the linear aberration retrieval model.

An aberration vector α can now be estimated based on only two calculation steps using the linear model described by Eq. (5.5). First, the PSF peak locations $(\mathbf{x}^c(\alpha), \mathbf{y}^c(\alpha))_m$ are calculated for the measured images $i_m(\mathbf{x})$ using the cepstrum approach described in [32]. Second, the linear system in Eq. (5.5) is solved by taking the pseudo-inverse of the transfer matrix \hat{T} . This direct approach enables fast aberration retrieval even for high resolution images. The obtained solution may be subject to a large estimation error though, if the linear system is not well conditioned. The condition number provides a measure to compare the relative estimation errors for different PEPD scenarios and to assess under what condition an aberration vector α cannot be retrieved reliably. Figure 5.3 (a) shows the dependency of the condition number $\text{CN}(\hat{T}_m)$ on the defocus diversity Δ_4 for a single channel PEPD aberration retrieval of up to N Zernike modes. Note that only positive values of Δ_4 are plotted in view of the symmetry of $\text{CN}(\hat{T}_m)$. The dependency is only analyzed for defocus diversities up to $\Delta_4 = 1.2$ waves. Larger defocus values lead to significant spreading of the triple-helix PSE, which prevents a reliable cepstrum peak identification. The graphs in Fig. 5.3 (a) show that a low condition number is only provided for the retrieval of up to 3 modes throughout the entire defocus diversity range of interest. In other words, only defocus and astigmatism can be reliably retrieved using the proposed PEPD approach based on a single measurement. In fact, the depth retrieval approach described in [32] represents the particular case of retrieving the defocus aberration only, where other aberrations are considered negligible.

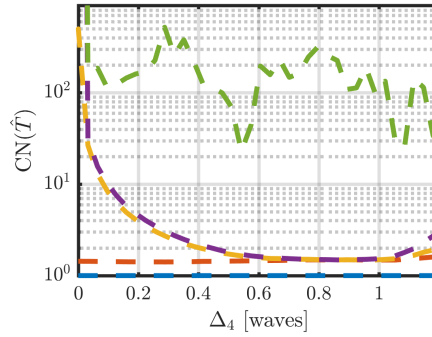
In order to retrieve more than 3 Zernike orders, at least two channels need to be considered because with a single channel there are not enough degrees of freedom in the linear PSF peak shift model and the solution becomes ambiguous. This is analogous to the conventional PD approach. To this end, the linear model in Eq. (5.5) is extended by simply combining the rows of the measured peak positions $(\mathbf{x}^c(\alpha), \mathbf{y}^c(\alpha))_m$, the nominal peak positions $(\mathbf{x}^c, \mathbf{y}^c)_{m,0}$ and the transfer matrix \hat{T}_m . Figure 5.3 shows the dependency of the condition number of the extended transfer matrix for two commonly investigated, two



(a) Single channel



(b) Two asymmetric channels



(c) Two symmetric channels

Figure 5.3: Dependency of the condition number $\text{CN}(\hat{T})$ on the defocus diversity Δ_4 for retrieving up to N Zernike modes and considering different PD configurations.

channel PD configurations ($M = 2$). The asymmetric configuration (Fig. 5.3 (b)) utilizes one channel in focus and one channel that is defocused by the amount Δ_4 . Conversely, the symmetrical approach (Fig. 5.3 (c)) is based on two image planes around the nominal focus location, which are subject to a defocus diversity of $\pm\Delta_4$, respectively. Both configurations result in significantly reduced condition numbers for $N = [5, 7]$ compared to the single channel configuration. The symmetrical configuration provides the lowest, overall condition number of $\text{CN}(\hat{T}) = 1.4$ at $\Delta_4 = 0.8$ waves for the retrieval of up to $N = 7$ modes and the defocus range of interest. A reduced condition number for $N = 8$ modes, which includes spherical aberration, can only be obtained using the asymmetrical configuration and defocus diversities $\Delta_4 > 0.5$ waves. Yet, the corresponding minimum achievable condition number of $\text{CN}(\hat{T}) = 5.5$ already indicates that the retrieval using the proposed PEPD approach is subject to considerable estimation errors in that case.

5.4. NUMERICAL PERFORMANCE ASSESSMENT

5.4.1. MONTE CARLO ANALYSIS

The following numerical investigations are based on the optical layout shown in Fig. 5.1. The optical design parameters are selected based on the experimental demonstration system that is used in section 5.5. The optical system is characterized by an aperture stop diameter of 10 mm, which is located in front of a focusing lens with a focal length of 150 mm. A wavelength of 540 nm is considered and the object is assumed to be located 1.8 m in front of the aperture stop, which results in an image space F-number of 15.9. The applied pixel size of 3.45 μm ensures a proper sampling with a Nyquist sampling frequency of 145 lp/mm above the optical cut-off frequency of $\rho_{\text{cut-off}} = 117 \text{ lp/mm}$. The triple-helix PSF phase element shown in Fig. 5.1 is used as a baseline for the PEPD approach evaluation. In addition, a double-helix PSF is considered for comparison purposes. The particular designs of both phase elements are equal to the designs used in [31]. Figure 5.1 shows the dependency of the conventional as well as the pupil engineered PSFs on the defocus diversity Δ_4 . Note that a geometrical image shift of 1 mm approximately corresponds to an RMS defocus value of $\Delta_4 = 0.27$ waves.

In addition to the image noise $v_m(\mathbf{x})$, the precision of the PD aberration retrieval strongly depends on the specific PD settings including the amount of defocus diversity Δ_4 , the particular aberrations to be estimated α , as well as the observed object distribution $o(\mathbf{x})$. Accordingly, a numerical Monte Carlo type analysis is performed in order to compare different PD settings and to assess general performance limits of the proposed PEPD method. So far, numerical studies in this area either assumed solely additive Gaussian noise [34–36] (i.e. camera readout noise) or pure Poisson noise [35] (photon shot-noise). Furthermore, only idealized point sources or a single, dedicated object [34–38] were investigated. This stands in contrast to the PEPD approach presented in this paper, where the main motivation is to apply aberration retrieval in the context of imaging arbitrary extended objects. Therefore, the Monte Carlo analysis in [34] is extended and performed for a statistical ensemble that comprises a combination of Gaussian and Poisson noise considering different sets of aberrations as well as different object distributions.

In general, 5 sets of aberrations are considered, which comprise a combination of N different Zernike modes with a maximum mode number $N = [1, 3, 5, 7, 8]$, excluding piston, tip and tilt. Each consecutive set includes an additional Zernike mode starting with pure defocus (Z_4) followed by primary astigmatism (Z_5, Z_6), coma (Z_7, Z_8), trefoil (Z_9, Z_{10}) and spherical aberration (Z_{11}). Each set contains 500 randomly generated aberration vectors α . The coefficients α_n ($n = 1, 2, \dots, N$) of the individual aberration vectors α are based on uniformly distributed random variables, which are normalized to result in a pre-defined pupil-averaged rms phase error $\alpha_{\text{total}} = \sqrt{\sum_{n=1}^N \alpha_n^2}$.

The set of considered object distributions is extracted from the ImageNet library [39], which is widely used as an image resource in the area of machine learning and object recognition. The library provides an extensive variety of natural object distributions, which can be considered as representative examples for the aberration measurement scenario addressed here. We extract a subset of 500 random images of the latest library addition, which contains the newest 5500 images of the overall image library. These images are further processed before they are applied for the Monte Carlo analysis. Initially,

each of the 8bit RGB images is converted to a grayscale format. The resulting images are subsequently cropped to fit a square format and rescaled using a linear interpolation to provide a common resolution of 512 x 512 pixels.

All calculations consider a combination of idealized (Gaussian) camera readout noise, which is determined by an rms value σ_r , and photon shot-noise, which depends on the number of photons K_m per channel. A fixed rms readout noise $\sigma_r = 10$ photons per pixel is assumed for all simulations. The number of photons K_m is selected by a pre-defined image signal-to-noise ratio (SNR). For an extended scene sampled by $P \times P$ pixels, the SNR is defined as the ratio between the average signal and the standard deviation of the signal. It can be expressed for the idealized case of a uniform (white) object distribution by:

$$\text{SNR} = \frac{K_m / P^2}{\sqrt{K_m / P^2 + \sigma_r^2}} . \quad (5.6)$$

The following numerical investigations analyze two different figures of merit for the Monte Carlo performance evaluation. First, the Cramér-Rao lower bound (CRLB) performance is analyzed, which is commonly used in order to quantify and compare the highest-achievable precision limit. Second, the aberration retrieval success rate is investigated as an alternative, practical figure of merit.

5.4.2. CRLB PERFORMANCE

The analysis of Fisher information and the CRLB has been previously applied in the context of phase diversity for optimizing the amount of defocus diversity [34, 36, 38] or for comparing different diversity modes [35]. It provides the precision limit of the phase retrieval in the presence of image noise in terms of a statistical process. The CRLB with respect to PD aberration measurement has, so far, only been investigated for objects that are known a priori [34–36, 38]. In contrast, the aberration estimation problem for an unknown object is comparable to a blind deconvolution problem.

The Fisher matrix for a multi-channel, blind deconvolution problem has been derived in the context of orientation estimation for imaged space objects [40]. It can be expressed as:

$$[\text{F}(\beta)]_{kl} = \sum_m \sum_{\mathbf{x}} \frac{1}{\tilde{i}(\mathbf{x}) + \sigma_r^2} \frac{\partial \tilde{i}_m(\mathbf{x})}{\partial \beta_k} \frac{\partial \tilde{i}_m(\mathbf{x})}{\partial \beta_l} , \quad (5.7)$$

considering the PD imaging system described in section 5.2. Here, β is the set of unknown system parameters and σ_r is the rms value of the additive Gaussian noise. The parameters β_k can be divided into 2 subsets for the general PD wavefront measurement with an unknown object described here. The first subset consists of the previously introduced Zernike aberration coefficients α_n ($n = 1, 2, \dots, N$). The second subset is dedicated to the object distribution described by a set of adequate basis functions. Although the object distribution itself shall not be estimated in the frame of this work, it is nevertheless important to take these parameters into consideration, which can be referred to as *nuisance parameters*. They need to be estimated jointly with the actual parameters of interest (explicitly or implicitly), if no a priori information on the object is available [40–42], which we will assume in the following. In this case, we will show that CRLB performance of the aberration estimation is significantly degraded due to the unknown object.

One particular set of basis functions to describe the object distribution, which has been used to assess the CRLB for blind deconvolution problems [43], is provided by delta distributions that simply correspond to the discrete sampling locations x_k of the object. However, this basis results in very large Fisher matrices with a total size of $(P^2 + N)^2$ elements. Considering the resolution of 512x512 pixels of the image set used here and 7 Zernike aberration modes to be retrieved, a double precision matrix would have a size of 512 GB, which cannot be efficiently handled numerically. In order to reduce the numerical complexity, a transition into the Fourier domain is performed and a general property of natural objects is exploited. In particular, their power spectral density is significantly decreasing with higher spatial frequencies and most of the object information is contained in a low spatial frequency sub-region of the spectrum. Accordingly, it is sufficient to only consider low spatial frequency coefficients Ω_k of the object spectrum to obtain an adequate approximation of the CRLB. The coefficients Ω_k are comprised of a real part Ω_k^{\Re} and an imaginary part Ω_k^{\Im} , since the Fourier transform $\Omega = \mathcal{F}(o)$ of the object distribution is complex valued. Yet, only half of the Fourier coefficients are considered, because the real valued object distribution o implies that its Fourier transform Ω is Hermitian.

On the one hand, the partial derivatives of $\tilde{i}(\mathbf{x})$ with respect to the aberration coefficients α_n for a particular PD channel m is derived in [34] and given by:

$$\frac{\partial \tilde{i}_m(\mathbf{x})}{\partial \alpha_n} = -2K_m o_{\text{norm}}(\mathbf{x}) * \left(\text{Im} \left\{ G_m^*(\mathbf{x}; \alpha + \Delta_m) \cdot \mathcal{F} \left[g_m(\mathbf{u}; \alpha + \Delta_m) Z_n \right] \right\} \right). \quad (5.8)$$

Note that G_m^* denotes the complex conjugate of the Fourier transform of the pupil function $g_m(\mathbf{u})$ as defined in Eq. (5.2). On the other hand, the partial derivatives with respect to the real part Ω_k^{\Re} of the objects Fourier coefficients can be obtained using Eq. (5.1):

$$\begin{aligned} \frac{\partial \tilde{i}_m(\mathbf{x})}{\partial \Omega_k^{\Re}} &= \frac{\partial}{\partial \Omega_k^{\Re}} [o(\mathbf{x}) * h_m(\mathbf{x})] \\ &= \frac{\partial}{\partial \Omega_k^{\Re}} [\mathcal{F}\{\Omega(\mathbf{u}) \cdot H_m(\mathbf{u})\}] \\ &= \frac{\partial}{\partial \Omega_k^{\Re}} \left[\mathcal{F} \left\{ \sum_l (\Omega_l \cdot H_{m,l} \cdot \delta(\mathbf{u} - \mathbf{u}_l)) \right\} \right], \end{aligned} \quad (5.9)$$

where the Fourier spectrum of $\Omega(\mathbf{u}) H_m(\mathbf{u})$ is decomposed into discrete sampling frequencies \mathbf{u}_l using the delta distribution $\delta(\mathbf{u})$. Next, the Hermitian symmetry of $\Omega(\mathbf{u})$ and $H_m(\mathbf{u})$ is exploited to derive the final expression of the derivative according to:

$$\begin{aligned} \frac{\partial \tilde{i}_m(\mathbf{x})}{\partial \Omega_k^{\Re}} &= \mathcal{F} \left\{ \left(H_{m,k} \cdot \delta(\mathbf{u} - \mathbf{u}_k) + H_{m,k}^* \cdot \delta(\mathbf{u} + \mathbf{u}_k) \right) \right\} \\ &= 2 \cdot \Re \left\{ H_{m,k} \cdot e^{2\pi i(\mathbf{u}_k \cdot \mathbf{x})} \right\}. \end{aligned} \quad (5.10)$$

The derivative with respect to the imaginary part Ω_k^{\Im} can be derived in an equivalent manner, which results in:

$$\frac{\partial \tilde{i}_m(\mathbf{x})}{\partial \Omega_k^{\Im}} = 2 \cdot \Im \left\{ H_{m,k} \cdot e^{2\pi i(\mathbf{u}_k \cdot \mathbf{x})} \right\}. \quad (5.11)$$

The Fisher matrix can now be calculated using Eq. (5.7) and considering the derivatives provided in Eq.(5.8), Eq.(5.10) and Eq.(5.11). The lower bounds ϵ_k of the mean square error of an unbiased estimate of the parameters $\beta = \{\alpha, \Omega^{\Re}, \Omega^{\Im}\}$ can be found in the diagonal element of the inverted Fisher matrix according to:

$$\epsilon_k^2 = \text{Var}(\beta_k) \geq [F^{-1}(\beta)]_{kk} . \quad (5.12)$$

The CRLB for the measurement of the entire set of N aberration coefficients $\{\alpha\}$ can then be obtained by the sum of the lower bounds $\sum_{k=1}^N \epsilon_k^2$ that correspond to the CRLBs of the N individual Zernike coefficients α_n . We emphasize again that the CRLB of the aberration estimation is affected by the object spectrum coefficients Ω_k , even if the object itself is not being retrieved. This is due to the inversion of the overall Fisher matrix F in Eq. (5.12), which, in general, contains non-zero, off-diagonal elements.

Accordingly, the CRLB for the aberration estimation depends on the particular object distribution $o(\mathbf{x})$ as well as the actual aberration coefficients α_k . In order to obtain a general figure of merit of the PEPD aberration measurement scenario, we follow the Monte-Carlo type approach presented in [34]. In particular, the CRLBs of an entire, previously defined set, which contains 500 different aberration vectors α and object distributions o , are averaged and the final CRLB performance measure is given by:

$$\epsilon^2 = \frac{1}{L} \sum_{l=1}^L \left[\sum_{k=1}^N \epsilon_{k,l}^2 \right] . \quad (5.13)$$

This approach can be considered as a suitable method to evaluate the mean-square error performance of the phase estimation for a particular statistical class of aberrations and objects.

The following calculations consider the PEPD system presented in section 5.4 for the symmetrical as well as the asymmetrical PD configuration. The analysis is performed for the previously defined set of object distributions and limited to one of the 5 aberration sets with $N = 7$ modes. It is shown in the next section that this represents the maximum number of modes that can be reliably estimated using the proposed linear retrieval model. An equal photon count of $K = 1.2 \cdot 10^8$ is assumed for each channel, which corresponds to a SNR of 20 for a uniform object according to Eq. (5.6). Furthermore, an overall rms aberration error of $\alpha_{\text{total}} = 0.2$ waves is applied. In addition to the engineered double- and triple-helix PSF designs shown in Fig. 5.1, the CRLB is investigated for a conventional PSF without a phase element.

Initially, the dependency of the CRLB performance measure ϵ^2 on the size of the considered low spatial frequency sub-region of the object is investigated for a single defocus diversity value of $\Delta_4 = 0.7$ waves. In particular, the radius ρ of the circular sub-region is varied with respect to the optical cut-off frequency $\rho_{\text{cut-off}} = 117 \text{ lp/mm}$. The corresponding plot is shown in Fig. 5.4 (a). It can be seen that the CRLB is significantly increasing if a non-zero spatial frequency sub-region is taken into consideration. This indicates that the aberration measurement accuracy for an unknown object is deteriorated in comparison to the case of a known object ($\rho = 0$). The CRLB performance of all considered phase diversity scenarios is converging for radii $\rho > 0.5 \cdot \rho_{\text{cut-off}}$. Accordingly, the subsequent simulations only consider Fourier coefficients Ω_k below this limit

to calculate the Fisher matrix, which is considered a suitable approximation of the CRLB performance in order to limit the numerical complexity. Figure 5.4 (b) and (c) show the dependency of the corresponding CRLB on the applied defocus diversity Δ_4 in comparison between a known ($\rho = 0$) and an unknown object ($\rho = 0.5 \cdot \rho_{\text{cut-off}}$), respectively. Note that only positive diversity values Δ_4 are plotted here, due to the symmetric CRLB performance, which arises from the uniformly distributed aberration coefficients.

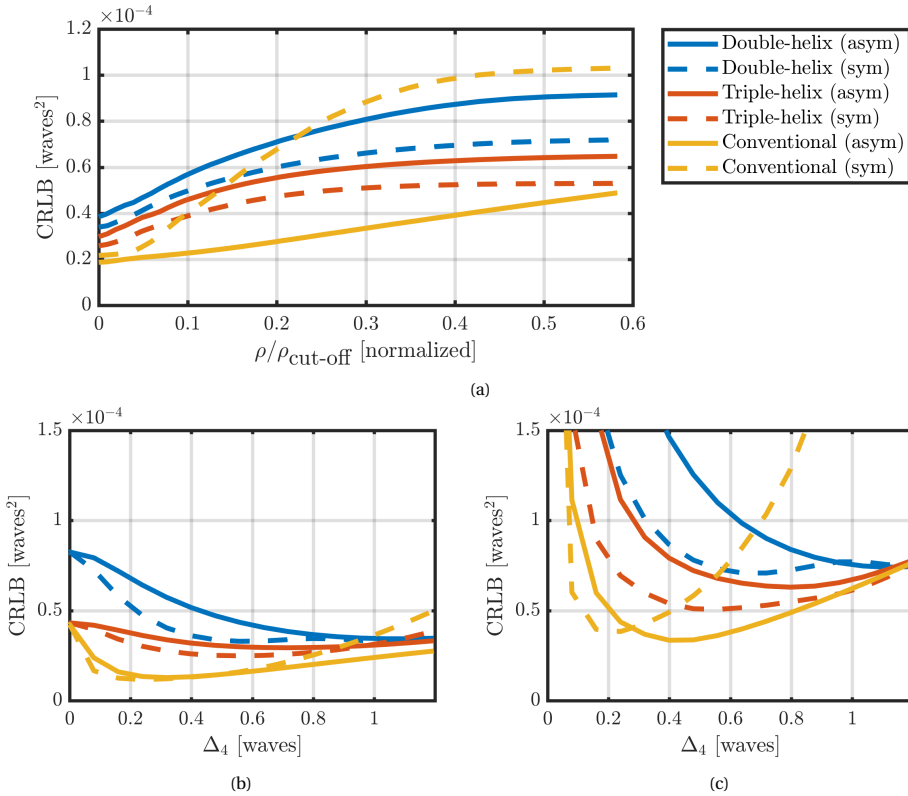


Figure 5.4: (a) CRLB dependency on the radius ρ of considered low spatial frequency sub-region of the object for different phase PD aberration retrieval scenarios ($\Delta_4 = 0.7$ waves). (b),(c) CRLB dependency on the selected defocus diversity Δ_4 for the same PD scenarios based on a known and an unknown object distribution, respectively, and considering a low spatial frequency region with $\rho = 0.5 \cdot \rho_{\text{cut-off}}$.

The CRLB analysis for a known object distribution in Figure 5.4 (b) reveals that the conventional PSF provides a superior performance with respect to the lowest achievable CRLB. The minimum CRLB is approximately a factor of 2 better than for the triple-helix and a factor of 2.5 better than the double-helix configuration. Note that the symmetrical configuration provides a better minimum CRLB value for all considered pupil functions, which is in agreement with previous results in the literature for the case of a nominal PSF [34]. The results for an unknown object in Figure 5.4 (c) demonstrate that the CRLB is increased over the entire diversity range in comparison with the case of a known ob-

ject. Yet, the conventional PSF still provides a superior CRLB performance compared to the helical PSFs. Both cases demonstrate the existence of an optimum diversity value Δ_4 that provides a minimum CRLB performance. It is pointed out that this optimum is shifted towards larger diversity values for the pupil engineered PD systems.

In summary, the conventional motivation for using helical PSFs is based on an improved CRLB for defocus measurements [30, 44, 45]. However, the performed simulations indicate that engineered PSFs are inferior, in case an entire set, i.e. $N = 7$, of aberrations is measured for an extended scene. We note that other authors claim to have found pupil engineered PSF designs with a superior performance [46, 47] in comparison with the conventional PSF. However, the results of the corresponding analyses are limited. First, the simulations in [46, 47] only consider idealized point sources. On the other hand, the calculation is only performed for a single, non-optimized diversity value Δ_4 . As can be seen from the simulation in Fig. 5.4, the proper choice of this parameter is crucial when comparing different PD approaches.

5.4.3. ABERRATION RETRIEVAL PERFORMANCE

The previously performed CRLB investigation aims at determining the precision limit of the measurement in the presence of noise. In a practical adaptive optics or system integration/alignment application scenario, however, it is rather important if the wavefront is correctly measured up to a certain accuracy limit. A suitable limit for classical imaging systems is given by the diffraction limit, which is commonly defined by a residual rms wavefront aberration of $\lambda/(8\sqrt{3})$. Therefore, the aberration retrieval success rate (SR) is considered for the following performance investigation. It is defined as the relative number of samples of a particular set of aberrations and object distributions with an rms measurement error (deviation between the retrieved and the actual wavefront) below the diffraction limit. Accordingly, it can be interpreted as the probability for a successful aberration retrieval in a practical application scenario, such as co-phasing a segmented optical mirror [20, 22].

In order to calculate the success rate, the PEPD approach proposed in section 5.3 is applied for the previously defined statistical sets of aberration vectors and object distributions. Initially, an equal overall wavefront error of $\alpha_{\text{total}} = 0.2$ waves and photon count $K = 1.2 \cdot 10^8$ compared to the CRLB analysis is considered. The results of the Monte Carlo simulations are shown in Fig. 5.5 (a). The dependency of obtained success rate on the defocus diversity Δ_4 is shown for the 5 different aberration sets and in comparison between the symmetrical and the asymmetrical PEPD configuration. The graphs show that the retrieval of up to 3 Zernike modes (defocus+astigmatism) provides a success rate close to 100% in both scenarios and throughout almost the entire defocus diversity range under investigation. Note that a similar performance can be obtained using a single channel only. The high success rate validates that the cepstrum approach can be used to retrieve the PSF parameters from the acquired images, which confirms that the considered natural objects provide a sufficient amount of small spatial features.

The success rate drops for a retrieval of up to 7 modes and features distinct optimum diversity values of approximately $\Delta_4 = 0.7$ waves for both scenarios. The appearance of this optimum can be related to the trade-off between the optimum CRLB (Fig. 5.4 (b)) and the condition number assessment (Fig. 5.3 (b) and (c)). The symmetrical configuration

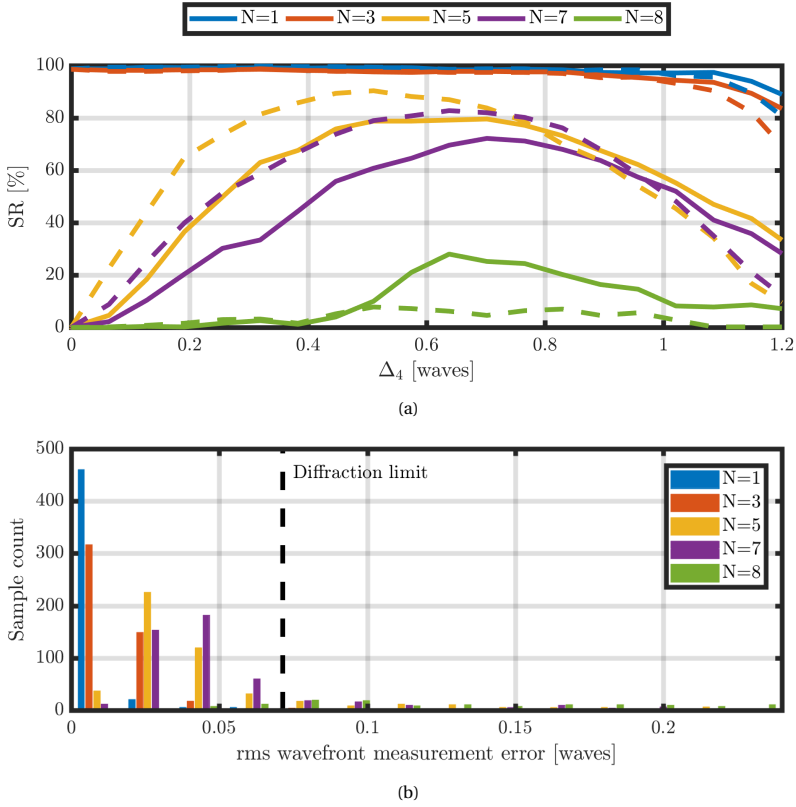


Figure 5.5: (a) Dependency of the success rate (SR) on the defocus diversity Δ_4 for the 5 different aberration sets and in comparison between the asymmetrical (solid line) and the symmetrical (dashed line) PEPD configuration. (b) Histogram plot illustrating the number of samples of each aberration set that provide a certain rms measurement error for the particular case of a symmetric configuration and $\Delta_4 = 0.7$ waves. An overall wavefront error of $\alpha_{\text{total}} = 0.2$ waves and a photon count $K_m = 1.2 \cdot 10^8$ is considered.

provides a superior performance with a success rate of up to $\text{SR} = 84\%$ ($N = 7$), which is in line with the significantly lower condition number compared to the asymmetrical case. The success rate deteriorates significantly if spherical aberration is included for the aberration retrieval ($N = 8$). Although, the asymmetrical configuration provides a better performance, the maximum success rate is only $\text{SR} = 30\%$. The histogram in Fig. 5.5 (b) illustrates how many samples of each set provide a certain rms measurement error for the particular case of a symmetric configuration at $\Delta_4 = 0.65$ waves. The plot indicates that the mean as well as the variance of this error increase with higher maximum mode numbers N . The large spreading for $N = 8$ modes (included spherical aberration) demonstrates that the relatively high condition number (Fig. 5.3 (b)) in addition to increased deviation of spherical aberration (Z_{11}) from a linear PSF response (Fig. 5.2) do not permit a reliable retrieval of that particular mode.

Additional simulations are performed in order to gain further insight into practical limi-

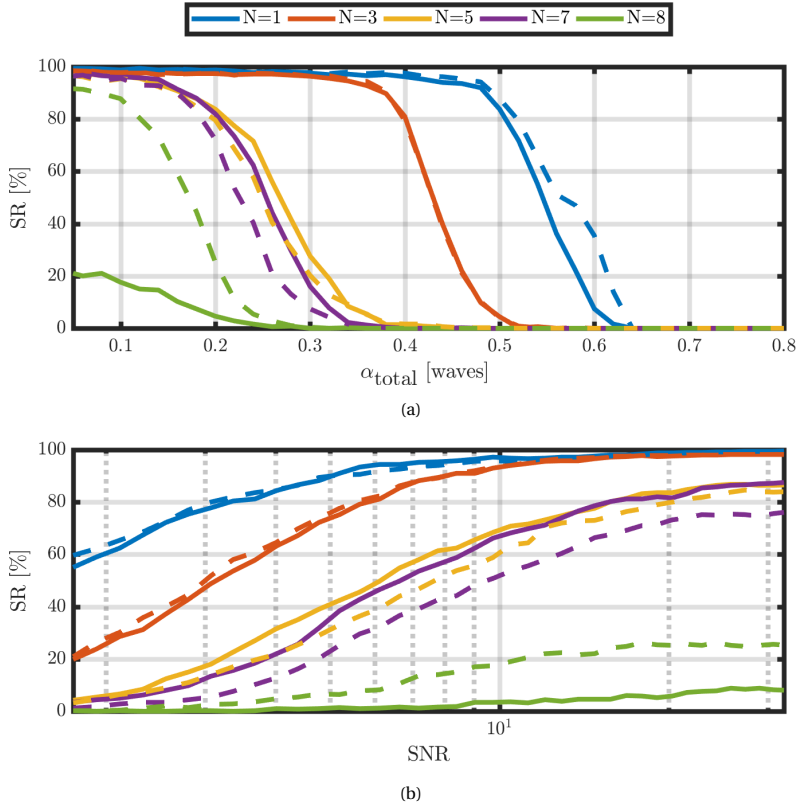


Figure 5.6: (a) Dependency of the success rate (SR) on the total wavefront error α_{total} for an asymmetrical (solid line) and a symmetrical (dashed line) configuration, considering the number of photons per channel $K_m = 1.2 \cdot 10^8$. (b) Dependency of the success rate (SR) on the signal to noise ratio for an asymmetrical (solid line) and a symmetrical (dashed line) configuration, considering a total wavefront error of $\alpha_{\text{total}} = 0.2$ waves. The values are obtained for an optimized defocus diversity $\Delta_4 = 0.7$ waves.

tations of the proposed PEPD approach by analyzing the success rate dependency on the total wavefront error α_{total} and the signal to noise ratio (SNR). Figure 5.6 (a) illustrates the dependency of the success rate on the total wavefront error α_{total} for the asymmetrical and the symmetrical configuration. The particular defocus diversity $\Delta_4 = 0.7$ waves is considered, which represents the previously obtained optimum value for $N = 7$. It can be seen that wavefronts that are aberrated by defocus and astigmatism ($N = 3$) can be reliably retrieved up to $\alpha_{\text{total}} = 0.4$ waves. The limit for the retrieval of up to $N = 7$ modes is close to the previously considered total rms wavefront error of $\alpha_{\text{total}} = 0.2$ waves. Figure 5.6 (a) further indicates that wavefronts including spherical aberration (Z_{11}) could be retrieved in an asymmetrical PEPD configuration for small rms errors of $\alpha_{\text{total}} < 0.1$ waves. Finally, the dependency of the success rate on the SNR is investigated in Fig. 5.6 (b) for an equal defocus diversity $\Delta_4 = 0.7$ waves and $\alpha_{\text{total}} = 0.2$ waves. To this end, the SNR is scaled by adjusting the number of detected photons K_m per channel according to Eq. (5.6). Wavefronts that are aberrated by defocus and astigmatism ($N = 3$) can be reliably

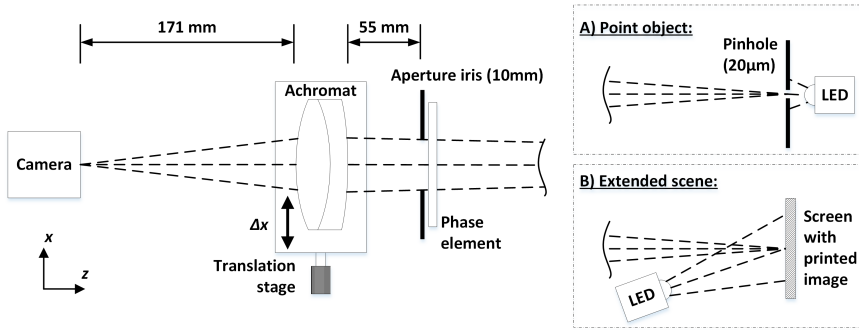


Figure 5.7: Schematic sketch of the optical setup applied for testing the PEPD method based on imaging a point object (A) and an extended scene (B). Note that the distance between the phase element and (A) the pinhole and (B) the extended screen is 1.8 m.

5

retrieved with a success rate greater 80% down to a very low SNR ≈ 5 for a symmetrical configuration. The same success rate performance necessitates SNR ≈ 20 for $N = 7$. This result demonstrates the robustness of the presented aberration retrieval approach in the presence of considerable image noise. For comparison, the numerical simulations performed for the validation of the deep learning method proposed in [27] only considered a negligible noise level that corresponds to SNR = 10^5 .

In summary, the performed numerical investigation of the success rate shows that the proposed PEPD approach provides an efficient and practical method, which can be applied to retrieve wavefronts that are dominated by low order Zernike modes up to $N = 7$ (excluding piston, tip and tilt).

5.5. EXPERIMENTAL RESULTS

An optical setup characterized by the same parameters as the previously simulated system is implemented experimentally using a commercially available lens (THORLABS achromate AC254-150-A-ML) in combination with a commercially available machine vision CMOS camera (IDS MuEye). The camera provides a resolution of 2456x2054 pixels with a size of $3.45 \mu\text{m}$. The iris aperture stop is placed 55 mm in front of the lens. Note that the nominal system provides a diffraction limited performance over the entire field of view. The same phase element as used in [31] is placed inside the aperture stop to generate the triple-helix PSF. The element consists of a thin, surface structured borosilicate glass sample and provides low intrinsic aberrations of the transmitted wavefront. A schematic sketch of the optical setup is shown in Fig. 5.7. A set of low order, field dependent aberrations is introduced into the experimental optical setup by applying a combination of two different measures. On the one hand, the achromatic lens is moved laterally in x-direction away from the optical axis defined by the center of the aperture stop as indicated in Fig. 5.7. The image shift, which can be associated with tip and tilt aberration, is neglected. Only Zernike coefficients associated with defocus, coma and astigmatism are considered, which constitute the dominating aberration modes that are introduced. On the other hand, the achromatic lens is utilized in a reverse direction,

which results in an increased amount of first order coma and astigmatism. Note that the spherical aberration as well as higher order modes remains negligible ($\alpha_n < \lambda/50$) due to the high system F-number and small field of view. In summary, the aberrations introduced to the experimental system by a certain lens shift Δx can be understood as a particular sample of the previously investigated aberration set with $N = 5$. Note that the misalignment of an optical system via introducing an element shift or tilt is commonly used to practically evaluate the PD aberration measurement performance [21, 48].

The introduced aberrations are initially measured based on imaging a point source object. This makes a quantitative comparison possible between the proposed PEPD method and a conventional aberration retrieval based on a least-square PSF fit. Subsequently, an extended object scene is considered and the method's capability for retrieving field dependent aberration coefficients for an unknown object is tested. Only the symmetrical PD scenario is considered for both experiments, due to the superior performance compared to the asymmetric configuration as discussed in section 5.4.3.

5.5.1. POINT OBJECT APPROACH VERIFICATION

A point object is experimentally realized by a combination of a high power LED source ($\lambda = 540 \text{ nm}$) and a pinhole with a diameter of $20 \mu\text{m}$. This assembly is placed at a nominal distance of 1.8 m in front of the experimental setup, which results in a demagnification factor of 11.9 between the object and the image plane. The pinhole cannot be resolved by the optical setup and therefore provides an adequate point source. A set of 20 images of the point object with different noise realizations is acquired at two image planes, symmetrically located $\pm 2.0 \text{ mm}$ around the nominal focus position, using the triple-helix PSF. This distance from the nominal focus corresponds to a defocus diversity of $\Delta_4 = 0.53$ waves, which is close to the optimum value for $N = 5$ found in the numerical simulations for $N = 5$. The average distributions of the acquired images are illustrated in the top part of Fig. 5.8 for different amounts of introduced lens shift Δx .

The aberration coefficients for defocus, primary astigmatism and coma are retrieved based on the proposed linear PEPD approach. The simulated linear transfer matrix \hat{T} and the nominal cepstrum peak position $(\mathbf{x}^c, \mathbf{y}^c)_{m,0}$, obtained in section 5.3, are used. The bottom part of Fig. 5.8 shows the measured aberration coefficients α_n of the relevant Zernike modes ($N = 5$) as well as the total wavefront error α_{total} depending on the introduced lens shift up to 3.5 mm . The small errorbars, which correspond to the statistical rms deviation of the retrieved coefficients for the 20 images, indicate a high relative accuracy of the retrieval.

In order to validate the proposed approach and to evaluate the absolute precision, a comparison with a conventional, maximum-likelihood estimation (MLE) method is performed. In particular, the MLE aberration coefficients are determined by minimizing the mean-square error metric

$$E = \sum_{m=1}^2 \sum_{\mathbf{x}} [h_m(\mathbf{x}) - \hat{h}_m(\mathbf{x})]^2 \quad (5.14)$$

that is also used for conventional phase diversity [15]. The measured and the estimated PSFs are denoted by $h_m(\mathbf{x})$ and $\hat{h}_m(\mathbf{x})$, respectively. The latter is related to the aberrated, triple-helix pupil function according to Eq. (5.4). In addition to the experimental part,

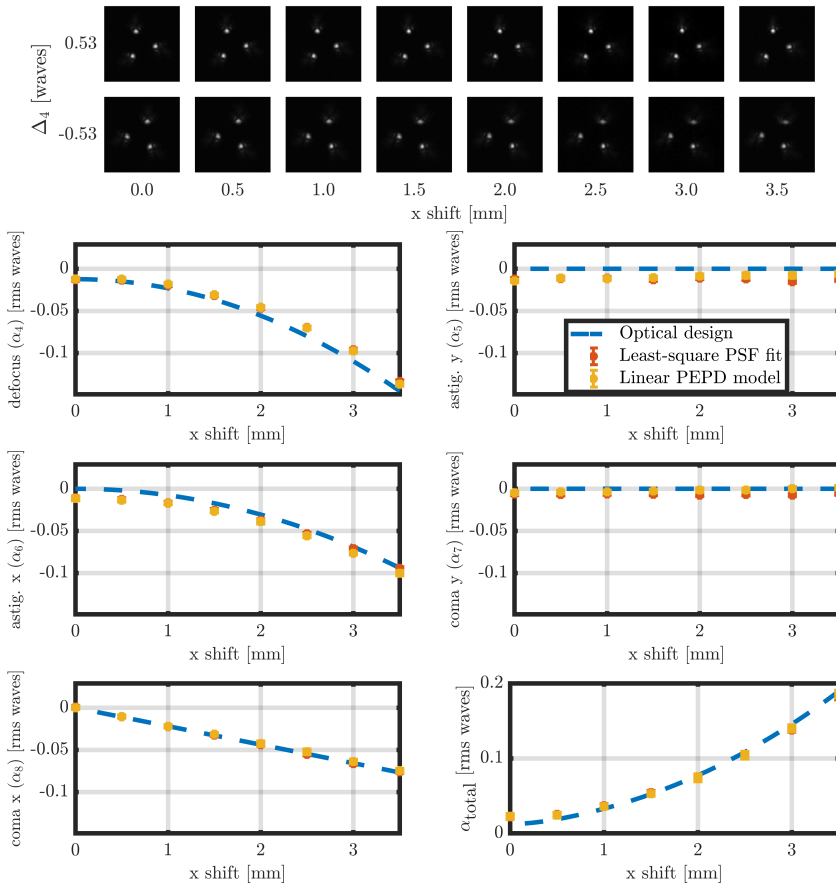


Figure 5.8: Top: Measured triple-helix PSF distributions for the two considered diversity channels and for different amounts of introduced lens shift Δx . Bottom: Comparison of the retrieved Zernike aberration coefficients α_n and the measured total rms wavefront error α_{total} for different amounts of introduced lens shift Δx .

the validation of the PEPD method is performed by comparing the measured aberration coefficients to the coefficients extracted from simulating the setup using a standard, optical design software (OpticStudio). As can be seen in the bottom part of Fig. 5.8, the values of the obtained coefficients using the proposed PEPD method agree well with the reference values obtained by the maximum-likelihood estimation and the simulations. The maximum absolute deviation between the fit and the linear PEPD is on the order of $\lambda/100$ and, therefore, demonstrates a successful aberration retrieval.

We emphasize that an accurate knowledge of the basic system parameters is essential for a successful aberration retrieval, which is a well known practical limitation of phase diversity. In particular, an uncertainty in the nominal focus position leads to an equal estimation error for the defocus aberration coefficient α_4 [49]. Other system parameters that, in general, significantly influence the PD retrieval accuracy include the exit pupil

size and location [49]. However, we find that a deviation of 10% between the considered parameters and the true values only leads to an additional measurement inaccuracy in the order of $\lambda/100$ for the system investigated here, if the proposed PEPD method is applied.

5.5.2. EXTENDED SCENE

The point source assembly used in the previous experiment is replaced by an extended screen that represents an extended object distribution (see Fig. 5.7). An exemplary, gray scale satellite image is printed onto the extended screen, which is placed at the same object distance of 1.8 m used in the previous experiment. Imaging this particular object distribution may represent a remote sensing application scenario. The printed object scene is illuminated by the previously used high power LED source. Low order optical aberrations dominated by defocus, primary astigmatism and coma are introduced to the optical setup in an equivalent manner compared to the previous experiment by shifting the inverted achromatic lens by 3.5 mm. Figure 5.9 (a) and (b) show in-focus, raw camera images of the aberrated scene acquired with a nominal and a triple-helix pupil function, respectively.

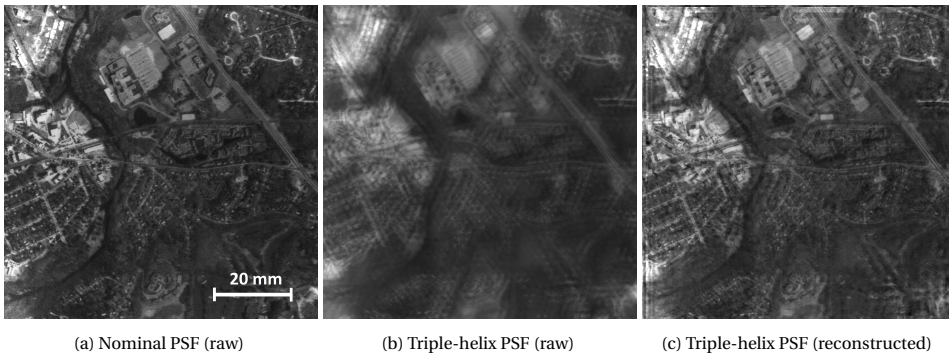


Figure 5.9: (a), (b) Raw images of the extended screen captured by the experimental demonstration setup using the nominal PSF and a triple-helix PSF, respectively, for an in-focus diversity channel ($\Delta_4 = 0$ waves). (c) Reconstructed object distribution of the raw image shown in (b) using the Wiener deconvolution approach presented in [32]. Note that the imaged object scene corresponds to an exemplary, gray scale satellite image printed onto the extended screen with a size indicated by the scale bar in (a).

In comparison to the previous investigation of a point source, a field dependency of the aberrations coefficients α_n needs to be considered for the extended scene. In order to obtain a two-dimensional map of the coefficients based on the proposed power cepstrum analysis, the image segmentation approach used for obtaining depth maps is applied [32]. In particular, the cropped camera image with a size of 2048x2048 pixels is divided into smaller sub-images with a size of 512x512 pixels and a lateral separation of 128 pixels, which leads to an overall aberration map sampling of 13x13 pixels. The local aberration coefficients are calculated for each sub-image based on the proposed, linear PEPD approach using the simulated system parameters \hat{T} and $(\mathbf{x}^c, \mathbf{y}^c)_{m,0}$ and a defocus diversity of $\Delta_4 = 0.53$ waves. The obtained field distributions of the coefficients α_n as well as the total wavefront error α_{total} are directly plotted in Fig. 5.10. Note that

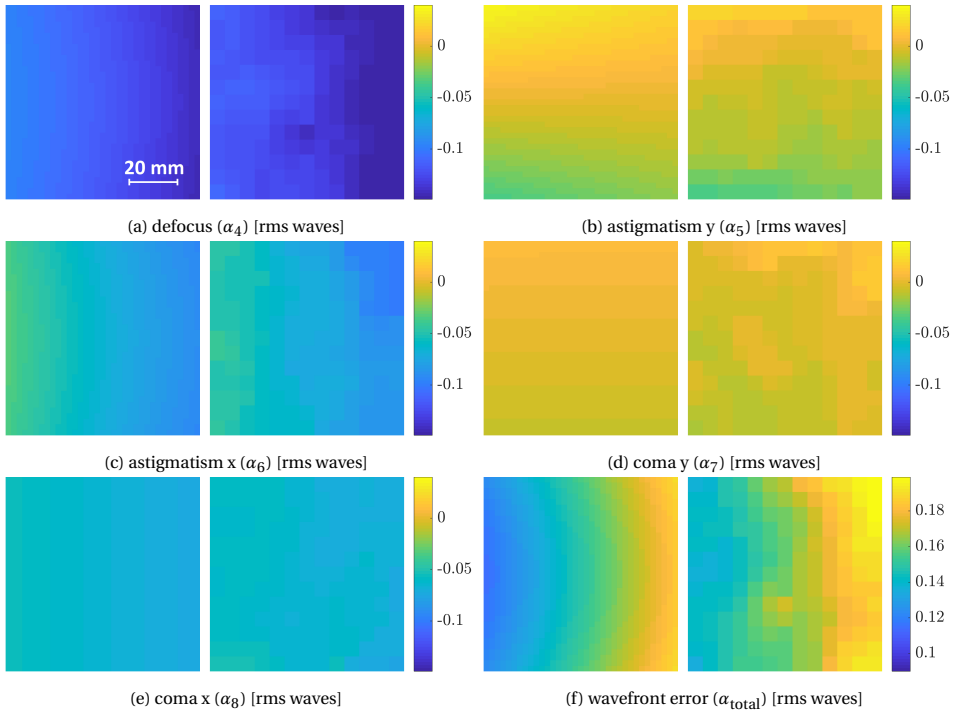


Figure 5.10: Comparison of the field dependent aberration coefficients obtained by the proposed linear PEPD model (right columns) and the corresponding values extracted from the optical design (left columns). The aberrations are introduced by shifting the inverted achromatic lens $\Delta x = 3.5 \text{ mm}$ away from the optical axis. The scale bar in (a) indicates the object field extension of the coefficient maps.

no smoothing was applied. The obtained results can be understood using third-order nodal aberration theory [50]. In contrast to a conventional, rotational symmetric optical system, the introduced lens shift generates distinct nodal points away from the optical axis for field curvature (field dependent defocus), coma and astigmatism. In particular, the individual image space nodal points for field curvature and coma are located approximately 22 mm and 20 mm away from the image center in negative x direction, respectively. The two nodal points for astigmatism are located approximately 6 mm and 30 mm away from the image center in negative and positive x direction, respectively. Accordingly, the nodal points are located outside the considered sensor width of 7 mm and cannot directly be observed in the plots shown in Fig. 5.10. The comparison with the theoretical nodal fields extracted from the optical design in Fig. 5.10, however, shows an agreement of the absolute aberration coefficients and the field dependency. The successful retrieval of field dependent wavefront aberrations (for $N = 5$ up to $\alpha_{\text{total}} \approx 0.2$ waves) is therefore demonstrated experimentally. The arbitrary, extended scene provides a significantly increased level of complexity in comparison to the simplified objects considered for alternative machine learning methods [14, 27]. It is emphasized that the calculation of the entire coefficient distributions can be performed in less than 7s using

a conventional laptop due to the fast linear retrieval model.

Depending on the particular application, the actual object distribution $o(\mathbf{x})$ may be of interest in addition to the measured aberration coefficients α_n . The obtained information on the local PSF peak parameters $(\mathbf{x}^c, \mathbf{y}^c)$ can be used to reconstruct the object distribution from the pupil-engineered image. Fig. 5.9 (c) exemplarily shows the reconstructed object distribution for the raw image in Fig. 5.9 (b) using an adapted Wiener deconvolution as described in [32]. It can be seen that the effect of the triple-helix PSF, which leads to an overlap of three shifted version of the object, is removed and small object features such as individual buildings and roads are retrieved.

5.6. CONCLUSION

A novel concept that combines conventional phase diversity aberration retrieval with helical point spread functions has been presented. It makes a fast estimation of low order aberration coefficients possible based on imaging an arbitrary, extended (natural) object and solving a linear system of equations. Numerical simulations have been performed, which evaluate the performance of the presented method based on the CRLB and the aberration retrieval success rate. To this end, an expression for the CRLB associated with the phase diversity aberration measurement was derived considering an unknown object. Although the CRLB performance of the helical PSFs is inferior in comparison to a conventional PSF, the proposed approach provides a practical tool to estimate the coefficients of up to 7 Zernike aberrations with sufficient accuracy (i.e. up to the diffraction limit) without the need for numerically extensive, iterative phase retrieval procedures. The proposed aberration retrieval has been demonstrated experimentally by retrieving the field dependent aberration coefficients for a misaligned optical system based on an unknown, extended scene.

The proposed aberration retrieval method can be understood as an extension of the application scope of helical PSFs. Previous studies targeted the measurement of defocus aberration in order to retrieve depth information. With the method presented here, up to 7 aberration modes can be retrieved fast and reliably. The method is considered useful for practical applications including co-phasing of segmented optical mirrors [51], general system alignment and the adaptive optical correction of mechanically or thermally introduced aberrations [52], particularly for cases in which no point source is available. Here, it can be applied to directly characterize and minimize field dependent aberrations (e.g. in a closed-loop). Alternatively, it may be used to obtain a robust initial aberration estimate for a conventional iterative PD aberration retrieval approach [15, 16].

The results here are obtained with a helical PSF that was originally designed and optimized for depth imaging (defocus measurement over a large range of interest). The performance with respect to the CRLB and the aberration retrieval success rate could be further improved by incorporating PSFs that are tailored to the phase diversity problem. As an example, such PSF designs could be optimized w.r.t. the spot size for only two dedicated defocus diversity positions.

ACKNOWLEDGMENTS

We thank Carlas Smith for research advice.

REFERENCES

- [1] R. Berlich and S. Stallinga, *Image based aberration retrieval using helical point spread functions*, *Applied Optics* **59**, 6557 (2020).
- [2] W. H. Southwell, *Wave-front analyzer using a maximum likelihood algorithm*, *Journal of the Optical Society of America* **67**, 396 (1977).
- [3] J. R. Fienup, *Phase retrieval algorithms: a comparison*, *Applied Optics* **21**, 2758 (1982).
- [4] J. N. Cederquist, J. R. Fienup, C. C. Wackerman, S. R. Robinson, and D. Kryskowski, *Wave-front phase estimation from Fourier intensity measurements*, *Journal of the Optical Society of America A* **6**, 1020 (1989).
- [5] X. Liu, L. Wang, J. Wang, and H. Meng, *A three-dimensional point spread function for phase retrieval and deconvolution*, *Optics Express* **20**, 15392 (2012).
- [6] B. Ellerbroek and D. Morrison, *Linear Methods In Phase Retrieval*, in *Wavefront Sensing*, Vol. 0351, edited by Noah Bareket and Chris L. Koliopoulos (SPIE, 1983) pp. 90–95.
- [7] C. S. Smith, R. Marinică, A. J. den Dekker, M. Verhaegen, V. Korhikoski, C. U. Keller, and N. Doelman, *Iterative linear focal-plane wavefront correction*, *Journal of the Optical Society of America. A, Optics, image science, and vision* **30**, 2002 (2013).
- [8] A. Polo, S. F. Pereira, and P. H. Urbach, *Theoretical analysis for best defocus measurement plane for robust phase retrieval*, *Opt. Lett.* **38**, 812 (2013).
- [9] D. Yue, H. Nie, Y. Li, and C. Ying, *Fast correction approach for wavefront sensorless adaptive optics based on a linear phase diversity technique*, *Applied Optics* **57**, 1650 (2018).
- [10] H. Guo, N. Korablinova, Q. Ren, and J. Bille, *Wavefront reconstruction with artificial neural networks*, *Optics Express* **14**, 6456 (2006).
- [11] S. W. Paine and J. R. Fienup, *Machine learning for improved image-based wavefront sensing*, *Opt. Lett.* **43**, 1235 (2018).
- [12] G. Ju, X. Qi, H. Ma, and C. Yan, *Feature-based phase retrieval wavefront sensing approach using machine learning*, *Optics Express* **26**, 31767 (2018).
- [13] S. Lohani and R. T. Glasser, *Turbulence correction with artificial neural networks*, *Opt. Lett.* **43**, 2611 (2018).
- [14] Y. Nishizaki, M. Valdivia, R. Horisaki, K. Kitaguchi, M. Saito, J. Tanida, and E. Vera, *Deep learning wavefront sensing*, *Optics Express* **27**, 240 (2019).
- [15] R. A. Gonsalves, *Phase Retrieval And Diversity In Adaptive Optics*, *Optical Engineering* **21** (1982), 10.1117/12.7972989.

- [16] L. M. Mugnier, A. Blanc, and J. Idier, *Phase Diversity: A Technique for Wave-Front Sensing and for Diffraction-Limited Imaging*, (Elsevier, 2006) pp. 1–76.
- [17] R. G. Paxman, T. J. Schulz, and J. R. Fienup, *Joint estimation of object and aberrations by using phase diversity*, *Journal of the Optical Society of America A* **9**, 1072 (1992).
- [18] A. Blanc, L. M. Mugnier, and J. Idier, *Marginal estimation of aberrations and image restoration by use of phase diversity*, *Journal of the Optical Society of America A* **20**, 1035 (2003).
- [19] M. W. Smith, *Use of adaptive optics to implement nonquadratic phase diversity imaging*, *Proc. of SPIE* **5524**, 66 (2004).
- [20] R. L. Kendrick, D. S. Acton, and A. L. Duncan, *Phase-diversity wave-front sensor for imaging systems*, *Applied Optics* **33**, 6533 (1994).
- [21] N. Miyamura, *Generalized phase diversity method for self-compensation of wave-front aberration using spatial light modulator*, *Optical Engineering* **48**, 128201 (2009).
- [22] M. R. Bolcar and J. R. Fienup, *Sub-aperture piston phase diversity for segmented and multi-aperture systems*, *Applied Optics* **48**, A5 (2009).
- [23] J.-F. Sauvage, L. Mugnier, B. Paul, and R. Vilecroze, *Coronagraphic phase diversity: a simple focal plane sensor for high-contrast imaging*, *Opt. Lett.* **37**, 4808 (2012).
- [24] L. Yang, A. El-Tamer, U. Hinze, J. Li, Y. Hu, W. Huang, J. Chu, and B. N. Chichkov, *Parallel direct laser writing of micro-optical and photonic structures using spatial light modulator*, *Optics and Lasers in Engineering* **70**, 26 (2015).
- [25] D. Wilding, P. Pozzi, O. Soloviev, G. Vdovin, and M. Verhaegen, *Pupil mask diversity for image correction in microscopy*, *Optics Express* **26**, 14832 (2018).
- [26] I. Mocoer, L. M. Mugnier, and F. Cassaing, *Analytical solution to the phase-diversity problem for real-time wavefront sensing*, *Opt. Lett.* **34**, 3487 (2009).
- [27] Q. Xin, G. Ju, C. Zhang, and S. Xu, *Object-independent image-based wavefront sensing approach using phase diversity images and deep learning*, *Optics Express* **27**, 26102 (2019).
- [28] C. Roider, R. Piestun, and A. Jesacher, *3D image scanning microscopy with engineered excitation and detection*, *Optica* **4**, 1373 (2017).
- [29] C. Smith, M. Huisman, M. Siemons, D. Grünwald, and S. Stallinga, *Simultaneous measurement of emission color and 3D position of single molecules*, *Optics Express* **24**, 4996 (2016).
- [30] S. R. P. Pavani, A. Greengard, and R. Piestun, *Three-dimensional localization with nanometer accuracy using a detector-limited double-helix point spread function system*, *Applied Physics Letters* **95**, 021103 (2009).

- [31] R. Berlich and S. Stallinga, *High-order-helix point spread functions for monocular three-dimensional imaging with superior aberration robustness*, *Opt. Express* **26**, 4873 (2018).
- [32] R. Berlich, A. Bräuer, and S. Stallinga, *Single shot three-dimensional imaging using an engineered point spread function*, *Opt. Express* **24**, 5946 (2016).
- [33] C. Wang, G. Ballard, R. Plemmons, and S. Prasad, *Joint 3D localization and classification of space debris using a multispectral rotating point spread function*, *Applied Optics* **58**, 8598 (2019).
- [34] D. J. Lee, M. C. Roggemann, and B. M. Welsh, *Cramér–Rao analysis of phase-diverse wave-front sensing*, *J. Opt. Soc. Am. A* (1999).
- [35] J. J. Dolne and H. B. Schall, *Cramer–Rao bound and phase-diversity blind deconvolution performance versus diversity polynomials*, *Applied Optics* **44**, 6220 (2005).
- [36] S. Prasad, *Fisher-information-based analysis of a phase-diversity-speckle imaging system*, *Journal of the Optical Society of America A* **21**, 2073 (2004).
- [37] J. J. Dolne, *Evaluation of the phase diversity algorithm for noise statistics error and diversity function combination*, (2006) p. 630708.
- [38] B. H. Dean and C. W. Bowers, *Diversity selection for phase-diverse phase retrieval*, *Journal of the Optical Society of America A* **20**, 1490 (2003).
- [39] O. Russakovsky, J. Deng, H. Su, J. Krause, S. Satheesh, S. Ma, Z. Huang, A. Karpathy, A. Khosla, M. Bernstein, A. C. Berg, and L. Fei-Fei, *ImageNet Large Scale Visual Recognition Challenge*, *International Journal of Computer Vision* **115**, 211 (2015).
- [40] D. R. Gerwe, J. L. Hill, and P. S. Idell, *Cramér-Rao analysis of orientation estimation: influence of target model uncertainties*, *Journal of the Optical Society of America A* **20**, 817 (2003).
- [41] S. M. Kay, *Fundamentals of statistical signal processing: Estimation theory*, Vol. 1 (Prentice-Hall, US, 1993).
- [42] D. R. Gerwe and P. S. Idell, *Cramér-Rao analysis of orientation estimation: viewing geometry influences on the information conveyed by target features*, *Journal of the Optical Society of America A* **20**, 797 (2003).
- [43] C. L. Matson, K. Borelli, S. Jefferies, C. C. Beckner, E. K. Hege, and L. H. Michael, *Fast and optimal multiframe blind deconvolution algorithm for high-resolution ground-based imaging of space objects*, *Applied Optics* **48**, 75 (2009).
- [44] M. Badieirostami, M. D. Lew, M. A. Thompson, and W. E. Moerner, *Three-dimensional localization precision of the double-helix point spread function versus astigmatism and biplane*, *Applied Physics Letters* **97**, 161103 (2010).
- [45] G. Grover, S. R. P. Pavani, and R. Piestun, *Performance limits on three-dimensional particle localization in photon-limited microscopy*, *Optics Letters* **35**, 3306 (2010).

- [46] M. K. Sharma, C. Gaur, P. Senthilkumaran, and K. Khare, *Phase imaging using spiral-phase diversity*, *Applied Optics* **54**, 3979 (2015).
- [47] S. Echeverri-Chacón, R. Restrepo, C. Cuartas-Vélez, and N. Uribe-Patarroyo, *Vortex-enhanced coherent-illumination phase diversity for phase retrieval in coherent imaging systems*, *Opt. Lett.* **41**, 1817 (2016).
- [48] J. J. Dolne, R. J. Tansey, K. A. Black, J. H. Deville, P. R. Cunningham, K. C. Widen, and P. S. Idell, *Practical issues in wave-front sensing by use of phase diversity*, *Applied Optics* **42**, 5284 (2003).
- [49] A. Blanc, T. Fusco, M. Hartung, L. M. Mugnier, and G. Rousset, *Calibration of NAOS and CONICA static aberrations*, *A&A* **399**, 373 (2003).
- [50] K. Thompson, *Description of the third-order optical aberrations of near-circular pupil optical systems without symmetry*, *Journal of the Optical Society of America A* **22**, 1389 (2005).
- [51] L. D. Feinberg, B. H. Dean, D. L. Aronstein, C. W. Bowers, W. Hayden, R. G. Lyon, R. Shiri, J. S. Smith, D. S. Acton, L. Carey, A. Contos, E. Sabatke, J. Schwenker, D. Shields, T. Towell, F. Shi, and L. Meza, *TRL-6 for JWST wavefront sensing and control*, in *UV/Optical/IR Space Telescopes: Innovative Technologies and Concepts III*, Vol. 6687 (SPIE, 2007) p. 668708.
- [52] N. Devaney, C. Reinlein, N. Lange, M. Goy, A. Goncharov, and P. Hallibert, *HYPATIA and STOIC: an active optics system for a large space telescope*, in *Proc. SPIE 9904, Space Telescopes and Instrumentation 2016: Optical, Infrared, and Millimeter Wave*, Vol. 9904, p. 990469.

6

CONCLUSION

6.1. RESULTS

This thesis presents evidence that computational optical systems which incorporate helical point spread functions provide a powerful tool for enhanced imaging and sensing applications. The work performed here provides the foundation to extend the application scope of this approach beyond its original use for super-resolution microscopy, i.e. three-dimensional single-molecule and particle localization, and enable other computational imaging applications to benefit from its unique advantages. The application scenarios addressed here include three-dimensional imaging, i.e. for machine vision problems, and wavefront sensing, both considering extended, unknown objects. So far, a direct application of helical PSFs in these areas was not possible due to severe shortcomings in its current implementation as described in section 1.2. Therefore, novel concepts that span the complete computational imaging process chain from optical image acquisition to digital image processing were developed holistically in order to overcome these shortcomings. These system level advances were supported further by substantial improvements of individual sub-system aspects of PSF engineered systems, which includes the optical design and the manufacturing of the pupil masks as well as the image processing of the encoded image. The individual accomplishments were validated theoretically and experimentally using dedicated test setups. The following sections detail the main research results achieved in the scope of this thesis.

6

6.1.1. PASSIVE, MONOCULAR 3D IMAGING ACQUISITION

A computational optical system approach for three-dimensional imaging using helical point spread functions has been developed and tested experimentally. It has been demonstrated in chapter 2 that the passive, monocular approach only necessitates a single shot image acquisition in order to extract the lateral as well as the depth information of an extended scene. The proposed concept can be practically implemented using a compact and cost efficient camera system with a low hardware complexity. Furthermore, we have shown in chapter 4 that the computational optical system can be rendered with an increased robustness with respect to first order optical aberrations due to the utilization of novel, high-order helical PSF designs. The proposed concept is therefore suitable for machine vision applications. Based on the limitations of previous helical PSF system implementations in the area of super-resolution microscopy, the following detailed achievements have been obtained in terms of the optical design, the practical phase element implementation as well as the image processing.

Optical design The advancements in the optical design of PSF engineered systems featuring helical PSFs can be divided into improvements of the phase element design concept and advances with respect to overall optical system design. The novel phase element design concept developed in chapter 4 enables the generation of multi-order helical PSFs featuring an arbitrary number of N peaks. These PSFs provide a depth dependent rotation and, in contrast to previous designs [1, 2], feature a large peak separation on the order of ten times the peak diameter while maintaining well-confined peaks over an extended rotation range of $2\pi/N$. Furthermore, it has been demonstrated in chapter 4 that the novel design approach can be extended to continuous phase profile designs that can be realized by purely refractive (free-form) optical elements. These are expected

to offer helical PSFs with reduced color artifacts compared to the conventional designs, which is crucial for imaging applications that rely on the acquisition of a wide wavelength spectrum.

In addition to the improvements of the particular phase element design approach, the design of PSF engineered systems featuring helical PSFs has been analysed on a system level in chapter 4, i.e. in terms of aberration robustness. In particular, it has been shown by numerical simulations which aberrations lead to false PSF rotation and, therefore, compromise the depth retrieval accuracy. It was shown that first order aberrations such as astigmatism and spherical aberration severely impact the depth measurement for pupil engineered systems that rely on a conventional, double-helix PSF. In contrast, the simulations revealed that the double-helix PSF rotation angle is not susceptible to coma or trefoil aberrations. An analytic analysis indicates that only Zernike aberrations with an azimuthal order $m = \kappa \cdot N$ ($\kappa = 0, 1, 2, \dots$) result in a PSF rotation. This result constitutes a major outcome of this thesis as it provides a guideline for balancing optical aberrations during the design of computational optical systems with rotating PSFs. Furthermore, it suggests that the novel, high-order helical PSFs featuring three or more rotating peaks can benefit computational imaging by rendering the depth measurement with improved aberration robustness. This hypothesis was demonstrated numerically and experimentally in chapter 4 using a dedicated test setup that verified the robustness of triple-helix PSFs to varying astigmatism across the field of view.

Pupil mask manufacturing Two fabrication schemes for generating the pupil masks, also referred to as computer generated holograms (CGHs), that generate helical PSFs were developed and experimentally demonstrated. The first method is based on a sequence of state-of-the-art, wafer-scale optical lithography manufacturing steps. It enables generating phase elements with a high surface accuracy due to a unique combination of a reactive-ion-etching and UV-imprinting. It provides a high level of cost efficiency for a large-scale production of equal phase elements due to the incorporated wafer level replication. The final elements provide increased temperature and mechanical stability in comparison to previous elements [1]. They can be used for RGB imaging as they provide improved transparency over the entire visual range. The manufacturing procedure was applied in chapter 4 to fabricate compact phase elements with a high light efficiency. It was experimentally verified that they provide an adequate wavefront quality for generating helical PSFs with well-defined peaks that can be used for a depth retrieval using the system approach presented in chapter 2.

In addition, an alternative CGH manufacturing approach was developed and demonstrated experimentally in chapter 3. It utilizes a method referred to as Femtosecond-Laser-Direct-Writing (FLDW) to generate phase elements inside transparent bulk materials. In comparison to the lithographic method, this fabrication approach provides a more cost efficient manufacturing solution for small numbers of fabricated samples. It provides a compromise between high flexibility and cost-efficiency since it only requires a single fabrication step. It has been demonstrated that the fabricated elements can be embedded in an optically transparent material. Therefore, the elements provide the basis for highly integrated and robust computational imaging solution.

In summary, both methods provide high compactness, mechanical robustness and light-

efficiency and do not necessitate wavelength or polarization filters. Accordingly, they represent adequate solutions for generating helical PSFs for machine vision application scenarios.

Image processing The development of a novel image processing approach constitutes the major achievement of this thesis, as it is the key for a universal utilization of helical PSFs for general computational imaging applications including three-dimensional imaging and wavefront sensing. In particular, a numerically efficient post-processing concept has been developed in chapter 2 that allows for retrieving the axial and lateral information of an extended, unknown scene in a single image acquisition. It has been demonstrated that the calculation of the encoded image's power cepstrum can be used to efficiently separate the object features from the PSF peak parameters, which constitutes one of the major challenges for applying helical PSFs for three-dimensional imaging. The cepstrum analysis enables the extraction of the PSF's rotation angle, which provides the information on the object's depth profile. It was then shown in chapter 2 how the PSF information can be used further to extract the lateral object distribution from the encoded image. This was based on the utilization of an adapted Wiener filter, which was shown to be applicable for an efficient reconstruction of the object's (RGB) color information. The entire image processing algorithm does not require extensive, iterative optimization procedures, which constitutes a major feature of the proposed approach as it makes three-dimensional image acquisition at video rates possible. A lab setup was finally implemented in chapter 2 to validate the image processing approach experimentally and to demonstrate the unique capabilities of the entire computational imaging system concept.

6.1.2. IMAGE BASED WAVEFRONT MEASUREMENT

The previously described achievements with respect to monocular, three-dimensional imaging build the foundation for utilizing helical PSFs for additional computational imaging tasks. The novel designs of high-order-helix PSF and the efficient image processing approach for extracting the PSF features from extended objects provide the basis for the developments performed in chapter 5. In particular, a system approach for advanced wavefront measurements is developed using a conventional phase diversity (PD) approach in combination with pupil engineering based on helical PSFs. To this end, a concept has been developed that allows for retrieving the shape of a wavefront in terms of Zernike modes by analysing a shift of the helical PSF peaks. This can be understood as an extension of the commonly explored relationship between an object point's axial distance, which can be associated with a parabolic wavefront, and the rotation angle of the helical PSF. The retrieval can be performed with high numerical efficiency using a simple linear model and without the need for complex iterative estimation procedures. The major feature of the proposed computational imaging approach is that the wavefront can be extracted from imaging an extended (unknown) object using the cepstrum approach developed in chapter 2.

The performance of the approach was analyzed and compared to a conventional PD approach by numerical and analytical investigations. An important result of this analysis is the derivation of an analytic expression for the theoretical precision limit of the wave-

front retrieval in terms of the Cramér-Rao lower bound considering unknown objects. This expression provides general means to compare different wavefront retrieval strategies beyond the particular pupil engineering approach developed in this thesis. The performed numerical simulations show that triple-helix PSFs are superior to conventional double-helix PSFs and enable the estimation of up to 7 Zernike modes, including defocus, astigmatism, coma and trefoil. Finally, the capabilities of the novel PEPD approach was demonstrated experimentally using an aberrated optical test setup to extract a complete two-dimensional map of wavefront coefficients for an extended, unknown scene.

6.2. OUTLOOK

The research results obtained in this thesis provide the foundation for novel application scenarios of pupil engineered computational imaging systems based on helical PSFs. In particular, it has been shown that the use of helical PSFs provides unique advantages in the area of three-dimensional imaging and wavefront sensing in comparison to the state-of-the-art technologies. The dedicated test setups and the performed experiments indicate the high potential of this concept for realizing compact and cost-efficient, computational optical systems with a low hardware complexity. In the following, the potential application scenarios are discussed in detail. Furthermore, additional research challenges and potential technological improvements are illustrated.

6.2.1. MACHINE VISION CAMERAS

The system approach for passive, monocular three-dimensional imaging developed in chapter 2 provides a clear potential for commercial applications. The accomplished advances in the utilization of helical PSFs paves the way for the development of novel types of computational machine vision cameras. Such computational cameras feature a low hardware complexity, as, in contrast to conventional stereo camera setups, they only require the usage of a single image detector. Moreover, the optical system can be implemented by a simple integration of a pupil mask into a conventional objective lens. This renders the approach with a high flexibility as it can be customized to specific machine vision problems. For example, a wide range of object distances and field of views can be addressed by simply selecting the appropriate objective lens. In fact, the proposed concept is generally applicable to varifocal and zoom systems, which represent an important class of imaging systems for machine vision applications. The developed approach offers a high level of compactness and physical robustness, which is advantageous for machine vision applications in harsh environments. The demonstrated pupil mask manufacturing approach in chapter 4, which relies on a lithographic imprinting technology on a wafer-scale, provides high cost-efficiency, i.e. for high-volume production markets. Finally, the fast image processing approach potentially allows for three-dimensional object acquisition at video rates. In view of these significant advantages, the developed computational imaging approach provides a promising solution for a wide range of machine vision problems including quality inspection and process control in production lines, as well as robot guidance e.g. for human-machine interactions. In fact, the start-up company *Double Helix Optics*, which originally only targeted applications in the area of super-resolution microscopy, is currently planning on expanding their product line

in order to address the machine vision market [3]. In particular, the company pursues the goal to develop three-dimensional imaging systems for machine vision applications using the system approach developed in chapter 2, which confirms the high commercialization potential of the developed approach.

In order to increase the attractiveness of computational imaging systems using helical PSFs for machine vision applications and to reduce the market entry threshold of this technology, several improvements of the proposed approach should be considered in future research. The depth retrieval approach presented in chapter 2 relies on calculating the power cepstrum of extended subwindows across the complete image. The size of these subwindows is commonly larger than 100 pixels in order to obtain a sufficient signal to noise ratio for the cepstrum analysis. This significantly limits the lateral resolution of the depth map and, therefore, the overall performance of the computational imaging system. A potential strategy to increase the lateral depth map resolution can be found in conventional stereo vision systems. In particular, the cepstrum calculation could be combined with other algorithms including Semi Global Block Matching (SGBM) [4] or deep learning [5], which enable a pixelwise depth determination with a sampling that matches the original image.

Another potential improvement of the current system approach may aim at increasing the accessible depth range of helical PSFs. Currently, the accessible depth range is limited by a corresponding PSF rotation range of $2\pi/N$, where N corresponds to the number of PSF peaks. This limitation is due to ambiguities in the rotation angle analysis. The analysis of advanced PSF features in addition to the rotation angle could be used to bypass this limitation. In fact, the distance of the PSF peaks from the rotation axis is increasing with larger rotation angles, which provides additional information that could be utilized to solve the ambiguity issue in the rotation angle measurement. As a result, the accessible depth range of a particular imaging system could be extended, while maintaining the same axial resolution given by the systems' numerical aperture. Alternatively, the numerical aperture of the imaging system could be increased, which improves the axial resolution but reduces the depth of focus. The extended rotation range could then be used to maintain the accessible depth range.

Finally, a major, inherent limitation of passive depth measurement principles is that they require the object of interest to provide adequate spatial features, which restricts the range of applications. Accordingly, future research could explore a potential combination of engineered, helical PSFs and an active, structured illumination to overcome this challenge. To this end, a conventional illumination system that projects a distinct pattern such as a (pseudo-) random dot distribution could be applied and the PSF engineered imaging system proposed in chapter 2 can directly be used. Alternatively, the pupil mask could be implemented within the illumination subsystem in an equivalent manner compared to the proposed imaging system, which would enable the realization of an illumination pattern that rotates with an increasing distance. A conventional imaging system could then be used to extract the depth information using the image processing approach proposed in chapter 1. In fact, this concept has been recently patented by one of the world's leading producers of sensors and sensor solutions for industrial automation applications [6], which provides an additional confirmation of the general potential of helical PSFs for commercial machine vision applications. So far, the

patent solely focuses on the use of double-helix patterns. The utilization of high-order-helix patterns could increase the robustness of the method with respect to aberrations as demonstrated in chapter 4, which is particularly important for illumination systems featuring a large field of view.

6.2.2. WAVEFRONT SENSORS

The novel wavefront sensor approach presented in chapter 5 provides the unique capability of measuring an optical wavefront based on imaging an extended, unknown object. This measurement can be performed with a low hardware complexity and a high numerical efficiency. Accordingly, it enables a fast, closed-loop aberration measurement, which provides an essential technology for multiple practical applications. A dedicated wavefront sensor based on the proposed approach could be incorporated for adaptive optical application scenarios that necessitate the correction of lower order aberrations. In particular, it can be used for the correction of mechanically or thermally introduced aberrations, i.e. for large mirror telescopes [7], or aberrations that originate from microscopic imaging through thick biological samples [8]. Furthermore, it provides a promising technology for the alignment of segmented and multi-aperture optics, which is also referred to as co-phasing. Such optics may include extremely large telescopes [9] or foldable mirror assemblies as proposed for cube sat optical payloads [10]. For earth observation applications in particular, no dedicated point source is available and the wavefront sensing needs to be based on an extended, unknown object. Other potential applications of the developed wavefront measurement concept include the general alignment and performance analysis of optical systems, such as objective lenses or telescopes. This is particularly relevant for the alignment of imaging systems that are based on free-form surfaces as they exhibit a complex field dependency of optical aberrations and, therefore, necessitate the wavefront evaluation over an extended field of view.

The dedicated optimization and adaption of current helical PSF designs for wavefront measurement purposes constitutes a topic that could be addressed in further research efforts. So far, the pupil masks that were used to investigate and to demonstrate the proposed approach in chapter 5 are originally designed and optimized for three-dimensional imaging applications. In particular, the helical PSFs were optimized for a large defocus range, which limits the achievable minimum PSF peak width. However, the proposed two channel phase diversity approach only necessitates an optimized helical PSF shape for two dedicated defocus settings. The consideration of this simplification in the optical design procedure of the phase elements would allow for a reduction of the PSF peak width at the two dedicated defocus positions of interest. This would improve the signal-to-noise ratio of the cepstrum analysis and, therefore, renders the aberration retrieval with an increased robustness with respect to image noise. Furthermore, a smaller calculation window could be considered for the cepstrum analysis, which would allow for a higher spatial resolution of the aberration map.

Finally, the potential of the wavefront sensing approach could be explored in combination with an adaptive optical system as described in [11]. To this end, the capability for correcting an aberrated wavefront using a deformable mirror may be investigated. The combination of the proposed wavefront sensor concept with a deformable mirror that corrects for focusing errors [12] in laser material processing applications constitutes a

promising implementation. This directly exploits the helical PSF's key capability in accurately measuring defocus aberrations. Another aspect of further research efforts could be the customization of the helical PSF design with respect to a particular adaptive optics application. In contrast to the consideration of general Zernike modes in chapter 5, the pupil mask design may be adapted to the most relevant spatial modes of the aberrations and the deformable mirror in order to facilitate an efficient and robust wavefront correction.

6.2.3. FURTHER APPLICATION SCENARIOS

The main motivation for the advancements in the use of engineered, helical PSFs for three-dimensional imaging was based on the machine vision application scenario. Yet, the high compactness, low hardware complexity and cost-efficiency can potentially benefit other fields of application. A specific example in the field of medical imaging is 3D endoscopy, which could benefit from compact, monocular three-dimensional imaging configurations. These configurations could be used for highly integrated sensors that provide significant advantages compared to conventional stereo endoscopy solutions [13]. Another medical application example is three-dimensional imaging through thick tissue, e.g. for analyzing extended blood vessels [14]. The application would directly benefit from the novel image processing approach developed in chapter 2 and the aberration robustness of high-order PSFs developed in chapter 4. Furthermore, the developed computational imaging concept may be used as a basis for novel 3D sensor solutions for security and safety purposes, i.e. secure facial recognition applications in consumer electronics [15] or driver monitoring in automotive applications [16]. An approach for three-dimensional localization and material classification of space debris using helical PSFs was recently introduced in ref. [17]. So far, the method can only be applied to point-like objects but it may potentially be adapted to extended objects using the image processing approach developed in chapter 2. Accordingly, the developments performed in this thesis may enable the utilization of helical PSFs for 5D hyperspectral imaging, which refers to a computational imaging approach for extracting temporal, three-dimensional and spectral object information simultaneously [18].

So far, most computational imaging systems featuring helical PSFs focus on applications in the visible domain. The advancement into different spectral domains would further expand the application scope of the developed three-dimensional imaging and wavefront sensing concepts. Here, infrared imaging is of particular interest as it is used for identifying and classifying chemical structures and it serves as an important tool for astronomical and defense applications. Initial efforts to make the depth measurement approach presented in chapter 2 applicable to the infrared domain are described in ref. [19], where a novel pupil mask implementation based on dielectric metasurfaces is proposed.

REFERENCES

- [1] G. Grover, S. Quirin, C. Fiedler, and R. Piestun, *Photon efficient double-helix PSF microscopy with application to 3D photo-activation localization imaging*, *Biom. Opt. Express* **2**, 3010 (2011).

- [2] S. Prasad, *Rotating point spread function via pupil-phase engineering*, *Optics Letters* **38**, 585 (2013).
- [3] G. Dutton, *Imaging Module Gives 2D Microscopes 3D Vision*, *Genetic Engineering & Biotechnology News* **40** (05/04/2020).
- [4] H. Hirschmüller, *Stereo processing by semiglobal matching and mutual information*, *IEEE Transactions on Pattern Analysis and Machine Intelligence* **30**, 328 (2008).
- [5] W. Luo, A. G. Schwing, and R. Urtasun, *Efficient Deep Learning for Stereo Matching*, in *2016 IEEE Conference on Computer Vision and Pattern Recognition (CVPR)* (IEEE, [Place of publication not identified], 2016) pp. 5695–5703.
- [6] F. Blöbbaum, *VERFAHREN UND VORRICHTUNG ZUR OPTOELEKTRONISCHEN ENTFERUNGSMESSUNG - European Patent Office - EP 3379292 A1*, (2018).
- [7] N. Devaney, C. Reinlein, N. Lange, M. Goy, A. Goncharov, and P. Hallibert, *HYPATIA and STOIC: an active optics system for a large space telescope*, in *Proc. SPIE 9904, Space Telescopes and Instrumentation 2016: Optical, Infrared, and Millimeter Wave*, Vol. 9904, p. 990469.
- [8] Travis J. Gould, Daniel Burke, Joerg Bewersdorf, and Martin J. Booth, *Adaptive optics enables 3D STED microscopy in aberrating specimens*, *Optics Express* **20**, 20998 (2012).
- [9] L. D. Feinberg, B. H. Dean, D. L. Aronstein, C. W. Bowers, W. Hayden, R. G. Lyon, R. Shiri, J. S. Smith, D. S. Acton, L. Carey, A. Contos, E. Sabatke, J. Schwenker, D. Shields, T. Towell, F. Shi, and L. Meza, *TRL-6 for JWST wavefront sensing and control*, in *UV/Optical/IR Space Telescopes: Innovative Technologies and Concepts III*, Vol. 6687 (SPIE, 2007) p. 668708.
- [10] N. Schwartz, D. Pearson, S. Todd, A. Vick, D. Lunney, and D. MacLeod, *A Segmented Deployable Primary Mirror for Earth Observation from a CubeSat Platform*, *Small Satellite Conference* (2016).
- [11] R. Berlich and C. Reinlein, *VORRICHTUNG ZUR MESSUNG EINER ABERRATION, ABBILDUNGSSYSTEME UND VERFAHREN ZUR MESSUNG EINER ABERRATION - European Patent Office - EP 3260829 A1*, (2017).
- [12] T. Kopf, C. Reinlein, M. Goy, R. Eberhardt, J. Langebach, and T. Scheller, *Adapting the axial focus in high-power laser processing machines within mm-range*, in *High-Power Laser Materials Processing: Applications, Diagnostics, and Systems VI*, SPIE Proceedings, edited by S. Kaierle and S. W. Heinemann (SPIE, 2017) p. 100970K.
- [13] V. Parot, D. Lim, G. González, G. Traverso, N. S. Nishioka, B. J. Vakoc, and N. J. Durr, *Photometric stereo endoscopy*, *Journal of Biomedical Optics* **18**, 076017 (2013).
- [14] R. Dickie, R. M. Bachoo, M. A. Rupnick, S. M. Dallabrida, G. M. Deloid, J. Lai, R. A. Depinho, and R. A. Rogers, *Three-dimensional visualization of microvessel architecture of whole-mount tissue by confocal microscopy*, *Microvascular research* **72**, 20 (2006).

- [15] K. Patel, H. Han, and A. K. Jain, *Secure Face Unlock: Spoof Detection on Smartphones*, *IEEE Transactions on Information Forensics and Security* **11**, 2268 (2016).
- [16] A. Fernández, R. Usamentiaga, J. L. Carús, and R. Casado, *Driver Distraction Using Visual-Based Sensors and Algorithms*, *Sensors (Basel, Switzerland)* **16** (2016), 10.3390/s16111805.
- [17] C. Wang, G. Ballard, R. Plemmons, and S. Prasad, *Joint 3D localization and classification of space debris using a multispectral rotating point spread function*, *Applied Optics* **58**, 8598 (2019).
- [18] S. Heist, C. Zhang, K. Reichwald, P. Kühmstedt, G. Notni, and A. Tünnermann, *5D hyperspectral imaging: fast and accurate measurement of surface shape and spectral characteristics using structured light*, *Opt. Express* **26**, 23366 (2018).
- [19] C. Jin, M. Afsharnia, R. Berlich, S. Fasold, C. Zou, D. Arslan, I. Staude, T. Pertsch, and F. Setzpfandt, *Dielectric metasurfaces for distance measurements and three-dimensional imaging*, *Advanced Photonics* **1**, 1 (2019).

ACKNOWLEDGEMENTS

In this chapter, I would like to take the opportunity to thank the people who supported me in performing the work that resulted in this thesis.

First of all, I would like to express my sincere gratitude to my mentor at Delft University of Technology, Prof. Sjoerd Stallinga, who gave me the opportunity to pursue this unconventional doctoral research collaboration. Throughout the past years he gave me the freedom to explore my own research ideas but, at the same time, provided me with the necessary guidance and advice to merge them into scientific contributions. I want to thank him for continuously providing me with detailed and valuable feedback, despite the physical distance between Delft and Jena.

I would like to thank my former advisers at Fraunhofer IOF, Dr. Andreas Bräuer and Dr. Andreas Brückner as this Ph.D. collaboration would not have been possible without them. I am particularly grateful for their support on a professional and personal level during the first part of this Ph.D. period. I want to thank Dr. Ramona Eberhardt and Dr. Claudia Reinlein for their encouragement and advice that helped me finishing this work. In addition, I would like to express my gratitude to my co-workers at Fraunhofer IOF, who offered me an incredible work environment that motivated and encouraged me during my doctoral research. I would like to thank my colleagues from the micro-optical imaging as well as the active and adaptive optics group for the inspiring discussions, the professional support as well as all the fun we had together at work and at various free-time activities. In particular, the time spent in the office with my colleagues and friends, Christin and Martin, is most memorable and significantly shaped me on a personal and a professional level.

Finally, I would like to express the most important gratitude to my wife, Heidi Berlich. I will never take for granted that she crossed an ocean to share a life with me and to support me in pursuing this Ph.D. She always stood by my side with her unconditional love and support during the ups and downs of this chapter of my life.

CURRICULUM VITÆ

René BERLICH

17-05-1987 Born in Gera, Germany.

EDUCATION

- 1997–2005 Grammar School
Friedrich-Schiller-Gymnasium, Eisenberg, Germany
- 2006–2009 B.Sc. Physics
Friedrich-Schiller-Universität Jena, Germany
Thesis: “Photonenmanagement in Solarzellen: Analyse eines Ray Tracing Modells zur Absorptionsberechnung”
- 2009–2012 M.Sc. Optics/Photonics (dual)
University of Central Florida (CREOL), Orlando, USA (2009–2010)
Friedrich-Schiller-Universität Jena, Germany (2010–2012)
Thesis: “Ultra-compact microscope for fluorescence imaging”
- 2014–2021 Ph.D. Physics
Delft University of Technology, The Netherlands
Thesis: “Computational optical imaging based on helical point spread functions”

EMPLOYMENT

- 2012–2013 Young-Graduate-Trainee
European Space Research and Technology Centre (ESA)
Noordwijk, The Netherlands
- Since 2013 Research Associate
Fraunhofer Institute for Applied Optics and Precision Engineering
Jena, Germany

LIST OF PUBLICATIONS

Journal Publications

9. **R. Berlich** and S. Stallinga, *Image based aberration retrieval using helical point spread functions*, [Applied Optics](#) **59**, 6557 (2020).
8. C. Jin, M. Afsharnia, **R. Berlich**, S. Fasold, C. Zou, D. Arslan, I. Staude, T. Pertsch and F. Setzpfandt, *Dielectric metasurfaces for distance measurements and three-dimensional imaging*, [Adv. Photon.](#) **1**, 036001 (2019).
7. **R. Berlich** and S. Stallinga, *High-order-helix point spread functions for monocular three-dimensional imaging with superior aberration robustness*, [Opt. Express](#) **26**, 4873 (2018).
6. A. Brady, **R. Berlich**, N. Leonhard, T. Kopf, P. Böttner, R. Eberhardt and C. Reinlein, *Experimental validation of phase-only pre-compensation over 494 m free-space propagation*, [Optics Letters](#) **42**, 2679 (2017).
5. N. Leonhard, **R. Berlich**, S. Minardi, A. Barth, S. Mauch, J. Mocci, M. Goy, M. Appelfelder, E. Beckert and C. Reinlein, *Real-time adaptive optics testbed to investigate point-ahead angle in pre-compensation of Earth-to-GEO optical communication*, [Opt. Express](#) **24**, 13157 (2016).
4. **R. Berlich**, A. Bräuer and S. Stallinga, *Single shot three-dimensional imaging using an engineered point spread function*, [Opt. Express](#) **24**, 5946 (2016).
3. **R. Berlich**, D. Richter, M. Richardson and S. Nolte, *Fabrication of computer-generated holograms using femtosecond laser direct writing*, [Optics Letters](#) **41**, 1752 (2016).
2. **R. Berlich**, J. Choi, C. Mazuir, W.V. Schoenfeld, S. Nolte and M. Richardson, *Spatially resolved measurement of femtosecond laser induced refractive index changes in transparent materials*, [Optics Letters](#) **37**, 3003 (2012).
1. I. Mingareev, **R. Berlich**, T. Eichelkraut, H. Herfurth, S. Heinemann, and M. Richardson, *Diffractive optical elements utilized for efficiency enhancement of photovoltaic modules*, [Opt. Express](#) **19**, 11397 (2011).

Conference Contributions

9. S. Schacke, **R. Berlich**, B. Höfer, P. Dannberg, B. Zaage, C. Damm, E. Beckert and N. Danz, *Towards an ultrathin multi-aperture microscope*, [Proc. SPIE 11243, Imaging, Manipulation, and Analysis of Biomolecules, Cells, and Tissues XVIII](#) (2020).
8. M. Hubold, **R. Berlich**, R. Brüning and R. Brunner, *System calibration and characterization of an ultra-compact multispectral snapshot imaging system*, [Proc. SPIE 11144, Photonics and Education in Measurement Science](#) (2019).

7. M. Hubold, **R. Berlich**, C. Gassner, R. Brüning and R. Brunner, *Ultra-compact micro-optical system for multispectral imaging*, *Proc. SPIE 10545, MOEMS and Miniaturized Systems XVII*, 105450V (2018).
6. **R. Berlich**, T. Kopf, A. Brady, N. Leonhard, A. Kamm and C. Reinlein, *Transportable system for in-field testing of adaptive optical pre-compensation for optical feeder links*, *Proc. SPIE 10562, International Conference on Space Optics — ICSO* (2016).
5. N. Leonhard, **R. Berlich**, S. Minardi, A. Barth, C. Reinlein, *Adaptive optics testbed for pre- and post-compensation of earth-to-geo optical communication: downlink results*, *Proc. SPIE 10562, International Conference on Space Optics — ICSO* (2016).
4. **R. Berlich**, A. Bräuer, and S. Stallinga, *Single shot approach for three-dimensional imaging with double-helix point spread functions*, *Imaging and Applied Optics, OSA, paper CTh1D.4* (2016)
3. **R. Berlich**, A. Brückner, R. Leitel, A. Oberdörster, F. Wippermann and A. Bräuer, *Multi-aperture microoptical system for close-up imaging*, *Proc. SPIE 9192, Current Developments in Lens Design and Optical Engineering XV* (2014).
2. **R. Berlich** and B. Harnisch, *Radiometric assessment method for diffraction effects in hyper-spectral imagers applied to the Earth Explorer #8 mission candidate FLEX*, *Proc. SPIE 10563, International Conference on Space Optics — ICSO* (2014).
1. S. Kraft, J.-L. Bézy, U. Del Bello, **R. Berlich**, M. Drusch, R. Franco, A. Gabriele, B. Harnisch, R. Meynart and P. Silvestrin *FLORIS: phase A status of the fluorescence imaging spectrometer of the Earth Explorer mission candidate FLEX*, *Proc. SPIE 8889, Sensors, Systems, and Next-Generation Satellites XVII* (2013).